Interactions between Tropospheric Chemistry and Aerosols in a Unified GCM Simulation

Thesis by

Hong Liao

In Partial Fulfillment of the Requirements

for the Degree of

Doctor of Philosophy

California Institute of Technology

Pasadena, California

2002

(Submitted August 24, 2001)

Acknowledgements

I would like to express my sincere appreciation to Prof. John H. Seinfeld, my advisor, for his help, encouragement, and guidance throughout my graduate study at Caltech. I would also like to thank other members of my advisory committee, Prof. Richard C. Flagan, Prof. Michael R. Hoffmann, and Prof. Yuk L. Yung, for their comments and suggestions.

Many thanks go to several Seinfeld group members, Peter Adams, Serena Chuang, and Athanasios Nene, for their valuable ideas and discussions. I am especially thankful to Dr. Loretta Mickley and Prof. Daniel Jacob, our collaborators, at Harvard University. Dr. Loretta Mickley has given me tremendous help in tropospheric chemistry modeling. Prof. Daniel Jacob has given me many insightful suggestions.

Finally and most importantly, I thank my husband, Yonglin Hu, for his love and encouragement and our son, Allen, for the inspiration to bring this work to fruition. I would also like to thank my parents for their love, invaluable help, and support.

The research work reported in this dissertation was mostly supported by the National Aeronautics and Space Administration Earth Observing System Interdisciplinary Science program (NASA EOS-IDS) and, in part, by National Science Foundation grant ATM-9614105 and NASA grant NAG5-3553.

Abstract

Anthropogenic changes in the atmospheric abundances of tropospheric ozone and aerosols make significant contributions to climate change. In turn, climate change affects the abundances of ozone and aerosols, resulting in complicated feedbacks. To move toward understanding interactions and feedbacks among tropospheric chemistry, aerosol formation, and climate change, a unified tropospheric chemistry-aerosol model is developed within the Goddard Institute for Space Studies general circulation model. The model includes a detailed simulation of tropospheric ozone-NO_X-hydrocarbon chemistry and a thermodynamic representation of sulfate/nitrate/ammonium aerosols. Two-way coupling between aerosols and chemistry provides consistent chemical fields for aerosol dynamics and aerosol mass for heterogeneous processes and calculations of gas-phase photolysis rates. Although the current version of the unified model does not include prognostic treatments of black carbon, organic carbon, and mineral dust aerosols, we include effects of these particles on photolysis and heterogeneous processes by using three-dimensional off-line fields. The unified model is applied to examine interactions between tropospheric chemistry and aerosols. This dissertation is the first step in the development of a fully-coupled climate/chemistry/aerosol model.

Contents

List of Figures

List of Tables

Chapter 1

Introduction

Tropospheric ozone and aerosols are of considerable importance in radiative forcing of climate [*Intergovernmental Panel on Climate Change (IPCC)*, 1995]. Ozone is a significant greenhouse gas because of its absorption in the infrared, visible, and ultraviolet spectral regions. Aerosols can directly influence atmospheric radiation budget by scattering or absorbing radiation, and can indirectly affect the radiation budget through their modification of cloud albedo and lifetime. The global mean, annually averaged radiative forcing by tropospheric O_3 has been estimated to be 0.33 ± 0.05 W m^{-2} [*van Dorland et al.*, 1997; *Berntsen et al.*, 1997; *Roelofs et al.*, 1997; *Haywood et al.*, 1998; *Brasseur et al.*, 1998; *Kiehl et al.*, 1999]. Radiative forcing by aerosols depends on aerosol composition, mixing state, and size distribution, as well as aerosol water uptake. Direct radiative forcing by anthropogenic aerosols is estimated to be -0.3 to -1.5 W m^{-2}, while the indirect radiative forcing by anthropogenic aerosols is estimated to be 0 to -1.5 W m^{-2} [*Intergovernmental Panel on Climate Change (IPCC)*, 1995].

Tropospheric O_3 and aerosols have short atmospheric lifetimes (days to weeks) and hence inhomogeneous atmospheric distributions. The abundances of aerosols and ozone are controlled by a combination of direct and precursor emissions, chemical reactions in the atmosphere, meteorological processes, and interactions among tropospheric chemistry, aerosols, and climate change. While concentrations of gas-phase species govern many aspects of the formation and growth of aerosols, aerosols play important roles in atmospheric chemistry by altering photolysis rates [*Demerjian et al.*, 1980; *Ruggaber et al.*, 1994; *Jacobson*, 1998; *Liao et al.*, 1999] and by serving as sites for heterogeneous conversion of gas-phase species [*Dentener and Crutzen* 1993; *Dentener et al.*, 1996]. The

abundances of aerosols and ozone can also be significantly affected by climate change with resulting feedbacks. For example, changes in the atmospheric water cycle affect O_3 photochemistry [*Johnson et al.*, 1999] as well as the formation, optical properties, cloud activating properties, and wet scavenging of aerosols. Changes in tropospheric circulation affect the distributions and hence the radiative forcing of O_3 and aerosols [*Hansen et al.*, 1997]. Rising temperatures affect emissions of NO_X, hydrocarbons, and ammonia [*Yienger and Levy*, 1995; *Guenther et al.*, 1995; *Bouwman et al.*, 1997]. Increasing deep convection enhances the lightning source of NO_X [*Sinha and Tuomi*, 1996; *Tuomi et al.*, 1996]. Increasing sea surface winds promote emissions of dimethylsulfide (DMS) and sea salt aerosol from the oceans. Better understanding of aerosol-chemistry-climate interactions is critically needed for future climate change.

Despite intense study of the human influence on tropospheric ozone and aerosols, estimates of the global mean radiative forcing by ozone and aerosols still have large uncertainties. Few global aerosol and ozone simulations have considered the interactions among atmospheric dynamic, gas-phase chemistry, aerosol, and climate change. For example, concentrations of OH, NO_3, HO_2, or O_3 required in sulfate aerosol simulations have been imported from off-line atmospheric chemistry models [*Feichter et al.*, 1996; *Koch et al.*, 1999, *Adams et al.*, 1999; *Barth et al.*, 2000], and off-line aerosol concentrations have been used in global chemistry models to simulate heterogeneous processes [*Brasseur et al.*, 1998; *Wang et al.*, 1998; *Mickley et al.*, 1999]. Since off-line gas-phase (aerosol) fields are usually generated without considering interactions with aerosols (gas-phase chemistry), it may lead to bias in predicted concentrations. More

importantly, off-line fields cannot account for two-way interactions between tropospheric chemistry and aerosols, which are desired in simulations when climate changes feed back into gas-phase chemistry and aerosols.

To move toward incorporating interactions and feedbacks among tropospheric chemistry, aerosol formation, and climate change in a general circulation model, a unified model that simulates atmospheric chemistry and sulfate/nitrate/ammonium aerosols in the Goddard Institute for Space Studies (GISS) GCM is developed in this study.

In Chapter 2, effect of clouds on direct aerosol radiative forcing of climate is examined. Chapter 3 studies the sensitivity of mineral dust radiative forcing to its physical and optical properties, since dust is of considerable importance in global radiative forcing and the magnitude of dust forcing has large uncertainty. Chapter 4 investigates the effect of aerosols on atmospheric chemistry through altering photolysis rates. Chapter 5 presents a unified simulation of aerosols and tropospheric chemistry within a general circulation model. A thorough examination of interactions between gas-phase chemistry and aerosols is carried out by using this newly developed model. Chapter 6 presents summary and conclusions of this thesis research.

References

Adams, P. J., J. H. Seinfeld, and D. M. Koch, Global concentrations of tropospheric sulfate, nitrate, and ammonium aerosol simulated in a general circulation model, *J. Geophys. Res., 104*, 13,791–13,824, 1999.

Barth, M. C., P. J. Rasch, J. T. Kiehl, C. M. Benkovitz, and S. E. Schwartz, Sulfur chemistry in the National Center for Atmospheric Research Community Climate Model: Description, evaluation, features, and sensitivity to aqueous chemistry, *J. Geophys. Res., 105*, 1387–1415, 2000.

Berntsen, T. K., I. S. A. Isaksen, G. Myhre, J. S. Fuglestvedt, F. Stordal, T. A. Larsen, R. S. Freckleton, and K. P. Shine, Effects of anthropogenic emissions on tropospheric ozone and its radiative forcing, *J. Geophys. Res., 102*, 28101–28126, 1997.

Bouwman, A.F., D. S. Lee, W. A. H. Asman, F. J. Dentener, K. W. VanderHoek, and J. G. J. Olivier, A global high-resolution emission inventory for ammonia, *Global Biogeochem. Cycles, 11*, 561–587, 1997.

Brasseur, G. P., D. A. Hauglustaine, S. Walters, P. J. Rasch, J.-F. Mller, C. Granier, and X. X. Tie, MOZART, a global chemical transport model for ozone and related chemical tracers, 1. Model description, *J. Geophys. Res., 103*, 28,265–28,289, 1998.

Brasseur, G. P., J. T. Kiehl, J. F. Mller, T. Schneider, C. Granier, X. X. Tie, and D. Hauglustaine, Past and future changes in global tropospheric ozone: Impact on radiative forcing, *Geophys. Res. Lett., 25*, 3807–3810, 1998.

Demerjian, K. L., K. L. Schere, and J. T. Peterson, Theoretical estimates of actinic (spherially integrated) flux and photolytic rate constants of atmospheric species in the lower troposphere, *Adv. Environ. Sci. Tech., 10*, 369–459, 1980.

Dentener, F. J., and P. J. Crutzen, Reaction of N_2O_5 on tropospheric aerosols: impact on the global distributions of NO_X, O_3, and OH, *J. Geophys. Res., 98*, 7149–7163, 1993.

Dentener, F. J., G. R. Carmichael, Y. Zhang, J. Lelieveld, and P. J. Crutzen, Role of mineral aerosol as a reactive surface in the global troposphere, *J. Geophys. Res., 101*, 22,869–22,889, 1996.

Feichter, J, E. Kjellstrom, H. Rodhe, F. Dentener, J. Lelieveld, and G.-J. Roelofs, Simulation of the tropospheric sulfur cycle in a global climate model, *Atmos. Environ., 30*, 1693–1707, 1996.

Guenther, A., C. N. Hewitt, D. Erickson, R. Fall, C. Geron, T. Graedel, P. Harley, L. Klinger, M. Lerdau, W. A. Mckay, T. Pierce, B. Scholes, R. Steinbrecher, R. Tallamraju, J. Taylor, and P. Zimmerman, A global model of natural volatile organic compound emissions, *J. Geophys. Res., 100*, 8873–8892, 1995.

Hansen, J., M. Sato, and R. Ruedy, Radiative forcing and climate response, *J. Geophys. Res., 102*, 6831–6864, 1997.

Haywood, J. M., M. D. Schwarzkopf, and V. Ramaswamy, Estimates of radiative forcing due to modeled increases in tropospheric ozone, *J. Geophys. Res., 103*, 16,999–17,007, 1998.

Intergovernmental Panel on Climate Change (IPCC), *Climate Change 1994*, edited by J. T.

Houghton et al., Cambridge Univ. Press, New York, 1995.

Jacobson, M. Z., Studying the effects of aerosols on vertical photolysis rate coefficient and temperature profiles over an urban airshed, *J. Geophys. Res., 103*, 10,593–10,604, 1998.

Johnson, C. E., Relative roles of climate and emissions changes on future tropospheric oxidant concentrations, *J. Geophys. Res., 104*, 18,631–18,645, 1999.

Liao, H., and J. H. Seinfeld, Effects of aerosols on tropospheric photolysis rates in clear and cloudy atmospheres, *J. Geophys. Res., 104*, 23,697–23,707, 1999.

Kiehl, J. T., T. L. Schneider, R. W. Portmann, and S. Solomon, Climate forcing due to tropospheric and stratospheric ozone, *J. Geophys. Res., 104*, 31,239–31,254, 1999.

Koch, D. M., D. Jacob, I. Tegen, D. Rind, and M. Chin, Tropospheric sulfur simulation and sulfate direct radiative forcing in the GISS GCM, *J. Geophys. Res., 104*, 23,799–23,822, 1999.

Mickley, L. J., P. Murti, D. Jacob, J. Logan, and D. Rind, Radiative forcing from tropospheric ozone calculated with a unified chemistry-climate model, *J. Geophys. Res., 104*, 30,153–30,172, 1999.

Roelofs, G.-J., J. Lelieveld, and R. van Dorland, A three-dimensional chemistry/general circulation model simulation of anthropogenically derived ozone in the troposphere and its radiative forcing, *J. Geophys. Res., 102*, 23,389–23,401, 1997.

Ruggaber, A., R. Dlugir, and T. Nakajima, Modeling radiation quantities and photolysis

frequencies in the atmosphere, *J. Atmos. Chem., 18*, 171–210, 1994.

Sinha, A., and R. Toumi, Tropospheric ozone, lightning, and climate change, *J. Geophys. Res., 102*, 10,667–10,672, 1997.

Toumi, R., J. D. Haigh, and K. S. Law, A tropospheric ozone-lightning climate feedback, *Geophys. Res. Lett., 23*, 1037–1040, 1996.

van Dorland, R., F. J. Dentener, and J. Lelieveld, Radiative forcing due to tropospheric ozone and sulfate aerosols, *J. Geophys. Res., 102*, 28,079–28,100, 1997.

Wang, Y., D. J. Jacob, and J. A. Logan, Global simulation of tropospheric O_3-NO_X-hydrocarbon chemistry, 1. Model formulation, *J. Geophys. Res., 103*, 10,713–10,725, 1998.

Yienger J. J., and H. Levy, Empirical-model of global soil-biogenic NO_X emissions, *J. Geophys. Res., 100*, 11,447–11,464, 1995.

Chapter 2

Effect of Clouds on Direct Aerosol Radiative Forcing of Climate

[The text of this chapter appears in: Liao H. and Seinfeld J. H. (1998) *Journal of Geophysical Research-Atmospheres*, **103**, 3781-3788.]

ABSTRACT

The effect of a cloud layer on top-of-atmosphere (TOA) aerosol radiative forcing is examined by means of a one-dimensional vertical column simulation. To span the range between nonabsorbing and strongly absorbing particles, $(NH_4)_2SO_4$ and soot aerosols are considered individually and in internal and external mixtures. For a cloud layer embedded within an aerosol layer it is shown that direct aerosol radiative forcing still occurs. For a nonabsorbing aerosol a maximum in (negative) forcing actually occurs for a thin cloud layer (100 m thickness for the set of parameters considered). The presence of an embedded cloud layer enhances the heating effect of soot aerosol, producing, for thick clouds, forcing values as much as a factor of 3 over those under cloud-free conditions. An absorbing aerosol layer can lead to an increase of in-cloud solar heating rates by up to 3% for the parameter values considered here. A cirrus cloud layer above an aerosol layer leads to only modest changes of TOA aerosol forcing from those in the absence of the cloud layer; thus aerosol forcing in the presence of typical cirrus clouds cannot be neglected.

2.1 Introduction

Aerosols affect climate through the scattering and absorption of solar radiation (the so-called direct effect) and through their influence on cloud properties (the so-called indirect effect) [*Charlson et al.*, 1992; *National Research Council (NRC)*, 1996]. There exist a number of assessments of the range of direct aerosol radiative forcing effects [*Intergovernmental Panel on Climate Change (IPCC)*, 1995]. These include vertical column calculations [*Charlson et al.*, 1991; *Haywood et al.*, 1995; *Nemesure et al.*, 1995; *Pilinis et al.*, 1995] to three-dimensional global simulations [*Kiehl and Briegleb*, 1993; *Boucher and Anderson*, 1995; *Feichter et al.*, 1997; *Chuang et al.*, 1997]. Aerosol types considered include sulfates [*Charlson et al.*, 1991; *Kiehl and Briegleb*, 1993; *Nemesure et al.*, 1995; *Boucher and Anderson*, 1995; *Feichter et al.*, 1997; *Chuang et al.*, 1997], organic aerosol from biomass burning [*Penner et al.*, 1992], soot [*Penner*, 1995], and a synthetic global-average mixture of inorganic and organic species [*Pilinis et al.*, 1995]. Aside from global-scale simulations that naturally include the presence of clouds, most of the assessments of direct aerosol forcing consider a cloud-free atmosphere.

The goal of the current work is to explore systematically the radiative interactions that occur between cloud and aerosol layers. We consider incoming and outgoing solar and IR radiation in a one-dimensional vertical column of air extending to the top of the atmosphere. To explore the effect of aerosol optical properties, which are of essential importance, we assume that the aerosol can consist of pure ammonium sulfate, $(NH_4)_2SO_4$, pure elemental carbon (soot), or mixtures of the two species. Moreover, when a mixture is present, we specify this mixture to be either an internal mixture, in which every particle

contains both species, or an external mixture, in which the aerosol consists of pure $(NH_4)_2SO_4$ particles and pure soot particles. The size distributions of the sulfate and soot particles are prescribed.

We seek to understand the role of clouds in modifying clear-sky direct aerosol radiative forcing. Interactions of aerosols in cloud formation are extremely complex, and indeed this complexity is central to the indirect radiative effect of aerosols on climate. We do not address the effect of aerosols on cloud formation and processes in this work. By simply specifying a cloud layer to be present or not, we can explore how the presence of clouds modifies clear-sky direct aerosol radiative forcing. We separately consider the two cases of a stratus cloud and a cirrus cloud, the former lying within the aerosol layer and the latter positioned above it. For a water cloud the liquid water content and mean droplet size are specified, and the thickness (vertical extent) of the cloud is allowed to vary. One aspect of the specification of the aerosol/cloud system is the state of the aerosol inside the cloud itself when the cloud exists within the aerosol layer. With sulfate (hygroscopic) and soot (nonhygroscopic) particles, one would expect that the hygroscopic particles would be incorporated into the cloud droplets and the nonhygroscopic particles would remain as interstitial aerosol. Even so, for simplicity, we assume all particles are present as interstitial aerosol in the cloud in our calculations, and we will show later that such an assumption does not change the qualitative conclusions of this study.

The essential variables in the cloud/aerosol direct forcing problem are (1) whether a cloud is present or not; (2) whether the cloud lies within the aerosol layer (stratus) or not (cirrus); and (3) cloud thickness. Variables that will produce an effect that is either

secondary or predictable, and are not studied here, include the aerosol size distribution [see Pilinis et al., 1995], cloud liquid water content, and cloud droplet size distribution.

2.2 Radiative Transfer Model

The radiative transfer model of *Fu and Liou* [1993] is used in the present study. The model is based on the δ-four-stream approximation [*Liou et al.*, 1988] to solve the radiative transfer equation in six solar wavelength bands (0.2–0.7, 0.7–1.3, 1.3–1.9, 1.9–2.5, 2.5–3.5, and 3.5–4.0 μm) and 12 IR bands (2200–1900, 1900–1700, 1700–1400, 1400–1250, 1250–1100, 1100–980, 980–800, 800–670, 670–540, 540–400, 400–280, and 280–0 cm^{-1}). The model includes molecular Rayleigh scattering, gaseous absorption, and cloud effects; we have extended the model to include aerosol scattering and absorption. The model calculates total flux as the sum of direct solar and diffuse flux. The heating rate is calculated from the divergence of the net flux. To investigate the effect of aerosols and the interaction between aerosols and clouds, optical depth, single-scattering albedo, and asymmetry factor of the aerosols are calculated and combined with those of gases and cloud droplets in each wavelength range.

To enhance vertical resolution near the cloud layer, we have increased the number of vertical layers in the model from 70 to 98, giving a vertical resolution of about 100 m near the cloud layer. Pressure, temperature, ozone, and clear-sky water vapor mixing ratios are those from U.S. Standard Atmosphere (1976). For cloudy sky the standard atmospheric profile is used to obtain the saturation water vapor mixing ratio in cloud.

We take the solar constant to be 1376 W m^{-2} and the IR surface emissivity to be 1.0. The solar surface albedo is 0.2 in all calculations except in Section 2.9 where we study the effect of surface albedo. Mixing ratios of CO_2, CH_4, and N_2O are assumed to be uniform throughout the troposphere at 356, 1.7, and 0.31 ppm, respectively.

The code ELSIE [*Sloane*, 1984, 1986; *Sloane and Wolff*, 1985; *Sloane et al.*, 1991] is used to calculate aerosol optical properties. ELSIE considers particles to be internal mixtures and includes nitrate, sulfate, organic carbon, elemental carbon, and residual mass (dust). Particle index of refraction is calculated as a volume-weighted average of the indices of refraction of its components. For an external mixture of $(NH_4)_2SO_4$ and elemental carbon (soot), the single-scattering albedo ω and asymmetry factor g in each size range are calculated by [*d'Almeida et al.*, 1991]

$$\omega = \frac{\omega_s \sigma_s + \omega_c \sigma_c}{\sigma_s + \sigma_c} \tag{2.1}$$

$$g = \frac{g_s \omega_s \sigma_s + g_c \omega_c \sigma_c}{\omega_s \sigma_s + \omega_c \sigma_c} \tag{2.2}$$

where σ_s and σ_c are the total extinction cross sections of sulfate and carbon particles, respectively; ω_s and ω_c are the single-scattering albedos of sulfate and carbon particles, and g_s and g_c are the corresponding asymmetry factors.

2.3 Aerosol and Cloud Specification

A uniform aerosol layer from the Earth's surface to 5 km is assumed. The two possible aerosol constituents are $(NH_4)_2SO_4$ and soot. The dry mass size distributions of $(NH_4)_2SO_4$ and soot particles are assumed to be lognormal, with median diameter of 0.5 μm and geometric standard deviation of 2.0 for $(NH_4)_2SO_4$ and 0.1 μm and 2.0 for soot particles. Refractive indices for $(NH_4)_2SO_4$, soot, and water are from *Toon et al.* [1976], *World Climate Program (WCP)* [1986], and *Hale and Querry* [1973], respectively. Densities are taken to be 1.76 g cm^{-3} for $(NH_4)_2SO_4$ and 1.70 g cm^{-3} for soot. In a humid atmosphere, total aerosol volume is the sum of the dry volumes of the individual components plus the volume of water associated with the hygroscopic components. Liquid water volume associated with pure $(NH_4)_2SO_4$ particles and mixed $(NH_4)_2SO_4$ soot particles is calculated by using thermodynamic theory [*Pilinis and Seinfeld*, 1987; *Kim et al.*, 1993a,b]. It is assumed that soot is nonhygroscopic.

A uniform relative humidity of 50% is a reasonable approximation for the lowest 5 km of the U.S. Standard Atmosphere and is assumed to calculate the optical properties of the uniform aerosol layer. Since the relative humidity of deliquescence (RHD) of pure $(NH_4)_2SO_4$ is 80%, particles initially dry would remain dry at 50% RH. There is evidence, however, that atmospheric particles below their RHD frequently exist in the metastable state corresponding to the curve obtained by drying out an initially wet particle. In such a case, a detailed thermodynamic calculation predicts that the ratio of wet to dry particle diameters for pure $(NH_4)_2SO_4$ at 50% RH is 1.21 [*Pilinis and Seinfeld*, 1987; *Kim et al.*, 1993a,b].

A $(NH_4)_2SO_4$ concentration of 2.5 μg m^{-3} is representative of continental

conditions, as compared with an estimated global-mean sulfate concentration of 0.57 μg m^{-3} distributed over the lowest 12 km of the atmosphere [*Andreae*, 1995]. (If this global-mean level is instead distributed over a layer only 5 km thick, it increases to 1.3 μg m^{-3}.) When a pure soot aerosol only is considered, the mass concentration is assumed to be 0.5 μg m^{-3}. For comparison, *Chýlek et al.* [1996] estimated an upper limit global-mean concentration of black carbon of 0.5 μg m^{-3} uniformly distributed over a 1 km thick layer. The total mass concentration of internal and external mixtures is 3.0 μg m^{-3}, consisting of 2.5 μg m^{-3} $(NH_4)_2SO_4$ and 0.5 μg m^{-3} soot. The soot/sulfate mixture considered here is roughly representative of northern hemisphere continental conditions.

When a stratus cloud is present we assume a vertically uniform cloud layer centered at 900 m altitude with a thickness that is varied over the range of 100 to 1000 m. A liquid water content of 0.2 g m^{-3} and an effective cloud droplet radius of 10 μm are assumed. For cirrus cloud simulations we assume a cloud layer with a thickness of 2000 m extending from 7000 to 9000 m altitude. At a temperature of about -40°C at this altitude, a cloud ice content of 9.177×10^{-3} g m^{-3} and a mean effective particle size of 64.1 μm are assumed [*Fu and Liou*, 1993].

2.4 TOA Aerosol Forcing in Cloud-Free Conditions

Top-of-atmosphere (TOA) aerosol radiative forcing is defined as $-(F_a\uparrow - F_o\uparrow)$, where $F_o\uparrow$ and $F_a\uparrow$ are the upward solar fluxes for aerosol-free and aerosol-laden cases, respectively. The negative sign implies that if $F_a\uparrow > F_o\uparrow$, aerosols produce a cooling effect

Table 2.1 Aerosol Radiative Forcing Under Cloud Free Conditons

Aerosol Conditon	Total Dry Mass[a]	TOA Forcing, W m^{-2}
Pure $(NH_4)_2SO_4$	2.5(1.1)	-2.0
Pure soot	0.5(0.0)	+5.5
Internal mixture	3.0(1.1)	+4.6
External mixture	3.0(1.1)	+3.6

(TOA) incoming solar flux=1376 W m^{-2}. Solar zenith angle $\theta_o = 0°$. $F_o\uparrow$=253.8 W m^{-2}. Surface albedo = 0.2.
[a]Water mass at 50% RH is given in parentheses.

and vice versa. $F_o\uparrow$ is calculated for clear sky, including Rayleigh scattering and molecular absorption; then $F_a\uparrow$ is calculated with the addition of the aerosol layer.

Aerosol radiative forcing for $(NH_4)_2SO_4$, soot, and mixtures at solar zenith angle $\theta_o = 0°$ is given in Table 2.1. A 5 km thick layer of pure $(NH_4)_2SO_4$ aerosol at a dry mass concentration of 2.5 μg m^{-3} produces a forcing of -2.0 W m^{-2}. At the other extreme a comparable layer of pure soot aerosol at a concentration of 0.5 μg m^{-3} yields a forcing of +5.5 W m^{-2}, a heating effect. TOA aerosol forcing is sensitive to the aerosol mixing state. With every particle exhibiting some absorption, an internally mixed aerosol layer produces a larger warming effect than the corresponding external mixture; the TOA forcing of the internal mixture is +4.6 W m^{-2}, whereas that of the external mixture is +3.6 W m^{-2}.

2.5 TOA Forcing by Aerosols in the Presence of a Stratus Cloud

TOA radiative forcing of aerosols in the presence of a cloud layer is defined as $-(F_{a+c}\uparrow - F_c\uparrow)$, where $F_{a+c}\uparrow$ and $F_c\uparrow$ are upward solar fluxes at TOA for cloudy sky with

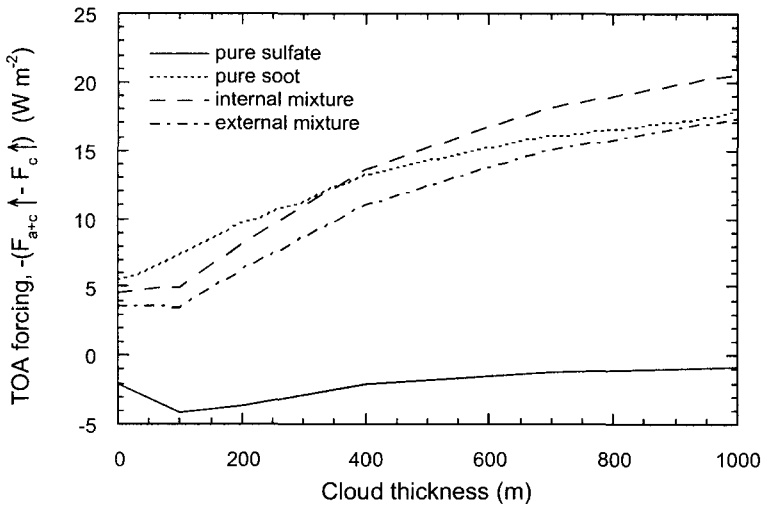

Figure 2.1 Top-of-atmosphere (TOA) radiative forcing, $-(F_{a+c}\uparrow - F_c\uparrow)$, as a function of cloud thickness for different aerosol compositions. Solar zenith angle=0°.

aerosols and cloudy sky without aerosols, respectively. The quantity $-(F_{a+c}\uparrow - F_c\uparrow)$ is shown as a function of cloud thickness in Figure 2.1 for $(NH_4)_2SO_4$, soot, and each of the mixtures. The TOA forcing effect of a pure $(NH_4)_2SO_4$ layer increases (greater negative effect, i.e., cooling) when a thin cloud is present but rapidly reaches a maximum at a cloud thickness of 100 m and then slowly decreases with increasing cloud thickness. For a pure soot aerosol, TOA forcing, in this case positive, i.e., heating, increases monotonically with increasing cloud thickness. The forcing effects of internally and externally mixed aerosols exhibit the same overall tendency of increasing forcing with increasing cloud thickness, except that when $(NH_4)_2SO_4$ is present the forcing tends in the direction of cooling when a thin cloud is present, reaches a minimum, and then increases. The forcing curve for pure soot begins above that of the internal mixture at zero cloud thickness, but the two curves cross at a cloud thickness of about 350 m; for clouds thicker than this, the internal mixture produces greater (positive) forcing than the pure soot aerosol.

Consider first the behavior of the pure $(NH_4)_2SO_4$ forcing as cloud thickness increases from zero. The maximum in negative forcing can be explained as follows: A cloud layer of 100 m thickness transmits about 85% of the downward solar flux and scatters the incident radiation from its original path. Since the upscatter fraction for diffuse radiation is larger than the upscatter fraction for incident radiation with the Sun at zenith [*Wiscombe and Grams*, 1976], the aerosols located below the cloud layer have larger negative forcing than they have in the absence of the thin cloud layer. For clouds thicker than this, the percentage of the solar beam transmitted through the cloud is smaller, so the contribution of the aerosols below the cloud to TOA forcing is decreased. Even when the particles contain a fraction of soot and are producing an overall heating effect, this balance between-cloud and below-cloud aerosol scattering still produces a cloud thickness at which heating is at a minimum, regardless of whether the particles are internally or externally mixed. It is apparent that the cloud thickness at which negative forcing is maximum or positive forcing is minimum depends on the solar zenith angle.

Since most of the soot aerosol resides above the cloud layer in our scenario, as cloud thickness increases, the soot aerosol above the cloud absorbs more radiation since the cloud is more effective at scattering increasing solar radiation back to space than either the aerosol layer alone or the Earth's surface.

We note from Figure 2.1 that for the case of pure $(NH_4)_2SO_4$ aerosol, (1) when the cloud layer is thick, $F_{a+c}\uparrow - F_c\uparrow < F_a\uparrow - F_o\uparrow$, and (2) the thicker the cloud layer, the smaller $F_{a+c}\uparrow - F_c\uparrow$. This result can be understood by using the adding method for multiple scattering [*Liou*, 1980]. When the cloud layer is thick, aerosol below the cloud layer can

be neglected. Let R_a and T_a denote the albedo and total (direct plus diffuse) transmission function for the aerosol layer above the cloud layer, and let R_c and T_c be the corresponding values for the cloud layer. The albedo of the cloud-aerosol combination is [*Liou*, 1980]

$$R_{a+c} = R_a + R_c \frac{T_a^2}{1 - R_a R_c} \tag{2.3}$$

Since pure $(NH_4)_2SO_4$ can be considered as nonabsorbing in the solar portion of the spectrum, $R_a + T_a = 1$. Thus (2.3) becomes

$$R_{a+c} = R_a + R_c \frac{(1 - R_a)^2}{1 - R_a R_c} \tag{2.4}$$

Since $0 < R_a < 1$ and $0 < R_c < 1$, $R_a + R_c < 2$. As a result

$$\frac{(1 - R_a)^2}{1 - R_a R_c} < 1 \tag{2.5}$$

and thus

$$R_{a+c} < R_a + R_c \tag{2.6}$$

Equation (2.6) indicates that the albedo of the combined aerosol-cloud system is less than the sum of the individual values of the aerosol and cloud layers. This is a result of the multiple scattering occurring between the cloud and the aerosol layers. Stated differently, $R_{a+c} - R_c < R_a$; that is, the increase in albedo that occurs when an aerosol layer is added to a cloud layer is less than that of the aerosol layer alone. Since $F_{a+c}\uparrow - F_c\uparrow = F_T T^2 (R_{a+c} - R_c)$ and $F_a\uparrow - F_o\uparrow = F_T T^2 R_a$, where F_T is the incident

solar flux at TOA and T is the transmission of the atmosphere above the aerosol layer, $F_{a+c}\uparrow\ -F_c\uparrow < F_a\uparrow\ -F_o\uparrow$. The quantity $F_{a+c}\uparrow\ -F_c\uparrow$ decreases as the cloud layer gets thicker. As cloud thickness increases, i.e., $R_c \rightarrow 1$, it is apparent from (2.3) that $(R_{a+c} - R_c) \rightarrow 0$. At a cloud albedo of unity, all incident radiation is sent back to space and the presence of the aerosol layer has no effect.

An intriguing property of the internally mixed aerosol case is the crossover of forcing for the pure soot and internal mixture at a cloud thickness of about 350 m. For both cases the mass concentration of soot is 0.5 μg m^{-3}. However, the internal mixture aerosol contains 2.5 μg m^{-3} additional $(NH_4)_2SO_4$. The median dry diameter of $(NH_4)_2SO_4$ is 0.5 μm, whereas that of the pure soot is 0.1 μm. The larger particle size and presence of nonabsorbing $(NH_4)_2SO_4$ make the scattering effect of the internally mixed aerosol much stronger than that of pure soot; the scattering coefficient for the internal mixture is about 38 times higher than that of pure soot. When the cloud layer is thin, the warming effect of pure soot exceeds that of the internal mixture. As the cloud thickness increases, the cooling effect from scattering is reduced, while the warming effect from absorption increases. In the external mixture the scattering coefficient is about the same as that of the internal mixture, but the absorption coefficient is slightly smaller than that of the internal mixture, so the overall aerosol does not have sufficient absorption, as cloud thickness increases, for the forcing curve to cross that of soot.

For simplicity we have assumed that particles are present as interstitial aerosol in the cloud. Whereas this assumption is likely to be a good one for soot aerosol, in-cloud $(NH_4)_2SO_4$ and the internally mixed aerosols, because of their solubility in water,

have probably been scavenged by cloud droplets. The question is what is the effect on forcing calculations if the $(NH_4)_2SO_4$ particles and internally mixed aerosol particles are retained in the cloud. For a 1000 m thick cloud the following results are obtained from our experiments: (1) for the case of pure $(NH_4)_2SO_4$, removing the $(NH_4)_2SO_4$ particles from the cloud layer leads to a decrease in the absolute value of forcing of 21%. At this point total net aerosol forcing is, however, very small; (2) for the external mixture, removing the $(NH_4)_2SO_4$ particles and leaving the soot particles inside the cloud cause an increase of only 0.6% in TOA forcing; (3) removing the internally mixed aerosol particles inside the cloud decreases the TOA forcing of the internal mixture by 16%. Thus the qualitative conclusions of the study do not change depending on whether soluble aerosol is retained in cloud or not.

Another assumption that we made in the calculations is that of a uniform aerosol layer, which has constant mass concentration from the surface to 5 km altitude. We can examine the effect of vertical variation of aerosol mass concentrations. For pure soot aerosol, which has the same column burden as in the uniform aerosol layer case, its mass concentration is now assumed to decrease linearly from its surface value to 1/10 of its surface value at 3 km altitude and then remain constant from 3 km to 5 km altitude. Compared with the uniform aerosol layer, this more realistic vertical profile produces almost identical TOA forcing under clear-sky conditions, but the TOA forcing is consistently smaller when a cloud layer is present because less aerosol is above the cloud layer. For example, in the presence of a 1000 m thick stratus cloud the TOA forcing of soot is 17.9 W m^{-2} when the aerosol layer is uniform, while it is 13.5 W m^{-2} with the assumed

vertical profile. In this case, about 72% of the total soot mass is above the cloud layer for the uniform aerosol layer, while only 40% of the total soot mass is above the cloud layer for the case with vertical mass variation. A similar study for pure $(NH_4)_2SO_4$ aerosol shows that the TOA forcing is not sensitive to vertical mass variation, either under clear-sky or under cloudy-sky conditions. Thus vertical variation of aerosol mass concentration affects the values of TOA forcing but does not change the essential physics of the problem.

2.6 TOA Aerosol Forcing in the Presence of a Cirrus Cloud

With a 2000 m thick cirrus cloud lying over the aerosol layer, at $\theta_o = 0°$, TOA forcing, $-(F_{a+c} \uparrow - F_c \uparrow)$, of pure $(NH_4)_2SO_4$ and soot layers are -3.3 and +4.9 W m^{-2}, respectively. These are to be compared with clear-sky TOA forcings of -2.0 and +5.5 W m^{-2} (Table 2.1). It is noteworthy that the cirrus cloud enhances the negative forcing of $(NH_4)_2SO_4$ but reduces the positive forcing of soot. Because the ice water content of the cirrus cloud (9.177×10^{-3} g m^{-3}) is much smaller than the liquid water content of the stratus cloud (0.2 g m^{-3}), the optical depth of a 2000 m cirrus cloud (0.93 in the wavelength band 0.2 to 0.7 μm) is much smaller than that of even a 100 m water cloud (3.10 in the same wavelength band); transmission of the cirrus cloud is about 90% while that of a 100 m stratus cloud is about 85%. The reason that the cirrus cloud slightly reduces the positive forcing of a soot aerosol layer lying below it is that absorption is proportional to radiation intensity, which is slightly reduced by the cirrus cloud. The explanation of why the cirrus cloud enhances negative sulfate forcing is that the cloud scatters the direction

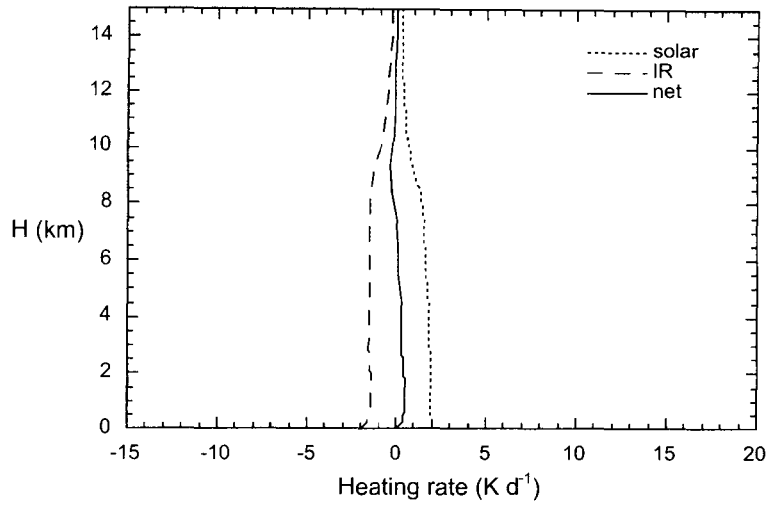

Figure 2.2 Atmospheric heating rates (solar, infrared, and net) for the aerosol-free and cloud-free atmosphere.

of the incident radiation from its $\theta_o = 0°$ path, causing a forcing increase similar to that which occurs with increasing solar zenith angle. It is clear that forcing by an aerosol layer underlying a cirrus layer cannot be neglected.

2.7 Heating Rates

The climate forcing effects of aerosols can be seen clearly in the vertical profiles of the heating rates. Under aerosol- and cloud-free conditions (Figure 2.2), heating caused by shortwave radiation is almost uniform in the troposphere. Solar heating is a result of gaseous absorption, and IR cooling is mainly a result of water vapor emission.

In the presence of a 1000 m thick stratus cloud and absence of aerosols (Figure 2.3), shortwave heating rates reach a maximum below the top of the cloud layer, corresponding to the point of maximum upward and downward solar fluxes (not shown). At the bottom

of the cloud layer, there is slight IR heating because the absorption of IR radiation emitted from the Earth's surface and the overlying cloud overweigh IR emission. At the top of the cloud layer, on the contrary, there is strong cooling because the IR emission there is much larger than the absorption of IR radiation emitted by the underlying cloud.

Figure 2.4 shows the difference in solar heating rates for four cases: (1) $(NH_4)_2SO_4$ layer versus clear sky (no cloud, no aerosol); (2) soot layer versus clear sky (no cloud, no aerosol); (3) $(NH_4)_2SO_4$ layer with cloud versus cloudy sky (no aerosol); and (4) soot layer with cloud versus cloudy sky (no aerosol). The cloud layer is 1000 m thick stratus cloud in cases (3) and (4). For a layer of pure $(NH_4)_2SO_4$ aerosol the difference in solar heating rate versus the cloud-free and aerosol-free atmosphere (Figure 2.2) is negligible, and the cooling effect of the aerosol layer is exclusively located at the surface. For a soot layer, on the other hand, a difference in solar heating rate of about 0.2 K d^{-1} is produced in the layer versus the cloud-free and aerosol-free atmosphere (Figure 2.2), about a 10% increase. When an $(NH_4)_2SO_4$ aerosol layer is added to a cloud layer, the change in solar heating is quite small, a slight cooling effect near cloud top that is negligible when compared to the approximately 30 K d^{-1} solar heating rate near the top of the cloud (Figure 2.3). The most interesting effect is that which occurs when a pure soot aerosol layer is present with a cloud layer. A differential solar heating rate of about 0.5 K d^{-1} occurs below the top of the cloud layer, corresponding to the maximum upward and downward solar fluxes. This 0.5 K d^{-1} is to be compared to the aerosol-free peak cloud heating rate of 20 to 30 K d^{-1} (Figure 2.3). Thus presence of the pure soot aerosol adds about 3% to the in-cloud solar heating rate, a small but nonnegligible effect.

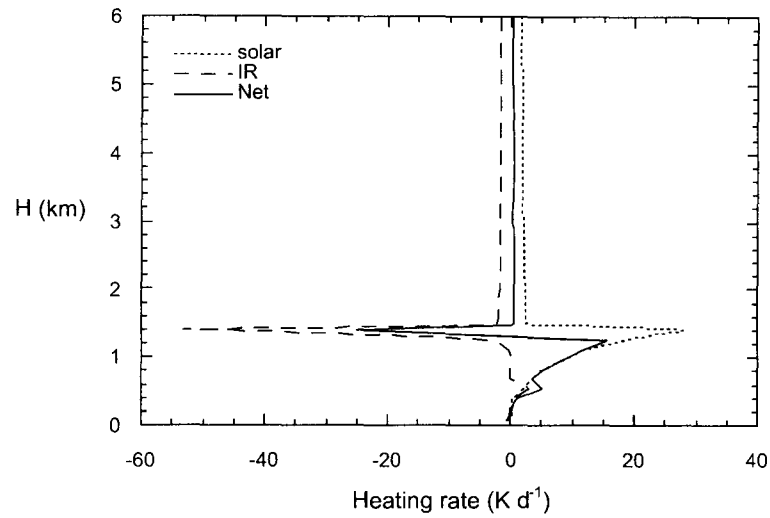

Figure 2.3 Atmospheric heating rates (solar, infrared, and net) for 1000 m thick cloud centered at 900 m altitude.

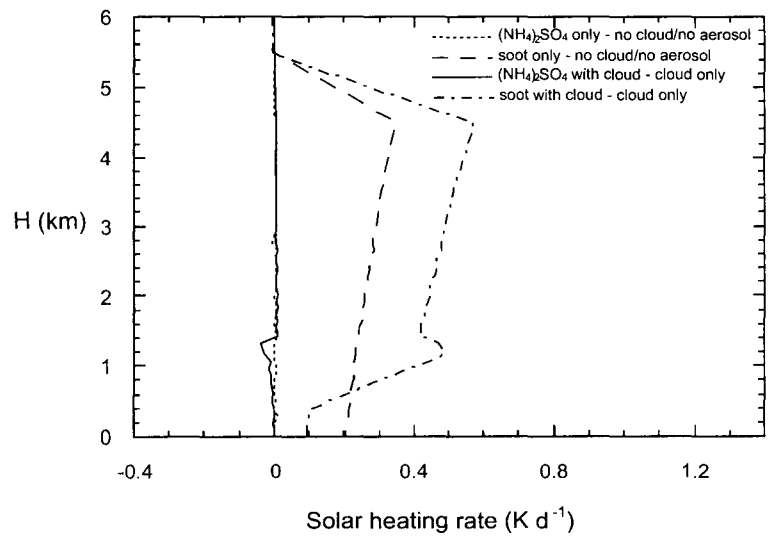

Figure 2.4 Differential solar heating rate for pure $(NH_4)_2SO_4$ and soot aerosol layers with and without cloud layer present. Cloud thickness 1000 m.

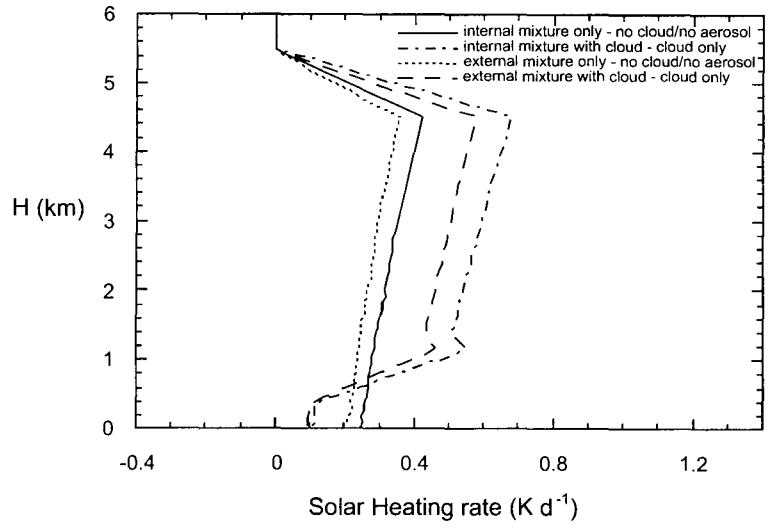

Figure 2.5 Differential solar heating rate for internal and external mixture. Cloud thickness 1000 m.

Figure 2.5 shows the differential solar heating rate again for the internal and external mixtures. As expected, the internal mixture produces a larger heating effect than the external mixture. Compared with clear-sky forcing, the presence of a 1000 m thick stratus cloud produces an increase of about 0.2 K d^{-1} in solar heating rate throughout the portion of the aerosol layer which is located above the cloud for both internal and external mixtures.

An increase in in-cloud solar heating rate of 3% as a result of the presence of an absorbing aerosol can be expected to lead to some alteration of cloud properties. This represents a cloud-aerosol feedback mechanism, as noted by *Hansen and Ruedy* [1997].

Since the optical depth of the cirrus cloud is very small, the differential heating rates caused by $(NH_4)_2SO_4$ or soot in the presence of an overlying cirrus cloud are

essentially identical to those caused by $(NH_4)_2SO_4$ or soot under clear-sky conditions, respectively.

2.8 Effect of Solar Zenith Angle

In examining the effect of solar zenith angle, we consider six cases: (1) pure $(NH_4)_2SO_4$ aerosol-no cloud; (2) pure $(NH_4)_2SO_4$-stratus cloud; (3) pure soot-no cloud; (4) pure soot-stratus cloud; (5) pure $(NH_4)_2SO_4$-cirrus cloud; and (6) pure soot-cirrus cloud. Cloud thickness is 1000 m for the stratus cloud and 2000 m for the cirrus cloud. TOA aerosol forcing is shown as a function of $\mu_0 = \cos\theta_o$ for the six cases in Figure 2.6. A maximum in negative forcing for the clear-sky $(NH_4)_2SO_4$ aerosol occurs at $\mu_o = 0.35$. The existence of such a maximum in forcing was demonstrated by *Nemesure et al.* [1995] and *Pilinis et al.* [1995]. The form of the $(NH_4)_2SO_4$ clear-sky curve as a function of solar zenith angle is consistent with that presented by *Russell et al.* [1997]. In the presence of the cirrus cloud the variation of TOA forcing of $(NH_4)_2SO_4$ versus μ_o has the same tendency as that of $(NH_4)_2SO_4$ under clear-sky conditions, even though the maximum shifts to $\mu_o = 0.6$ due to the effect of the cirrus cloud which scatters the incident radiation from its original path. When the stratus cloud is present, the magnitude of negative forcing is reduced, and negative forcing monotonically increases toward that at overhead Sun. As θ_o increases, the optical path through the cloud increases, producing the same effect as if the cloud layer is getting thicker. TOA forcing is positive for soot aerosols both with and without a cloud present with a maximum at $\theta_o = 0°$ ($\mu_o = 1.0$).

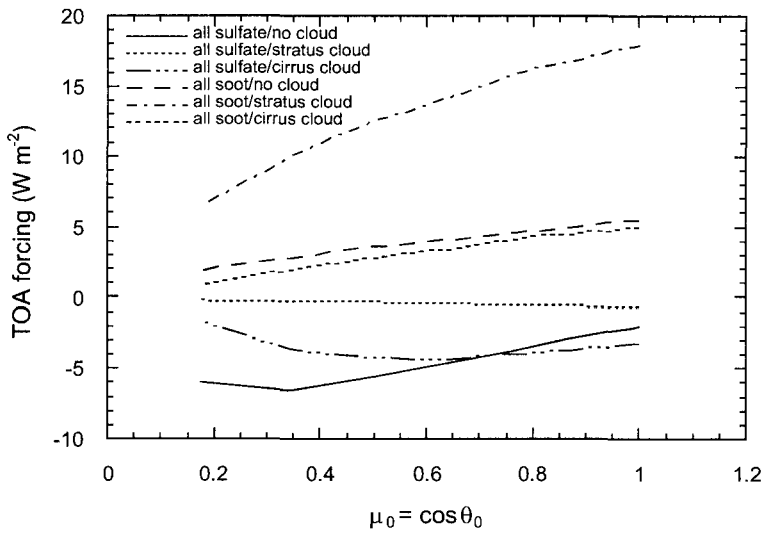

Figure 2.6 TOA radiative forcing as a function of $\mu_o = \cos\theta_o$ for pure $(NH_4)_2SO_4$ and soot aerosol layers with and without cloud layer present. Stratus cloud thickness 1000 m and cirrus cloud thickness 2000 m.

2.9 Effect of Surface Albedo

The same cases as in Section 2.8 are used to investigate the sensitivity of aerosol TOA forcing to surface albedo (Figure 2.7). Cloud thickness is 1000 m for the stratus cloud and 2000 m for the cirrus cloud, and solar zenith angle $\theta_o = 0°$. TOA forcing of $(NH_4)_2SO_4$ under clear-sky conditions or with the cirrus cloud has positive values when surface albedo is larger than about 0.4. This can be explained as follows: On one hand, absorption by the surface is increased when the aerosol layer is present and surface albedo is high. Some of the radiation that is reflected by the surface is backscattered to the surface by the aerosol layer and it is reflected again by the surface, thus the surface absorbs more radiation [*Haywood et al.*, 1997]. On the other hand, the increase in path length of the radiation due to scattering by the aerosol and surface leads to extra gaseous absorption.

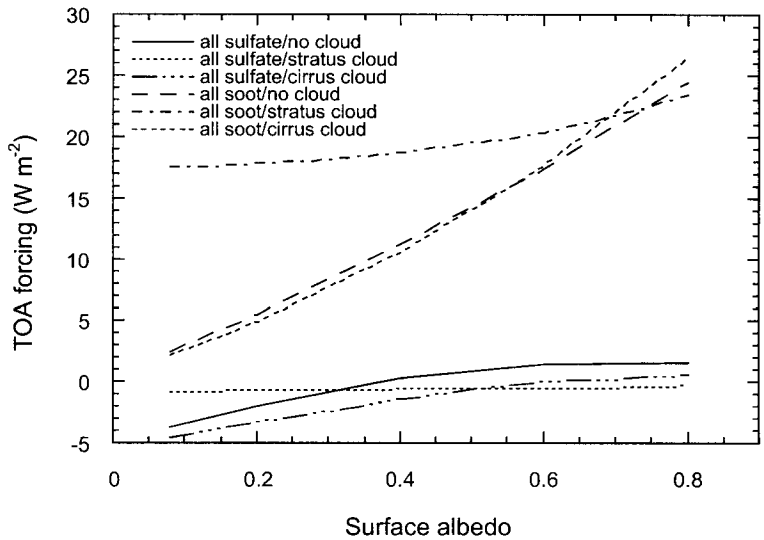

Figure 2.7 TOA radiative forcing as a function of surface albedo for pure $(NH_4)_2SO_4$ and soot aerosol layers with and without cloud layer present. Stratus cloud thickness 1000 m and cirrus cloud thickness 2000 m.

The TOA forcing of soot under clear-sky conditions or with the cirrus cloud increases dramatically with increasing surface albedo, ranging from about 2 W m^{-2} over sea surface (surface albedo$\approx$0.08) to about 25 W m^{-2} over snow surface (surface albedo$\approx$0.8), because the soot particles absorb both incoming radiation and radiation reflected by high-albedo surfaces. The TOA forcing of $(NH_4)_2SO_4$ or soot in the presence of a stratus cloud layer is not very sensitive to surface albedo because of the shielding effect of the cloud.

2.10 Conclusions

We have examined the change in TOA radiative forcing of an aerosol layer as a result of the presence of a stratus cloud layer for pure $(NH_4)_2SO_4$ and soot aerosols and internal and external mixtures of the two species. We consider a relatively low-level

($\sim$1 km altitude) cloud layer embedded within a uniform aerosol layer extending up to 5 km altitude. The "zeroth-order" approximation that direct radiative aerosol forcing occurs only in cloud-free regions is shown to be correct only for nonabsorbing aerosols and only as cloud albedo approaches unity. For strongly absorbing particles such as soot the presence of a cloud layer embedded within the aerosol layer actually enhances the heating effect of such particles. That enhancement continues to increase as cloud thickness increases, eventually reaching more or less an asymptotic value that can be as much as 3 times cloud-free forcing. The presence of a typical cirrus cloud layer above an aerosol layer leads to only modest changes of forcing from those in the absence of the cloud layer. Thus aerosol forcing in the presence of cirrus clouds cannot be neglected.

We show that an absorbing aerosol layer in the presence of an embedded cloud layer can lead to in-cloud solar heating rates that are, for the particular set of parameters considered here, up to 3% of the aerosol-free, in-cloud solar heating rates.

Acknowledgement. This work was supported by the National Science Foundation grant ATM-9614105.

References

Andreae, M., Climatic effects of changing atmospheric aerosol levels, in *World Survey of Climatology*, vol. 16, *Future Climates of the World*, edited by A. Henderson-Sellers, pp. 341-392, Elsevier, New York, 1995.

Boucher, O., and T. L. Anderson, General circulation model assessment of the sensitivity of direct climate forcing by anthropogenic sulfate aerosols to aerosol-size and chemistry, *J. Geophys. Res., 100*, 26, 117-26,134, 1995.

Charlson, R. J., J. Langner, H. Rodhe, C. B. Leovy, and S. G. Warren, Perturbation of the northern hemisphere radiative balance by backscattering from anthropogenic sulfate aerosols, *Tellus, 43AB*, 152-163, 1991.

Charlson, R. J., S. E. Schwartz, J. M. Hales, R. D. Cess, J. A. Coakley, J. E. Hansen, and D. J. Hofmann, Climate forcing by anthropogenic aerosol, *Science, 255*, 423-430, 1992.

Chuang, C.C., J.E. Penner, K.E. Taylor, A.S. Grossman, and J.J. Walton, An assessment of the radiative effects of anthropogenic sulfate, *J. Geophys. Res., 102*, 3761-3778, 1997.

Chýlek, P., G. B. Lesins, G. Vidden, J. G. D. Wong, R. G. Pinnick, D. Ngo, and J.D. Klett, Black carbon and absorption of solar radiation by clouds, *J. Geophys. Res., 101*, 23,365-23,371, 1996.

d'Almeida, G.A., P. Koepke, and E.P. Shettley, *Atmospheric Aerosols: Global Climatology*

and Radiative Characteristics, 261 pp., A. Deepak, Hampton, Va., 1991.

Feichter, J., U. Lohmann, and I. Schult, The atmospheric sulfur cycle in ECHAM-4 and its impact on the shortwave radiation, *Clim. Dyn., 13*, 235-246, 1997.

Fu, Q., and K. N. Liou, Parameterization of the radiative properties of cirrus clouds, *J. Atmos. Sci., 50*, 2008-2025, 1993.

Hale, G. M., and M. R. Querry, Optical constants of water in the 200 nm to 200 mm wavelength region, *Appl. Opt., 12*, 555-563, 1973.

Hansen J., M. Sato, and R. Ruedy, Radiative forcing and climate response, *J. Geophys. Res., 102*, 6831-6864, 1997.

Haywood, J. M., and K. P. Shine, The effect of anthropogenic sulfate and soot on the clear sky planetary radiation budget, *Geophys. Res. Lett., 22*, 603-606, 1995.

Haywood, J.M., D.L. Roberts, A. Slingo, J.M. Edwards, and K.P. Shine, General-circulation-model calculations of the direct radiative forcing by anthropogenic sulfate and fossil-fuel soot aerosol, *J. Clim., 10*, 1562-1577, 1997.

Intergovernmental Panel on Climate Change (IPCC), *Climate Change 1994: Radiative Forcing of Climate*, report to IPCC from the Scientific Assessment Working Group (WGI), Cambridge Univ. Press, New York, 1995.

Kiehl, J. T., and B. P. Briegleb, The relative roles of sulfate aerosols and greenhouse gases in climate forcing, *Science, 260*, 311-314, 1993.

Kim, Y. P., J. H. Seinfeld, and P. Saxena, Atmospheric gas aerosol equilibrium, I.

Thermodynamic model, *Aerosol Sci. Technol., 19*, 157-181, 1993a.

Kim, Y. P., J. H. Seinfeld, and P. Saxena, Atmospheric gas aerosol equilibrium, II. Analysis of common approximations and activity coefficient calculation methods, *Aerosol Sci. Technol., 19*, 182-198, 1993b.

Liou, K. N., *An Introduction to Atmospheric Radiation*, 217 pp., Academic Press, San Diego, Calif., 1980.

Liou, K. N., Q. Fu, and T. P. Ackerman, A simple formulation of the delta-four-stream approximation for radiative transfer parameterization, *J. Atmos. Sci., 45*, 1940-1947, 1988.

National Research Council (NRC), *A Plan for a Research Program on Aerosol Radiative Forcing and Climate*, Nat. Acad. Press, Washington, D. C., 1996.

Nemesure, S., R. Wagener, and S. E. Schwartz, Direct shortwave forcing of climate by anthropogenic sulfate aerosol: Sensitivity to particle size, composition, and relative humidity, *J. Geophys. Res., 100*, 26,105-26,116, 1995.

Penner, J. E., Carbonaceous aerosols in influencing atmospheric radiation: Black and organic carbon, in *Aerosol Forcing of Climate*, edited by R. J. Charlson and J. Heintzenberg, John Wiley, New York, 1995.

Penner, J. E., R. Dickinson, and C. O'Neill, Effects of aerosols from biomass burning on the global radiation budget, *Science, 256*, 1432-1434, 1992.

Pilinis, C., and J. H. Seinfeld, Continued development of a general equilibrium model for

inorganic multicomponent atmospheric aerosols, *Atmos. Environ., 21*, 2453-2466, 1987.

Pilinis, C., S. N. Pandis, and J. H. Seinfeld, Sensitivity of direct climate forcing by atmospheric aerosols to aerosol size and composition, *J. Geophys. Res., 100*, 18,739-18,754, 1995.

Russell, P. B., S. A. Kinne, and R. W. Bergstrom, Aerosol climate effects: Local radiative forcing and column closure experiments, *J. Geophys. Res., 102*, 9397-9407, 1997.

Sloane, C. S., Optical properties of aerosols of mixed composition, *Atmos. Environ., 18*, 871-878, 1984.

Sloane, C. S., Effect of composition on aerosol light scattering efficiencies, *Atmos. Environ., 20*, 1025-1037, 1986.

Sloane, C. S., and G. T. Wolff, Prediction of ambient light scattering using a physical model responsive to relative humidity: Validation with measurements from Detroit, *Atmos. Environ., 19*, 669-680,1985.

Sloane, C. S., J. G. Watson, J. C. Chow, L. C. Pritchett, and L. W. Richards, Size-segregated fine particle measurements by chemical species and their impact on visibility impairment in Denver, *Atmos. Environ., 25A*, 1013-1024, 1991.

Toon, O. B., J. B. Pollack, and B. N. Khare, The optical constants of several atmospheric aerosol species: Ammonium sulfate, aluminum oxide, and sodium chloride, *J. Geophys. Res., 81*, 5733-5748, 1976.

van de Hulst, H. C., *Light Scattering by Small Particles*, Wiley, New York, 470 pp., 1957.

Wiscombe, W., and G. Grams, The backscattered fraction in two-stream approximations, *J. Atmos. Sci., 33*, 2440-2451, 1976.

World Climate Program (WCP), A preliminary cloudless standard atmosphere for radiation computation, *WCP-112*, World Meteorol. Organ., Geneva, 1986.

Chapter 3

Radiative Forcing by Mineral Dust Aerosols: Sensitivity to Key Variables

[The text of this chapter appears in Liao H. and Seinfeld J.H. (1998) *Journal of Geophysical Research*, **103**, 31637-31645]

ABSTRACT

We examine diurnally averaged radiative forcing by mineral dust aerosols in shortwave and longwave spectral regions using a one-dimensional column radiation model. At the top of the atmosphere (TOA), net (shortwave plus longwave) dust radiative forcing can be positive (heating) or negative (cooling) depending on values of key variables. We derive an analytical expression for the critical single-scattering albedo at which forcing changes sign for an atmosphere containing both cloud and aerosol layers. At the surface, net dust forcing can be positive or negative under clear-sky conditions, whereas it is always cooling in the presence of a low-level stratus cloud. Longwave radiative forcing is essentially zero when clouds are present. We also study the sensitivity of dust diurnally averaged forcing to the imaginary part of refractive index (k), height of the dust layer, dust particle size, and dust optical depth. These variables play different roles as follows: (1) under both clear- and cloudy sky conditions, net TOA forcing is more sensitive to k than net surface forcing; (2) clear-sky longwave forcing and cloudy-sky TOA shortwave forcing are very sensitive to the altitude of the dust layer; although clear-sky shortwave forcing is not sensitive to it; (3) clear-sky shortwave forcing is much more sensitive to particle size than cloudy-sky shortwave forcing; longwave forcing is not sensitive to particle size; and (4) all forcings are sensitive to optical depth except cloudy-sky longwave forcing.

3.1 Introduction

Among the aerosol constituents of the Earth's atmosphere, those with the most poorly characterized and most variable optical properties are the mineral dusts from deserts and arid regions. The magnitude of global mean radiative forcing by mineral dust has been estimated to be comparable to that of anthropogenic aerosols [*Sokolik and Toon*, 1996]. Early studies of dust radiative effects were performed in the 1980s [*Carlson and Benjamin*, 1980] and in the context of nuclear winter scenarios [*Ramaswamy and Kiehl*, 1985; *Cess*, 1985]. *Tegen and Lacis* [1996] showed that the sign of total (shortwave plus longwave) radiative forcing at the tropopause can be either positive (warming) or negative (cooling) depending on the particle size and vertical distribution of the dust layer. Furthermore, using a general circulation model (GCM), *Tegen et al.* [1996] calculated the top of atmosphere (TOA) radiative forcing of mineral dust aerosol and found that forcing at solar wavelengths can be either positive or negative, depending on clear versus cloudy sky conditions and on the local surface albedo. *Sokolik et al.* [1998] have studied the importance of mineral dust radiative forcing at infrared wavelengths.

Because of its importance in global radiative forcing by aerosols and because of the considerable uncertainty attending the magnitude of that forcing, we systematically examine here, using a one-dimensional radiative transfer model, the sensitivity of dust radiative forcing to its physical and optical properties, the vertical distribution of dust in the atmosphere, surface albedo, and to the presence or absence of clouds. Our goal is both to define regions of forcing behavior (positive or negative forcing) and to establish the quantitative sensitivity of forcing to uncertainties in essential variables.

3.2 Radiative Transfer Model

The radiative transfer model of *Fu and Liou* [1993] calculates shortwave fluxes over six solar bands (0.2–0.7, 0.7–1.3, 1.3–1.9, 1.9–2.5, 2.5–3.5, and 3.5–4.0 μm) and longwave fluxes over 12 infrared spectral intervals (2200–1900, 1900–1700, 1700–1400, 1400–1250, 1250–1100, 1100–980, 980–800, 800–670, 670–540, 540–400, 400–280, and 280–0 cm^{-1}). The model includes molecular Rayleigh scattering, gaseous absorption, and cloud effects; we have extended the model to include aerosol absorption and scattering. The atmosphere is divided into 98 layers, with a vertical resolution of 100 m near the cloud layer and of 1 km at other altitudes. Vertical profiles of pressure, temperature, ozone, and H_2O vapor mixing ratios are from U.S. Standard Atmosphere (1976). The solar constant is 1376 Wm^{-2}.

Mie theory is used to calculate the optical properties of dust aerosols. For each solar band i of the radiative code, single-scattering albedo is calculated by integrating over the band as $\omega_i = \int W(\lambda)\omega d\lambda / \int W(\lambda) d\lambda$, where $W(\lambda)$ is the incident solar flux at the top of the atmosphere; for each longwave band, $\omega_i = \int \omega d\lambda / \int d\lambda$. The extinction cross section and asymmetry factor are also calculated in the same manner.

Both diurnally averaged TOA and surface radiative forcing are examined in this work. Letting $\Delta F(\mu_0)$ denote the radiative forcing, where μ_0 is the cosine of the solar zenith angle, the diurnally averaged forcing $\Delta\overline{F}$ is calculated by [*Cess*, 1985]

$$\Delta\overline{F} = \frac{1}{2}\int_0^1 \Delta F(\mu_0) d\mu_0 \tag{3.1}$$

For surface forcing, ΔF is defined as $(F_s^d - F_s^0)$ for clear-sky conditions and $(F_s^{c+d} - F_s^c)$ for cloudy-sky conditions, where F_s^0 and F_s^d are the net fluxes (downward is positive) at the surface for dust-free and dust-laden cases, respectively; F_s^c and F_s^{c+d} are net fluxes at the surface for cloudy sky without dust and cloudy sky with dust, respectively. For TOA forcing, ΔF is defined as $-(F_{TOA}^d\uparrow - F_{TOA}^0\uparrow)$ for clear-sky conditions and $-(F_{TOA}^{c+d}\uparrow - F_{TOA}^c\uparrow)$ for cloudy sky conditions, where $F_{TOA}^0\uparrow$ and $F_{TOA}^d\uparrow$ are the upward fluxes at TOA for dust-free and dust-laden cases, respectively; $F_{TOA}^c\uparrow$ and $F_{TOA}^{c+d}\uparrow$ are upward fluxes at TOA for cloudy sky without dust and cloudy sky with dust, respectively. The negative sign implies that if $F_{TOA}^d\uparrow > F_{TOA}^0\uparrow$, aerosols produce a cooling effect at TOA and vice versa.

3.3 Basis of the Analysis

We apply the one-dimensional radiative transfer model to examine the sensitivity of mineral dust radiative forcing to variation in key parameters. A uniform dust layer with column burden of 100 mg m^{-2} is assumed. On the basis of the analysis of *Dentener et al.* [1996], 100 mg m^{-2} is roughly the annual average column dust burden over North Africa and Asia. The optical depth of the dust layer depends on particle size; for a column burden of 100 mg m^{-2}, the optical depth is 0.02 (in the wavelength band 0.2 to 0.7 μm) for a dust mass median diameter of 8 μm and 0.21 (in the same wavelength band) for a mass median diameter of 1 μm. Three different altitudes for the dust layer will be considered: 0–3 km, 0–1 km, and 3–6 km. The cloud layer, when present, is highly simplified; we assume the layer is vertically uniform and is located between 1 and 1.5 km, with a liquid water

content of 0.2 g m^{-3} and an effective cloud drop radius of 10 μm. The optical depth of the cloud layer is 15.5 in the wavelength band of 0.2 to 0.7 μm. Since we are concerned here principally with the radiative interaction between cloud and dust layers, it is sufficient to consider such a simplified cloud layer. Dust particles are assumed to be spherical, having a mass distribution that is lognormal with geometric standard deviation of 2.0. The dust mass median diameter will be varied over the range of 1.0 to 8.0 μm. Dust density is taken to be 2.5 g cm^{-3}. (*Tegen and Fung* [1994] assumed 2.5–2.65 g cm^{-3} for different dust particle size classes.) It should be noted that the assumption of particle sphericity may not lead to significant errors for a climate forcing calculation since integration over the entire hemisphere is performed [*Mishchenko*, 1993; *Mishchenko and Travis*, 1994; *Lacis and Mishchenko*, 1995]. For satellite data retrieval, on the other hand, properly accounting for the nonspherical nature of particles is necessary.

There is significant variation in the refractive index of dust aerosol from the world's desert regions, especially the imaginary component k [*Patterson et al.*, 1977; *Sokolik et al.*, 1993, 1998]. We select for the base case refractive indices that lie at about the average values of a variety of measurements; we use curve 8 in Figure 1 of *Sokolik et al.* [1993] for k in the shortwave wavelength region and curve 5 in Figure 1a of *Sokolik et al.* [1998] for k in the longwave region. Thus k is 0.006 and 0.25 at the wavelengths of 0.5 μm and 10 μm, respectively. Although values of the real part of the refractive index also vary, the value of 1.5 chosen here is relatively representative of many dusts and is not varied in our study.

The sensitivity of diurnally averaged forcing to key variables is studied in two

ways. First, overall sensitivity is evaluated by examining the dependence of diurnally averaged forcing on key variables. Second, the local sensitivity, the derivative of forcing with respect to parameters that may vary, is calculated as follows. The local sensitivity of diurnally averaged radiative forcing (at TOA or surface) to a parameter x is $x\frac{\partial \Delta \overline{F}}{\partial x}$ (approximated by $x\frac{\Delta \overline{F}|_{x+\Delta x} - \Delta \overline{F}|_{x-\Delta x}}{2\Delta x}$) [*Chýlek and Kiehl*, 1981], where x represents, in the current case, variables such as refractive index, mass median diameter, and dust optical depth; the overall quantity is the change in radiative forcing (in W m^{-2}) per fractional change in x.

3.4 Dependence of Diurnally Averaged Radiative Forcing on Key Variables

3.4.1 Dependence of Radiative Forcing on Surface Albedo

Figure 3.1 shows diurnally averaged TOA and surface shortwave forcing in the absence and presence of a cloud layer as a function of surface albedo r_s. The dust layer is located at 0–3 km and dust mass median diameter is 3.5 μm. Clear-sky TOA shortwave forcing increases from negative (cooling) to positive (heating) as surface albedo increases, whereas TOA forcing in the presence of the cloud layer is positive for all surface reflectances. High-albedo surfaces and/or the presence of a cloud layer lead to enhanced absorption of reflected radiation thus producing heating at TOA. Surface shortwave forcing of mineral dust aerosol is negative under both clear and cloudy sky conditions. The magnitude of cooling under clear-sky conditions decreases as surface albedo increases.

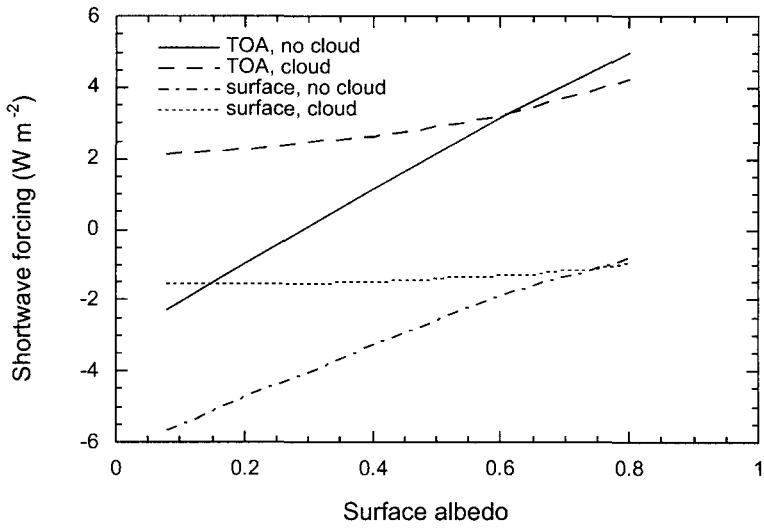

Figure 3.1 TOA and surface diurnally averaged shortwave dust forcing as a functin of surface albedo r_s under cloud-free and cloud conditions. Dust layer of total column burden 100 mg m^{-2} located over 0–3 km altitude. Mass distribution of dust log-normally distributed with mass median diameter of 3.5 μm and geometric standard deviation of 2.0.

This behavior can be understood by examining the definition for surface shortwave forcing, $(F_s^d - F_s^0)$, which can be expressed as $(1 - r_s)(F_s^d\downarrow - F_s^0\downarrow)$, where F_s^0 and F_s^d are the downward shortwave fluxes at the surface for dust-free and dust-laden cases, respectively. When surface albedo increases, the magnitude of $(F_s^d\downarrow - F_s^0\downarrow)$ decreases (smaller negative value) as a result of multiple scattering between aerosol and surface, and the factor $(1 - r_s)$ also decreases; thus under clear-sky conditions, the surface experiences less cooling at higher surface albedo. Cloudy sky surface shortwave forcing is defined as $(F_s^{c+d} - F_s^c)$, which can be written as $(1 - r_s)(F_s^{c+d}\downarrow - F_s^c\downarrow)$, where $F_s^c\downarrow$ and $F_s^{c+d}\downarrow$ are downward solar fluxes at the surface for cloudy sky without dust and cloudy sky with dust, respectively. As surface albedo increases, even though $(1 - r_s)$ decreases rapidly, $(F_s^{c+d}\downarrow - F_s^c\downarrow)$ increases in magnitude at about the same rate (greater negative value), leading to the net effect that

surface shortwave cooling under cloudy sky conditions is relatively independent of surface albedo for $0.08 < r_s < 0.8$. It is important to note that over ocean and normal land surfaces ($r_s < 0.4$), the magnitude of surface forcing under cloudy sky conditions is considerably smaller than that under clear sky conditions; at a surface albedo of 0.20, for example, surface forcing of dust is about -4.7 W m^{-2} in the absence of the cloud layer and -1.5 W m^{-2} in its presence.

Longwave radiative forcing is independent of surface albedo and is positive (heating) at both TOA and surface. For the conditions assumed here, TOA longwave forcing is 0.40 W m^{-2}, and surface longwave is 1.30 W m^{-2} for clear-sky conditions, and both TOA and surface longwave forcing are 0.10 W m^{-2} when the cloud layer is present. The fact that the cloud layer greatly reduces both TOA and surface longwave forcing will be addressed subsequently.

3.4.2 Dependence of Radiative Forcing on Altitude of the Dust Layer

Although mineral dust generally resides in the lowest several kilometers of the atmosphere, dust particles can be transported to high altitudes. To examine the effect of dust layer altitude on radiative forcing, we consider the vertically uniform dust layer of fixed column burden 100 mg m^{-2} occupying each of three altitude ranges: 0–3 km, 0–1 km, and 3–6 km. Dust mass median diameter is assumed to be 3.5 μm.

In the absence of clouds, shortwave forcing is not sensitive to the altitude of the dust layer; both TOA and surface shortwave forcing are about the same as those with the dust layer at 0–3 km (see Figure 3.1). In the presence of a cloud layer, TOA warming is

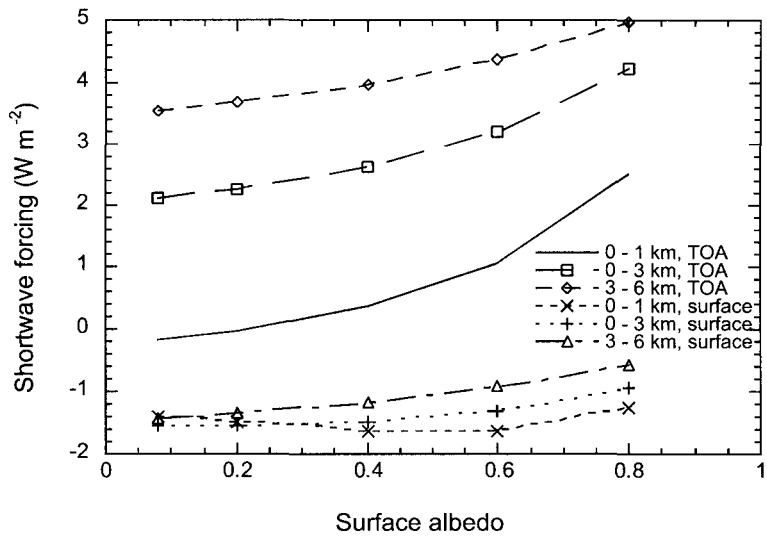

Figure 3.2 Cloudy-sky TOA and surface diurnally averaged shortwave dust forcing as a function of surface albede r_s for different assumed dust layer altitudes. Cloud layer of liquid water content 0.2 g m^{-3} and effective droplet radius 10 μm located between 1 and 1.5 km altitude. Dust layer of total column burden 100 mg m^{-2}. Mass distribution of dust lognormally distributed with mass median diameter of 3.5 μm and geometric standard deviation of 2.0.

strongest when the dust layer lies above the cloud layer (Figure 3.2), since the dust absorbs both incoming solar radiation and that reflected by the cloud layer [*Crisp*, 1997; *Haywood and Shine*, 1997; *Hansen et al.*, 1997].

With 50% of total column burden located above cloud, TOA forcing of a dust layer at 0–3 km is about 2 W m^{-2} larger than that of a dust layer at 0–1 km and about 1.5 W m^{-2} lower than that of a dust layer at 3–6 km. The three lines for TOA forcing tend to converge when surface albedo is high ($r_s > 0.6$) because the high-albedo surface leads to more absorption of radiation by aerosols below the cloud layer. When the dust layer lies completely beneath cloud, TOA shortwave forcing changes sign as r_s increases, being negative over low-albedo surfaces and positive over high-albedo surfaces.

Table 3.1 Diurnal-Average Longwave Radiative Forcing Under Cloud-Free and Cloud Conditions

Dust Layer Altitude, km	Without Cloud, W m^{-2}		With Cloud, W m^{-2}	
	TOA	Surface	TOA	Surface
0–1	0.2	1.4	0.0	0.1
0–3	0.4	1.3	0.1	0.1
3–6	1.0	0.9	0.6	0.0

Surface shortwave forcing under cloudy sky conditions is not so sensitive to the altitude of the dust layer as TOA shortwave forcing, especially over low-albedo surfaces ($r_s < 0.3$). Surfaces with higher albedo ($r_s > 0.3$) lead to stronger multiple scattering among surface, cloud and dust aerosol, as well as more absorption along the optical path. When the dust layer is located below the cloud layer (0-1 km), multiple scattering produces the strongest cooling for high-albedo surfaces.

Longwave radiative forcing for the three dust layer altitudes is given in Table 3.1. Under clear sky conditions, the higher the dust layer, the larger the TOA forcing but the smaller the surface forcing. The temperature of the dust layer is lower the higher its altitude; thus emission of longwave radiation is smaller, so less longwave radiation both escapes to space and arrives at the surface. In the presence of a cloud layer, both TOA and surface longwave forcing are practically negligible in all cases, except for the case when the dust layer is completely above cloud (at 3–6 km altitude). When cloud overlays the dust layer, it absorbs the IR radiation emitted by the dust layer and emits longwave radiation at its top. Since the temperature at the top of the cloud layer is assumed to be the same both with and without dust, TOA IR forcing is zero on the basis of our definition of forcing. When the dust layer is above cloud at 3–6 km, IR forcing still exists, but the magnitude

is smaller compared with that under clear-sky conditions, because the temperature at the top of the cloud is lower than that at the surface. Surface longwave forcing in the presence of the cloud layer is essentially zero because the effect of dust aerosol above the cloud is blocked by the cloud, while the aerosols below cloud cannot exert forcing on the surface as the particles have about the same temperature as the cloud bottom.

3.4.3 Dependence of Radiative Forcing on Dust Mass Median Diameter

To examine the effect of aerosol size on dust radiative forcing, we vary the mass median diameter of the dust layer from 1.0 μm to 8.0 μm to span the range from long-lived, transported dust to that at source regions. The column burden and altitude of the dust layer are fixed at 100 mg m^{-2} and 0–3 km, respectively.

Diurnally averaged shortwave forcing as a function of dust mass median diameter and surface albedo is shown for clear and cloudy conditions in Figures 3.3 and 3.4, respectively. Under clear-sky conditions, as mass median diameter increases, shortwave forcing tends toward warming, which is in agreement with the results obtained by *Tegen and Lacis* [1996]. Negative forcing decreases in magnitude or positive forcing increases in magnitude as mass median diameter increases from 1 μm to 5 μm, whereas both TOA and surface forcing change more slowly when mass median diameter exceeds 5 μm. The fact that shortwave forcing is very sensitive to mass median diameter in the 1.0 to 5.0 μm region indicates that this will be a key variable in global mineral dust forcing simulations, since about 90% of global dust mass loading is assumed to lie in this size region [*Tegen*

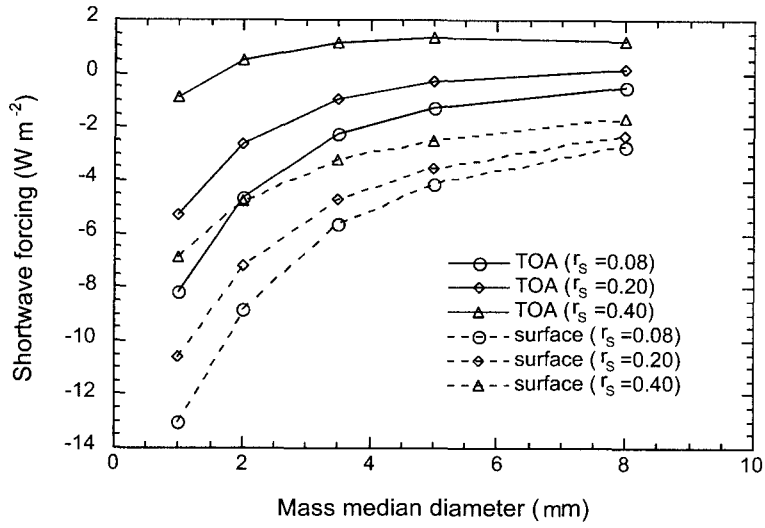

Figure 3.3 TOA and surface diurnally averaged shortwave dust forcing as a functin of dust mass median diameter and surface albedo r_s under cloud-free conditions. Dust layer of total column burden 100 mg m^{-2} located over 0–3 km altitude. Mass distribution of dust lognormally distributed with geometric standard deviation of 2.0.

and Lacis, 1996].

In contrast to the clear-sky case, in the presence of a cloud layer, TOA forcing is always positive (heating), with the maximum forcing occurring at a dust mass median diameter of about 2.0 μm for $r_s \leq 0.4$. The reason that the maximum positive TOA forcing occurs at a mass median diameter of about 2.0 μm can be explained as follows. At solar wavelengths, the single-scattering albedo ω decreases with increasing particle size [*Tegen and Lacis*, 1996]. When the dust mass median diameter exceeds about 2 μm at a fixed mass loading, however, the effect of absorption begins to decrease strongly because the total particle number concentration falls off rapidly. For the conditions assumed here, for example, dust number concentration is 28 cm^{-3} at a mass median diameter of 2 μm, whereas it is 5 cm^{-3} at a mass median diameter of 3.5 μm.

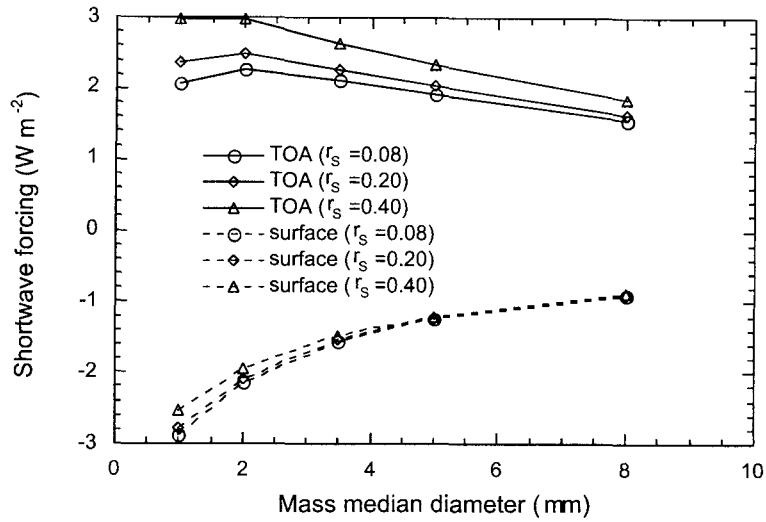

Figure 3.4 TOA and surface diurnally averaged shortwave dust forcing as a functin of dust mass median diameter and surface albedo r_s in the presence of a cloud layer. Cloud layer of liquid water content 0.2 g m^{-3} and effective droplet radius 10 μm located between 1 and 1.5 km altitude. Dust layer of total column burden 100 mg m^{-2} located over 0–3 km altitude. Mass distribution of dust lognormally distributed with geometric standard deviation of 2.0.

Table 3.2 Diurnal-Average Longwave Radiative Forcing Under Cloud-Free and Cloud Conditons

Mass Median Diameter, μm	Without Cloud, W m^{-2}		With Cloud, W m^{-2}	
	TOA	Surface	TOA	Surface
1.0	0.2	1.0	0.0	0.1
2.0	0.4	1.3	0.0	0.1
3.5	0.4	1.3	0.1	0.1
5.0	0.5	1.3	0.1	0.1
8.0	0.4	1.1	0.1	0.1

Longwave forcing for different mass median diameters is given in Table 3.2. For clear-sky conditions, both TOA and surface longwave forcing increases with increasing mass median diameter, reaching a maximum at 5 μm and then decreasing with further increase in mass median diameter. This behavior is a result of a similar variation in extinction coefficient (thus optical depth) in the wavelength region of 4–12 μm. When

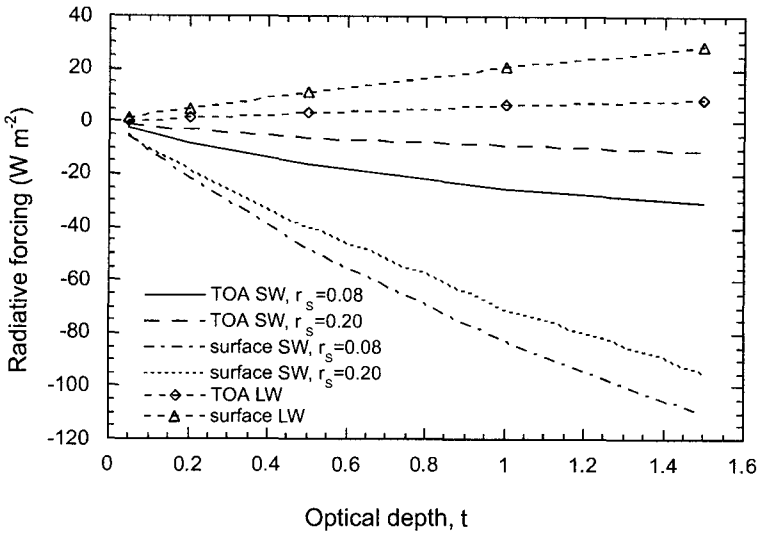

Figure 3.5 TOA and surface diurnally averaged dust radiative forcing (shortwave (SW) and longwave (LW)) as a function of dust optical depth under cloud-free conditions. Dust layer of total column burden 100 mg m^{-2} located over 0–3 km altitude. Mass distribution of dust lognormally distributed with mass median diameter of 3.5 μm and geometric standard deviation of 2.0.

clouds are present, the dust layer exerts nearly zero forcing at both TOA and surface, regardless of particle size distribution.

3.4.4 Dependence of Radiative Forcing on Dust Optical Depth

Radiative forcing as a function of dust optical depth is shown under clear and cloudy conditions in Figures 3.5 and 3.6, respectively. A mass median diameter of 3.5 μm is assumed, and the altitude of the dust layer is fixed at 0–3 km. Under both clear and cloudy conditions, radiative forcing (longwave and shortwave) varies more or less linearly with optical depth at surface albedos characteristic of both ocean (r_s= 0.08) and land (r_s= 0.2) surfaces.

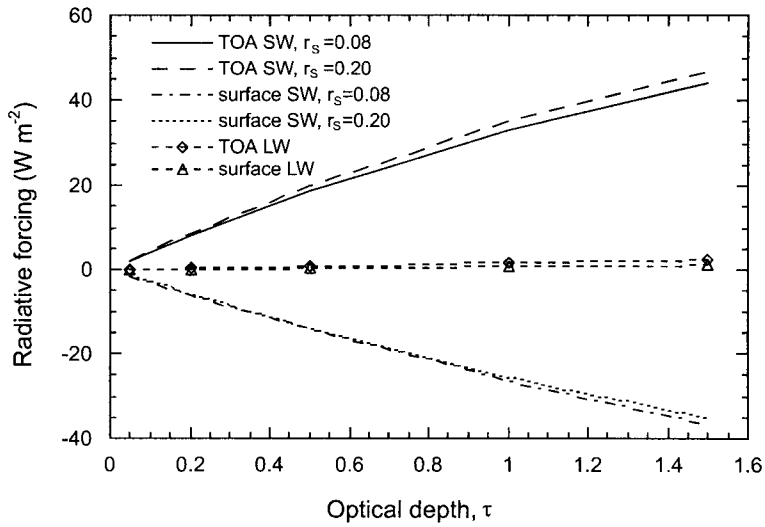

Figure 3.6 TOA and surface diurnally averaged dust radiative forcing (shortwave (SW) and longwave (LW)) as a function of dust optical depth in the presence of a cloud layer. Cloud layer of liquid water content 0.2 g m^{-3} and effective droplet radius 10 μm located between 1 and 1.5 km altitude. Dust layer of total column burden 100 mg m^{-2} located over 0–3 km altitude. Mass distribution of dust lognormally distributed with mass median diameter of 3.5 μm and geometric standard deviation of 2.0.

3.4.5 Dependence of Longwave Forcing on Atmospheric Conditions

We have seen that clear-sky longwave forcing depends on dust layer altitude, dust mass median diameter, and dust optical depth. Longwave radiative forcing also depends on atmospheric conditions, such as temperature profile and water vapor content (Table 3.3). Clear-sky longwave forcing is sensitive to changes in the atmospheric temperature profile. In cases in which we vary atmospheric temperature profile, the surface temperature is changed accordingly, thus the relative temperatures of dust layer, surface, and cloud remain the same. If the change in temperature is not uniform throughout the atmosphere, one can expect a larger or smaller sensitivity of longwave forcing to the actual temperature profile [*Ramanathan*, 1977]. Water vapor content is also a key parameter that affects longwave

Table 3.3 Longwave Forcing(W m^{-2}) for Different Assumptions Concerning Atmospheric Conditions

Surface Temperature K	Temperature Profile	Water Vapor Profile	Longwave Forcing (W m^{-2})			
			No cloud		cloud	
			TOA	Surface	TOA	Surface
Sensitivity to the Atmospheric Temperature Profile						
298	increase 10K throughout U.S. Standard profile	U.S. Standard Atmosphere	0.5	1.6	0.1	0.1
278	decrease 10 K throughout U.S. Standard profile	U.S. Standard Atmosphere	0.3	1.0	0.0	0.0
Sensitivity to the Atmospheric Water Vapor Profile						
288	U.S. Standard Atmosphere	dry case[a]	0.5	1.5	0.1	0.1
288	U.S. Standard Atmosphere	wet case[b]	0.2	0.8	0.1	0.0

[a]Dry case has the same vertical characteristics as the U.S. Standard atmosphere except the water vapor mixing ratio is lower (assumed to be 2.4 g/kg) in the lowest 2.5 km.
[b]Wet case has the same vertical characteristics as the U.S. Standard atmosphere except the water vapor mixing ratio is higher (assumed to be 8.0 g/kg) in the lowest 2.5 km.

forcing. By setting the water vapor mixing ratio in the lowest 2.5 km of the U. S. Standard Atmosphere to be 2.4 g kg^{-1} ("dry case") and 8.0 g kg^{-1} ("wet case"), under clear sky conditions, TOA longwave forcing is 0.5 and 0.2 W m^{-2} (25% and -50% change with respect to the base case), and surface forcing is 1.5 and 0.8 W m^{-2} (15% and -38% change with respect to base case) for dry and wet cases, respectively. Thus the drier the atmosphere, the stronger the longwave radiative forcing of dust, a conclusion that is consistent with results presented by *Sokolik et al.* [1998].

3.5 Local Sensitivity of Mineral Dust Radiative Forcing to Refractive Index, Mass Median Diameter, and Optical Depth

Of the variables considered in this study, the most uncertain are imaginary part of the mineral dust refractive index (k), dust mass median diameter (D_{pm}), and dust optical depth (τ). To evaluate the relative sensitivity of the diurnally averaged radiative forcing to these variables, local sensitivity coefficients, as described in Section 3.3, are computed at the base case conditions.

The base case for the sensitivity study assumes that a dust layer of total column burden of 100 mg m^{-2} is located over 0–3 km altitude, with mass median diameter of 3.5 μm. By varying x (x represents k, D_{pm}, and τ) of the base case by 20% (-10% to +10%), we obtain the local sensitivity $x\frac{\partial \Delta \overline{F}}{\partial x}$ over ocean (r_s= 0.08) and land surfaces (r_s= 0.20).

Table 3.4 shows the local sensitivity of diurnally averaged radiative forcing to k. We note that TOA shortwave forcing under cloudy sky conditions is more sensitive to k than that under clear-sky conditions, as the cloud layer enhances aerosol absorption above the cloud, thus accentuating the effect of k. On the contrary, surface shortwave forcing is more sensitive to k in the absence of the cloud layer than in its presence. For the conditions assumed here, the effect of k on TOA and surface longwave forcing is nonzero only for clear-sky conditions. For net (shortwave plus longwave) forcing, no matter whether clouds are present or not, TOA forcing is more sensitive to variations in k than surface forcing.

The local sensitivity of diurnally averaged radiative forcing to D_{pm} is summarized

in Table 3.5. Shortwave forcing at both TOA and surface in the absence of the cloud layer is much more sensitive to size than when clouds are present, and longwave forcing is not sensitive to particle size at fixed dust column burden.

Sensitivity of radiative forcing to dust optical depth is summarized in Table 3.6. All forcings, except longwave forcing in the presence of clouds, are sensitive to optical depth.

3.6 Critical Single-Scattering Albedo

A first-order estimate of TOA shortwave radiative forcing can be made by calculating the change in planetary albedo resulting from addition of an optically thin aerosol layer. The critical single-scattering albedo ω_{crit}, of an optically thin aerosol layer at

Table 3.4 Radiative Forcing Sensitivity $k(\partial\Delta\overline{F}/\partial k)$ With Respect to the Imaginary Part of the Refractive Index k

Surface Albedo	TOA Sensitivities		Surface Sensitivities	
	No cloud	Cloud	No cloud	Cloud
	Shortwave			
0.08	0.83	1.81	-1.54	-0.83
0.20	1.18	1.97	-1.40	-0.86
	Longwave			
	0.5	0	1.0	0
	Net (Shortwave + Longwave)			
0.08	1.23	1.81	-0.54	-0.83
0.20	1.68	1.97	-0.40	-0.86

$\Delta\overline{F}$ is given in W m^{-2}. (Positive values imply that the increase in k produces larger heating or less cooling, while negative values mean less heating or larger cooling.) Base value of k is 0.006 and 0.25 at the wavelengths of 0.5 μm and 10 μm, respectively.

Table 3.5 Radiative Forcing Sensitivity $D_{pm}(\partial\Delta\overline{F}/\partial D_{pm})$ With Respect to the Mass Median Diameter D_{pm}

Surface Albedo	No Cloud		Cloud	
	TOA	Surface	TOA	Surface
		Shortwave		
0.08	3.45	4.95	-0.50	0.95
0.20	2.35	3.90	-0.55	0.90
		Longwave		
	0.5	0	0	0

$\Delta\overline{F}$ is given in W m^{-2}. (Positive values imply that the increase in D_{pm} produces larger heating or less cooling, while negative values mean less heating or larger cooling.) Base value of D_{pm} is 3.5 μm.

Table 3.6 Radiative Forcing Sensitivity $\tau(\partial\Delta\overline{F}/\partial\tau)$ With Respect to Optical Depth τ

Surface Albedo	No Cloud		Cloud	
	TOA	Surface	TOA	Surface
		Shortwave		
0.08	-1.90	-5.22	2.01	-1.50
0.20	-0.75	-4.37	2.15	-1.48
		Longwave		
	0.4	1.23	0.10	0.03

$\Delta\overline{F}$ is given in W m^{-2}. (Positive values imply that the increase in τ produces larger heating or less cooling, while negative values mean less heating or larger cooling.) Base value of τ is 0.05.

which the perturbation in planetary albedo changes from one of cooling to one of heating, is given by [*Chýlek and Coakley*, 1974; *Seinfeld and Pandis*, 1998]

$$\omega_{crit} = \frac{2r_s}{2r_s + \beta(1 - r_s)^2} \tag{3.2}$$

where β is the upscatter fraction of the particles. Values of $\omega > \omega_{crit}$ lead to cooling; values of $\omega < \omega_{crit}$ to heating.

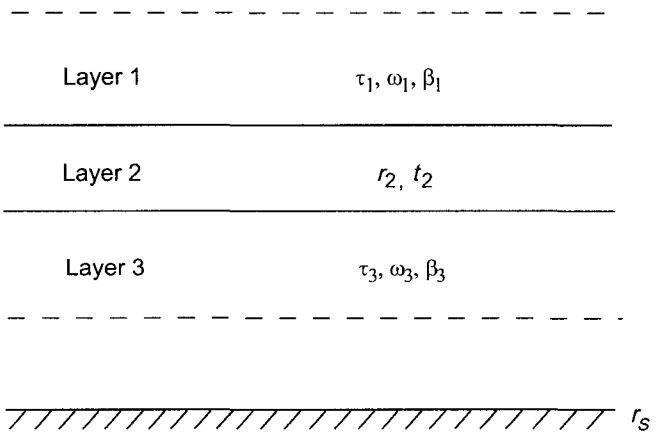

Figure 3.7 Three-layer radiative model of atmosphere. Layers 1 and 3 are aerosol layers, with optical depths, single scattering albedos, and upscatter fractions indicated. Layer 2 is the cloud layer, with albedo r_2 and transmittance t_2.

The analysis that leads to equation (3.2) can be extended to the case of interspersed aerosol and cloud layers (Figure 3.7). Layers 1 and 3 are aerosol layers, the optical properties of which are characterized by optical depths τ_1 and τ_3, single-scattering albedo ω, and upscatter fraction β. Layer 2 is a cloud layer with albedo r_2 and transmittance t_2. The Earth's surface is considered as a Lambertian reflector with albedo r_s. If aerosol exists entirely above cloud, then $\tau_3 = 0$; conversely, for an aerosol layer wholly below cloud, $\tau_1 = 0$. We show in the Appendix that the critical single-scattering albedo of the aerosol in this general case is

$$\omega_{crit} = \frac{(r_2+\frac{r_s t_2^2}{1-r_2 r_s})+r_s^2 r_2 t_2^2-r_2(1+r_s^2 t_2^2)(1-4\tau_1)-r_s t_2^2(1+r_s r_2)(1-4\tau)}{2(1+r_s^2 t_2^2)[\tau_1\beta+2r_2(1-\beta)\tau_1+r_2^2\tau_1\beta+\tau_3\beta t_2^2]+r_s t_2^2(1+r_s r_2)[4(1-\beta)\tau+4\beta\tau r_2]} \tag{3.3}$$

Generally β_1 and β_3 should be different because the incident irradiance on the top of layer 1 is direct while that on the top of layer 3 is mainly diffuse. The analysis in the Appendix considers $\beta_1 \neq \beta_3$; for simplicity we assume $\beta_1 = \beta_3 = \beta$ in equation (3.3).

The critical single-scattering albedo obtained by equation (3.3) is shown in Figure 3.8 as a function of surface albedo r_s. As in previous sections, the cloud layer with liquid water content of 0.2 g m^{-3} and effective droplet radius 10 μm is located between 1 and 1.5 km altitude. Based on our calculations, the albedo r_2 and transmission t_2 of the cloud, which are computed by assuming the surface albedo $r_s = 0$ and integrated over all angles of incoming radiation, are 0.61 and 0.32, respectively. The dust layer of total column burden 100 mg m^{-2} has mass median diameter of 3.5 μm. The optical depth τ, asymmetry factor g, and single-scattering albedo ω are obtained by Mie calculations and then averaged over the solar wavelength region by

$$A = \frac{\int A(\lambda)W(\lambda)d\lambda}{\int W(\lambda)d\lambda} \tag{3.4}$$

where A represents τ, g, or ω, and $W(\lambda)$ is TOA incident solar flux. The values of $W(\lambda)$ are given by *Fröhlich and London* [1986]. The upscatter fraction β is calculated using an approximate relation, $\beta = \frac{1}{2}(1 - \frac{7g}{8})$ [*Wiscombe and Grams*, 1976], which is the global mean value. For the dust aerosol parameters assumed, we obtain $\tau = 0.056, \beta = 0.18$, and $\omega = 0.89$.

In Figure 3.8, three cases are considered: (1) all aerosol above cloud ($\tau_3 = 0$), (2) all aerosol below cloud ($\tau_1 = 0$), and (3) aerosol located both above and below cloud, with $\tau_1 = \tau_3$. The critical value of ω is sensitive to the location of the aerosol layers for either type of cloud. For a surface albedo of 0.15, ω_{crit} is largest (about 0.98) when all aerosol lies above the cloud layer, as in this case even a small amount of aerosol absorption leads to heating; ω_{crit} is smallest when all aerosols are located below cloud (about 0.68

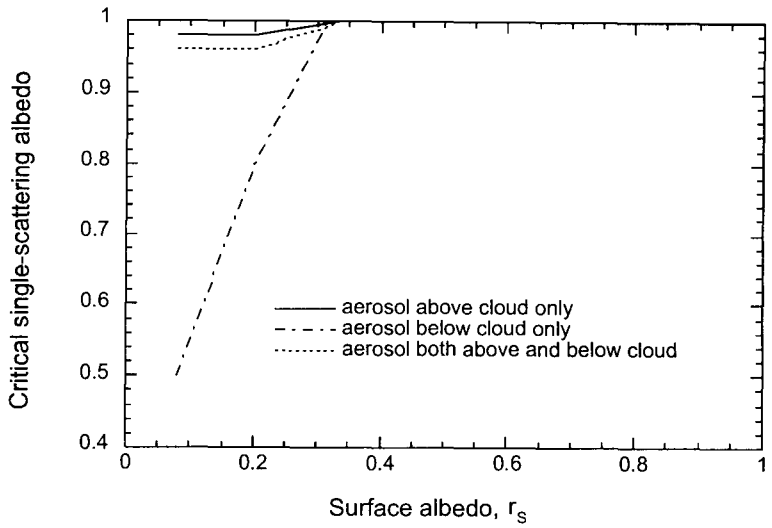

Figure 3.8 Critical single-scattering albedo ω_{crit} as a function of surface albedo and location of the dust layer. The 500 m thick cloud layer has liquid water content of 0.2 g m^{-3} and effective droplet radius 10 μm. $r_2 = 0.61$ and $t_2 = 0.31$. Total column burden of the dust layer is 100 mg m^{-2} and mass median diameter is 3.5 μm (the same as in Figure 3.2).

at $r_s = 0.15$), because only a fraction of incoming radiation reaches the aerosol layer. Consequently, the absorbing component of the particles must be quite substantial to lead to heating. When surface albedo exceeds about 0.5, the aerosol always leads to a heating effect regardless of the value of ω, the reason for which is absorption by surface and cloud. When an aerosol layer is present and surface albedo is high, the surface absorbs more radiation [*Haywood and Shine*, 1997]. According to our definition of TOA aerosol forcing, even though particles are nonabsorbing ($\omega = 1$), $-(F^d_{TOA}\uparrow - F^0_{TOA}\uparrow)$ is positive. Similarly, absorption by cloud also leads to positive aerosol forcing.

Since the parameters of the dust aerosol used for Figure 3.8 are the same as those in Figure 3.2, one can explain the TOA cooling and heating effects shown in Figure 3.2 by comparing ω and ω_{crit}. The spectrally averaged single-scattering albedo of the dust

aerosol is $\omega = 0.89$. It can be seen that ω is always smaller than ω_{crit} for the case with all aerosol above cloud, which explains heating by a dust layer at 3–6 km in Figure 3.2. When all aerosol is below cloud, the curve for crosses over $\omega = 0.89$ at a surface albedo of about 0.25, which is in approximate agreement with the result shown in Figure 3.2; TOA forcing of the dust layer at 0–1 km changes from cooling to heating at a surface albedo of 0.22. We do not compare the case with aerosol both above and below the cloud layer in Figure 3.8 with that in Figure 3.2 because dust is assumed to exist within the cloud layer in the calculations of Figure 3.2, whereas no aerosol is assumed inside the cloud layer in deriving ω_{crit}, although the difference is expected to be small.

It should be mentioned that in the above analysis, water vapor and Rayleigh scattering have been neglected for simplicity. This treatment should not lead to significant error since TOA forcing depends on the difference in planetary albedo instead of on the absolute value of planetary albedo.

3.7 Conclusion

The present work studies the sensitivity of diurnal average mineral dust forcing (TOA and surface) to the imaginary part of dust refractive index, dust particle size, dust altitude, dust optical depth, surface albedo, and the presence or absence of clouds. The sign of net dust forcing (shortwave plus longwave) at TOA depends on surface albedo, particle size, k (imaginary part of refractive index), and the presence or absence of clouds. Results show that low surface albedo and small particle size can produce negative forcing

(cooling) under clear sky conditions, which is consistent with the results obtained by *Tegen and Lacis* [1996] and *Tegen et al.*, [1996]. At the surface, shortwave forcing always leads to cooling, and longwave forcing always leads to heating.

The presence of a low-level stratus cloud greatly alters both shortwave and longwave forcing by mineral dust from the values under clear-sky condition. Though longwave forcing is important under clear-sky condition [*Sokolik et al.*, 1998], it becomes practically negligible when clouds are present. Surface forcing in the presence of a cloud always leads to cooling and is greatly reduced in magnitude compared with clear-sky shortwave forcing. The sign of cloudy sky TOA forcing by dust is determined by the critical single-scattering albedo derived in this study.

Sensitivity studies show the following results:

1. Net TOA forcing is more sensitive to k, the imaginary part of the dust refractive index, than net surface forcing, no matter whether a cloud layer is present or not.

2. Clear-sky shortwave forcing (TOA and surface) is not sensitive to the altitude of the dust layer, but clear-sky longwave forcing (TOA and surface) and cloudy sky TOA shortwave forcing are quite sensitive to it.

3. Shortwave forcing (TOA and surface) under clear-sky conditions is more sensitive to dust mass median diameter than that under cloudy sky conditions. Longwave forcing is not sensitive to particle size.

4. All forcings are sensitive to dust optical depth except cloudy-sky longwave forcing.

Appendix: Derivation of Critical Single-Scattering Albedo for Cloud and Aerosol Layers

Consider the aerosol and cloud layers shown in Figure 3.7. For optically thin aerosol layers the reflectance and transmittance are given by [*Coakley and Chýlek*, 1975; *King and Harshvardhan*, 1986]

$$r_1 = \frac{\tau_1 \omega_1 \beta_1(\mu_0)}{\mu_0} \tag{A1}$$

$$t_1 = 1 - \frac{\tau_1}{\mu_0}[1 - \omega_1 + \omega_1 \beta_1(\mu_0)] \tag{A2}$$

$$r_3 = \frac{\tau_3 \omega_3 \beta_3(\mu_0)}{\mu_0} \tag{A3}$$

$$t_3 = 1 - \frac{\tau_3}{\mu_0}[1 - \omega_3 + \omega_3 \beta_3(\mu_0)] \tag{A4}$$

where μ_0 is the cosine of solar zenith angle. The spherical reflectances and transmissions are obtained by integration of equations (A1)–(A4) over all angles of incoming radiation [*Chýlek and Wong*, 1995]. We obtain

$$r_1 = 2\tau_1 \omega_1 \beta_1 \tag{A5}$$

$$t_1 = 1 - 2\tau_1 + 2\omega_1(1 - \beta_1)\tau_1 \tag{A6}$$

$$r_3 = 2\tau_3 \omega_3 \beta_3 \tag{A7}$$

$$t_3 = 1 - 2\tau_3 + 2\omega_3(1 - \beta_3)\tau_3 \tag{A8}$$

where

$$\beta_i = \int_0^1 \beta_i(\mu_0) d\mu_0 \qquad i = 1, 3$$

By using the adding method [*Liou*, 1980], the combined reflectance and transmittance for layers 1 and 2 are

$$r_{12} = r_1 + \frac{r_2 t_1^2}{1 - r_1 r_2} \tag{A9}$$

$$t_{12} = \frac{t_1 t_2}{1 - r_1 r_2} \tag{A10}$$

Then regarding layers 1 and 2 as a single layer, we get the combined reflectance and transmittance of layers 1, 2, 3 as

$$r_{123} = r_{12} + \frac{r_3 t_{12}^2}{1 - r_{12} r_3} \tag{A11}$$

$$t_{123} = \frac{t_{12} t_3}{1 - r_{12} r_3} \tag{A12}$$

Similarly, the combined reflectance of layers 1, 2, 3 and the surface is

$$r_{123s} = r_{123} + \frac{r_s t_{123}^2}{1 - r_{123} r_s} \tag{A13}$$

Using equations (A5)–(A8) in (A9)–(A13) and neglecting terms involving τ_1^2 and $\tau_1 \tau_2$, one obtains

$$r_{12} \cong 2\tau_1 \omega_1 \beta_1 + r_2[1 - 4\tau_1 + 4\omega_1(1 - \beta_1)\tau_1 + 2\tau_1 \omega_1 \beta_1 r_2] \tag{A14}$$

$$t_{12} \cong [1 - 2\tau_1 + 2\omega_1(1 - \beta_1)\tau_1 + 2\tau_1 \omega_1 \beta_1 r_2] t_2 \tag{A15}$$

$$r_{123} \cong r_{12} + 2\tau_3 \omega_3 \beta_3 t_2^2 \tag{A16}$$

$$t_{123} \cong t_2[1-2\tau_1+2\omega_1(1-\beta_1)\tau_1+2\tau_1\omega_1\beta_1 r_2-2\tau_3+2\omega_3(1-\beta_3)\tau_3+2\tau_3\omega_3\beta_3 r_2] \quad \text{(A17)}$$

$$r_{123s} = r_{123}(1+r_s^2t_2^2) - r_s^2r_2t_2^2 + r_st_2^2(1+r_sr_2)[1-4\tau_1+4\omega_1(1-\beta_1)\tau_1$$

$$+4\tau_1\omega_1\beta_1r_2 - 4\tau_3 + 4\omega_3(1-\beta_3)\tau_3 + 4\tau_3\omega_3\beta_3r_2] \quad \text{(A18)}$$

If we let $\tau_1 + \tau_3 = \tau$, the total optical depth of the aerosol layer, $\beta_1 = \beta_3 = \beta$, and $\omega_1 = \omega_3 = \omega$, then

$$r_{123s} = (1+r_s^2t_2^2)\{2\tau_1\omega\beta + r_2[1-4\tau_1+4\omega(1-\beta)\tau_1+2\tau_1\omega\beta r_2] + 2\tau_3\omega\beta t_2^2\}$$

$$-r_s^2r_2t_2^2 + r_st_2^2(1+r_sr_2)[1-4\tau+4\omega(1-\beta)\tau+4\tau\omega\beta r_2] \quad \text{(A19)}$$

In the absence of aerosols the reflectance of the cloud-surface system is

$$r_{cs} = r_2 + \frac{r_st_2^2}{1-r_2r_s} \quad \text{(A20)}$$

The change in reflectance as a result of the presence of the aerosol layers is $\Delta r_p = r_{123s} - r_{cs}$. Setting $\Delta r_p = 0$ leads to the desired expression for the critical single-scattering albedo of the aerosol, i.e., the value of ω at which Δr_p changes sign,

$$\omega_{crit} = \frac{(r_2+\frac{r_st_2^2}{1-r_2r_s})+r_s^2r_2t_2^2-r_2(1+r_s^2t_2^2)(1-4\tau_1)-r_st_2^2(1+r_sr_2)(1-4\tau)}{2(1+r_s^2t_2^2)[\tau_1\beta+2r_2(1-\beta)\tau_1+r_2^2\tau_1\beta+\tau_3\beta t_2^2]+r_st_2^2(1+r_sr_2)[4(1-\beta)\tau+4\beta\tau r_2]} \quad \text{(A21)}$$

Acknowledgement. This work was supported by the National Science Foundation grant ATM-9614105.

References

Carlson, T. N., and S. Benjamin, Radiative heating rates for Sahara dust, *J. Atmos. Sci., 37*, 193-213, 1980.

Cess, R. D., Nuclear war: Illustrative effects of atmospheric smoke and dust upon solar radiation, *Clim. Change, 7*, 237-251, 1985.

Chýlek, P., and J. A. Coakley, Aerosols and climate, *Science, 183*, 75-77, 1974.

Chýlek, P., and J. T. Kiehl, Sensitivities of radiative-convective climate models, *J. Atmos. Sci., 38*, 1105-1110, 1981.

Chýlek, P., and J. Wong, Effect of absorbing aerosols on global radiation budget, *Geophys. Res. Lett., 22*, 929-931, 1995.

Coakley, J., and P. Chlek, The two-stream approximation in radiative transfer: Including the angle of incident radiation, *J. Atmos. Sci., 32*, 409-418, 1975.

Crisp, D., Absorption of sunlight by water vapor in cloudy conditions: A partial explanation for the cloud absorption anomaly, *Geophys. Res. Lett., 24*, 571-574, 1997.

Dentener, F. J., G. R. Carmichael, Y. Zhang, J. Lelieveld, and P.J. Crutzen, Role of mineral aerosol as a reactive surface in the global troposphere, *J. Geophys. Res., 101*, 22, 869-22, 889, 1996.

Fröhlich, C., and J. London, Revised instruction manual on radiation instruments and measurements, World Clim. Res. Program (WCRP), *Pub. Ser. 7*, WMO TD 149, World Meteorol. Organ., Geneva, 1986.

Fu, Q., and K. N. Liou, Parameterization of the radiative properties of cirrus clouds, *J. Atmos. Sci., 50*, 2008-2025, 1993.

Hansen, J., M. Sato, and R. Ruedy, Radiative forcing and climate response, *J. Geophys. Res., 102*, 6831-6864, 1997.

Haywood, J. M., and K. P. Shine, Multi-spectral calculations of the direct radiative forcing of tropospheric sulfate and soot aerosols using a column model, *Q. J. R. Meteorol. Soc., 123*, 1907-1930, 1997.

King, M. D., and Harshvardhan, Comparative accuracy of selected multiple scattering approximations, *J. Atmos. Sci., 43*, 784-801, 1986.

Lacis, A.A., and M.I. Mishchenko, Climate forcing, climate sensitivity, and climate response: A radiative modeling perspective on atmospheric aerosols, in *Aerosol Forcing of Climate*, edited by R. Charlson and J. Heintzenberg, pp. 11-42, John Wiley, New York, 1995.

Liou, K. N., *An Introduction to Atmospheric Radiation*, Academic, San Diego, Calif., 1980.

Mishchenko, M.I., Light scattering by size-shape distributions of randomly oriented axially symmetric particles of a size comparable to a wavelength, *Appl. Opt., 32*, 4652-4666, 1993.

Mishchenko, M.I., and L.D. Travis, Light scattering by polydispersions of randomly oriented spheroids with sizes comparable to wavelengths of observation, *Appl. Opt.*, 33, 7206-7225, 1994.

Patterson, E.M., D.A. Gillette, and B.H. Stockton, Complex index of refraction between 300 and 700 nm for Saharan aerosols, *J. Geophys. Res. 82*, 3151-3160, 1977.

Ramanathan, V., Interactions between ice-albedo, lapse-rate and cloud-top feedbacks: An analysis of the nonlinear response of a GCM climate model, *J. Atmos. Sci., 34*, 1885-1897, 1977.

Ramaswamy, V., and J.T. Kiehl, Sensitivities of the radiative forcing due to large loading of smoke and dust aerosols, *J. Geophys. Res., 90*, 5597-5613, 1985.

Seinfeld, J. H., and S. N. Pandis, *Atmospheric Chemistry and Physics*. Wiley, New York, 1997.

Sokolik, I. N., A. V. Andronova, and T. C. Johnson, Complex refractive index of atmospheric dust aerosols, *Atmos. Environ., 27A*, 2495-2502, 1993.

Sokolik, I. N., and G. S. Golitsyn, Investigation of optical and radiative properties of atmospheric dust aerosols, *Atmos. Environ., 27A*, 2509-2517, 1993.

Sokolik, I. N., and O. B. Toon, Direct radiative forcing by anthropogenic mineral aerosols, *Nature, 381*, 681-683, 1996.

Sokolik, I.N., O.B. Toon, and R.W. Bergstrom, Modeling the radiative characteristics of airborne mineral aerosols at infrared wavelengths, *J. Geophys. Res. 103*, 8813-8826, 1998.

Tegen, I., and I. Fung, Modeling of mineral dust in the atmosphere: Sources, transport, and optical thickness, *J. Geophys. Res., 99*, 22,897-22,914, 1994.

Tegen, I., and A. A. Lacis, Modeling of particle size distribution and its influence on the radiative properties of mineral dust aerosol, *J. Geophys. Res., 101*, 19,237-19,244, 1996.

Tegen, I., A. A. Lacis, and I. Fung, The influence on climate forcing of mineral aerosols from disturbed soils, *Nature, 380*, 419-422, 1996.

Wiscombe, W. J., and G. W. Grams, The backscattered fraction in two-stream approximations, *J. Atmos. Sci., 33*, 2440-2451, 1976.

Chapter 4

Effects of Aerosols on Tropospheric Photolysis Rates in Clear and Cloudy Atmospheres

[The text of this chapter appears in Liao, H., Yung, Y.L., and Seinfeld, J.H. (1999) *Journal of Geophysical Research*, **104**, 23697–23707.]

ABSTRACT

The effect of aerosols on 14 tropospheric photolysis reactions is examined under noncloudy and cloudy sky conditions by using a detailed one-dimensional radiative transfer model. Pure $(NH_4)_2SO_4$, pure soot, and internal and external mixtures of the two aerosols, as well as mineral dust aerosol, are considered. Nonabsorbing aerosol generally enhances photolysis rates above and in the upper part of the aerosol layer in both noncloudy and cloudy atmospheres, with the enhancement effect reduced in the presence of clouds. In contrast, soot aerosol reduces photolysis rates under both noncloudy and cloudy sky conditions, with the reduction accentuated by a cloud layer. Mixtures of absorbing and nonabsorbing aerosols may produce enhancement or reduction in photolysis rates under clear sky conditions, whereas they generally reduce rates when a cloud is present. In the absence of cloud, sulfate aerosol at urban levels enhances tropospheric average photolysis rates from 11 to 18% for the 14 reactions studied; soot aerosol decreases tropospheric average rates from 6 to 11%. In the presence of a 500-m-thick stratus cloud, sulfate aerosol enhances each of 14 tropospheric average photolysis rates by about 5%; soot aerosol decreases tropospheric average photolysis rates from 9 to 19%.

4.1 Introduction

Solar radiation drives the chemistry of the troposphere through the photodissociation of a number of molecules. The local photolysis rate of an atmospheric species i, $J(i)$ (s^{-1}), is given by

$$J(i) = \int_{\lambda_1}^{\lambda_2} \sigma_i(\lambda, T)\phi_i(\lambda, T)F(\lambda)d\lambda \tag{4.1}$$

where $\sigma_i(\lambda, T)$ (cm^2) is the wavelength and temperature-dependent absorption cross section of species i, $\phi_i(\lambda, T)$ is the quantum yield, and $F(\lambda)$ (photons cm^{-2} nm^{-1} s^{-1}) is the solar actinic flux. In the troposphere, the wavelength range of interest is approximately λ_1= 290 nm to λ_2= 700 nm.

Calculation of photolysis rates requires accurate specification of actinic flux, which in the troposphere depends on solar zenith angle, surface albedo, molecular absorption, Rayleigh scattering, and the presence of clouds and aerosols. The effects of molecular absorption and Rayleigh scattering on actinic flux are relatively well known and are routinely modeled. Among all the absorbing gases, ozone has the most significant effect on tropospheric chemistry by altering photolysis rates [*Liu and Trainer*, 1988; *Thompson et al.*, 1989; *Madronich and Granier*, 1992; *Fuglestvedt et al.*, 1994; *Ma*, 1995]. As shown by *Fuglestvedt et al.* [1994], for the period 1970–1990, stratospheric ozone depletion led to a reduction of 4.5% in global annually averaged total O_3, which increased the global annual average surface photodissociation rate of O_3 to $O(^1D)$ by 6.3%.

Radiative transfer in a cloudy atmosphere and its relation to photochemistry have been studied quite extensively [*Thompson*, 1984; *Madronich*, 1987a,b; *Tsay and Stamnes*,

1992; *van Weele and Duynkerke*, 1993; *Krol and van Weele*, 1997; *Matthijsen et al.*, 1997, 1998; *Crawford et al.*, 1999]. In comparison to clear sky, an optically thick cloud is predicted to increase photolysis rates in the upper part of the cloud and above cloud, while reducing those below cloud.

Aerosols scatter and absorb UV radiation and consequently either enhance or reduce actinic flux and/or photolysis rates. Studies of the effects of aerosols on UV radiation have been carried out by *Liu et al.* [1991], *Forster* [1995], *Reuder et al.* [1996], *Ma and Guicherit* [1997], *Erlick and Frederick* [1998], *Erlick et al.* [1998], *Papayannis et al.* [1998], *Repapis et al.* [1998], *Jacobson* [1999], and *Reuder and Schwander* [1999]. *Ma and Guicherit* [1997] studied the effects of air pollutants on surface UV-B radiation by using a multilayer radiative transfer model and found that the increase of tropospheric pollution in nonurban regions over that last 50–100 years has reduced the surface UV-B, offsetting the effect of the increase due to stratospheric ozone depletion. Recently, *Reuder and Schwander* [1999] showed that potential day-to-day variability in nonurban atmospheric aerosols produces changes of spectrally integrated actinic flux by 10–50%. Jacobson demonstrated that nitrated and aromatic aerosols may be important in reducing UV radiation. Measurements in Athens, Greece, showed that urban aerosols can reduce clear sky UV-B radiation by as much as 40% [*Papayannis et al.*, 1998; *Repapis et al.*, 1998]. Studies of the effects of tropospheric aerosols on photolysis rates have been carried out by *Demerjian et al.* [1980], *Ruggaber et al.* [1994], *Lantz et al.* [1996], *Castro et al.* [1997], *Dickerson et al.* [1997], *Landgraf and Crutzen* [1998], and *Jacobson* [1998]. Scattering aerosols in the boundary layer accelerate photochemical reactions within and above the

aerosol layer [*Ruggaber et al.*, 1994; *Dickerson et al.*, 1997; *Landgraf and Crutzen*, 1998; *Jacobson*, 1998], while absorbing aerosols decrease photolysis rates [*Ruggaber et al.*, 1994; *Dickerson et al.*, 1997; *Jacobson*, 1998]. Effects of aerosols on photolysis rates are sensitive to the aerosol optical depth, single-scattering albedo, and vertical profile, as well as relative humidity and solar zenith angle [*Ruggaber et al.*, 1994].

Even though cloud and aerosol effects have been well studied separately, aerosol effects on photolysis rates in the presence of clouds have not yet been studied systematically. The goal of this work is to evaluate the impact of aerosols on tropospheric photolysis rates, with emphasis on the interaction between cloud and aerosol layers. This interaction is important because stratus clouds, those that are primarily responsible for the reflection of UV and visible radiation, frequently occur near the Earth's surface. Since scattering by aerosols below a low-level stratus cloud can be shielded by the cloud and aerosol absorption above the cloud can be significantly enhanced by the presence of the cloud [*Liao and Seinfeld*, 1998], we expect, as is shown in this study, that the effects of aerosols on photolysis rates in the presence of clouds can be quite different from those under clear sky conditions.

To explore the qualitative effect of aerosol optical properties and to span the range from nonabsorbing to strongly absorbing particles, $(NH_4)_2SO_4$ and soot aerosols are taken as representative of these extremes of tropospheric aerosols, in both internal and external mixtures. We consider also the effect of mineral dust aerosol on photolysis rates.

4.2 Radiative Transfer Model

We calculate actinic flux with the one-dimensional discrete ordinate radiative transfer (DISORT) model [*Stamnes et al.*, 1988]. DISORT uses the discrete ordinate method [*Chandrasekhar*, 1960] to solve the radiative transfer equation, and it uses the δ-M method [*Wiscombe*, 1977] to compute fluxes efficiently in scattering media with strongly asymmetric phase functions. The accuracy of DISORT has been confirmed under both clear and cloudy sky conditions. By comparing $J(NO_2)$ calculated with DISORT with that measured in the summer of 1995 at Greenbelt, Maryland, *Dickerson et al.* [1997] showed that clear sky predictions and measurements of $J(NO_2)$ agreed over a broad range of optical depths and zenith angles. It was shown by *Matthijsen et al.* [1998] that in the presence of clouds, modeled UV irradiances were close to the measured values; the difference was found to be within approximately 5 W m^{-2}.

The vertical resolution, spectral resolution, and number of streams of the code can be selected freely. In this study, we use 80 vertical layers from 0 to 70 km, with a vertical resolution of 100 m in the lowest 3 km, 200 m between 3 and 4 km, 1 km between 4 and 50 km, and 5 km between 50 and 70 km. Pressure, temperature, ozone, and number density of air are from the U.S. Standard Atmosphere (1976). Actinic flux calculations are performed in the wavelength region of 290 - 700 nm, with spectral intervals of 1 nm between 290 and 330 nm, 2 nm between 330 and 600 nm, and 5 nm between 600 and 700 nm. The highest resolution is taken at the shortest wavelengths where ozone absorption changes rapidly and where most photodissociation reactions of interest occur. The number of streams is set equal to 16.

The temperature-dependent ozone absorption cross section data are those reported by *Malicet et al.* [1995] (290–345 nm) at 218 K, 228 K, 243 K, 273 K, and 295 K, and by World Meteorological Organization (WMO) [1985] (345 - 700 nm) at 203 K and 273 K. Solar irradiance data are taken from *Woods et al.* [1996] for wavelengths $\leq$410.5 nm with a wavelength resolution of 1 nm and from *Neckel and Labs* [1984] for wavelengths > 410.5 nm with a resolution of 1 nm (wavelengths $\leq$630 nm) and 2 nm (wavelengths >630 nm), respectively. The spectral surface albedo follows that of *Demerjian et al.* [1980] for land surface: 290–400 nm (0.05), 400–450 nm (0.06), 450–500 nm (0.08), 500–550 nm (0.10), 550–600 nm (0.11), 600–640 nm (0.12), 640–660 nm (0.135), and 660–700 nm (0.15).

4.3 Aerosol and Cloud Specification

When $(NH_4)_2SO_4$, soot, and mixtures thereof are present, we assume that an aerosol layer extends from the Earth's surface to 5 km, with the mass concentration of each species decreasing linearly from its value at the surface to 0.1 of its surface value at 3-km altitude and remaining constant from 3 to 5 km. Column burdens of 12.5 mg m^{-2} for $(NH_4)_2SO_4$ and 2.5 mg m^{-2} for soot are representative of continental conditions [*Liao and Seinfeld*, 1998]. For urban conditions, column burdens of 125 mg m^{-2} for $(NH_4)_2SO_4$ and 25 mg m^{-2} for soot are assumed. Whereas an $(NH_4)_2SO_4$ column burden of 125 mg m^{-2} is somewhat high for sulfate alone, this value can account for the presence of other essentially nonabsorbing components, such as nitrate. When mineral dust aerosol is considered, a uniform layer with a column burden of 100 mg m^{-2} is assumed at 3- to 6-km altitude. On the basis of the analysis of *Dentener et al.* [1996], 100 mg m^{-2} is roughly

the annual average column dust burden over North Africa and Asia.

Aerosol optical properties are calculated with the code ELSIE [*Sloane*, 1984, 1986; *Sloane and Wolff*, 1985; *Sloane et al.*, 1991]. The dry mass size distributions of $(NH_4)_2SO_4$, soot, and mineral dust particles are assumed to be lognormal, with mean diameter of 0.5 μm and geometric standard deviation of 2.0 for $(NH_4)_2SO_4$, 0.1 μm and 2.0 for soot, and 2.0 μm and 2.0 for mineral dust particles, respectively. Refractive indices for $(NH_4)_2SO_4$, soot, and water are from *Toon et al.* [1976], *World Climate Program* [1986] and *Hale and Querry* [1973], respectively. The refractive index of dust from the world's desert regions varies significantly [*Patterson et al.*, 1977; *Sokolik et al.*, 1993]. For the mineral dust refractive index, we assume a real part of 1.50 and use curve 8 in Figure 1 of *Sokolik et al.* [1993] as the imaginary part, k, in the wavelength region of 290 to 700 nm. (Thus k= 0.006 at 500 nm.) Densities are taken to be 1.76 g cm^{-3} for $(NH_4)_2SO_4$, 1.70 g cm^{-3} for soot, and 2.5 g cm^{-3} for mineral dust. In the lowest 5 km of the U.S. Standard Atmosphere, a uniform relative humidity of 50% is a reasonable approximation and is used to calculate the hygroscopic and optical properties of the aerosol. Liquid water mass associated with pure $(NH_4)_2SO_4$ particles and mixed $(NH_4)_2SO_4$-soot particles is calculated by using gas-aerosol thermodynamic theory [*Pilinis and Seinfeld*, 1987; *Kim et al.*, 1993a,b]. It is assumed that soot and mineral dust are nonhygroscopic.

Particle index of refraction is calculated as a volume-weighted average of the indices of refraction of its components. For an external mixture of $(NH_4)_2SO_4$ (denoted s) and soot (denoted c), the single scattering albedo ω and asymmetry factor g are calculated by [*d'Almeida et al.*, 1991]

$$\omega = \frac{\omega_s \sigma_s + \omega_c \sigma_c}{\sigma_s + \sigma_c} \tag{4.2}$$

$$g = \frac{g_s \omega_s \sigma_s + g_c \omega_c \sigma_c}{\omega_s \sigma_s + \omega_c \sigma_c} \tag{4.3}$$

where σ_s and σ_c are the total extinction cross sections of sulfate and carbon particles, respectively.

When a cloud is present, we assume a stratus cloud layer centered at 950-m altitude with a thickness that can vary from 100 to 1000 m. Nominal cloud thickness is taken to be 500 m. Liquid water content, lwc, within the cloud is assumed to increase linearly with increasing height with a vertically averaged value of 0.2 g m^{-3}. An effective cloud droplet radius r_e of 10 μm is assumed, and the cloud optical depth over a layer of thickness dz is estimated by [*Slingo and Schrecker*, 1982]

$$\tau_{cloud} \approx \frac{3}{2} \frac{\text{lwc} \times dz}{\rho_w r_e} \tag{4.4}$$

where ρ_w is the density of water. The asymmetry factor of the cloud layer is assumed to be 0.85 [*Matthijsen et al.*, 1998]. Aerosol particles are assumed to be present interstitially within the cloud. Since hygroscopic sulfate particles are expected to be scavenged by cloud droplets, this assumption leads to a small overestimation of photolysis rates above clouds and a slight underestimation of those within and below clouds.

A summary of total optical depth of the major atmospheric components considered in this study is given in Table 4.1. Vertical profiles of optical depth are shown in Figure 4.1 for Rayleigh scattering, ozone absorption, and urban sulfate aerosol. The optical depth is

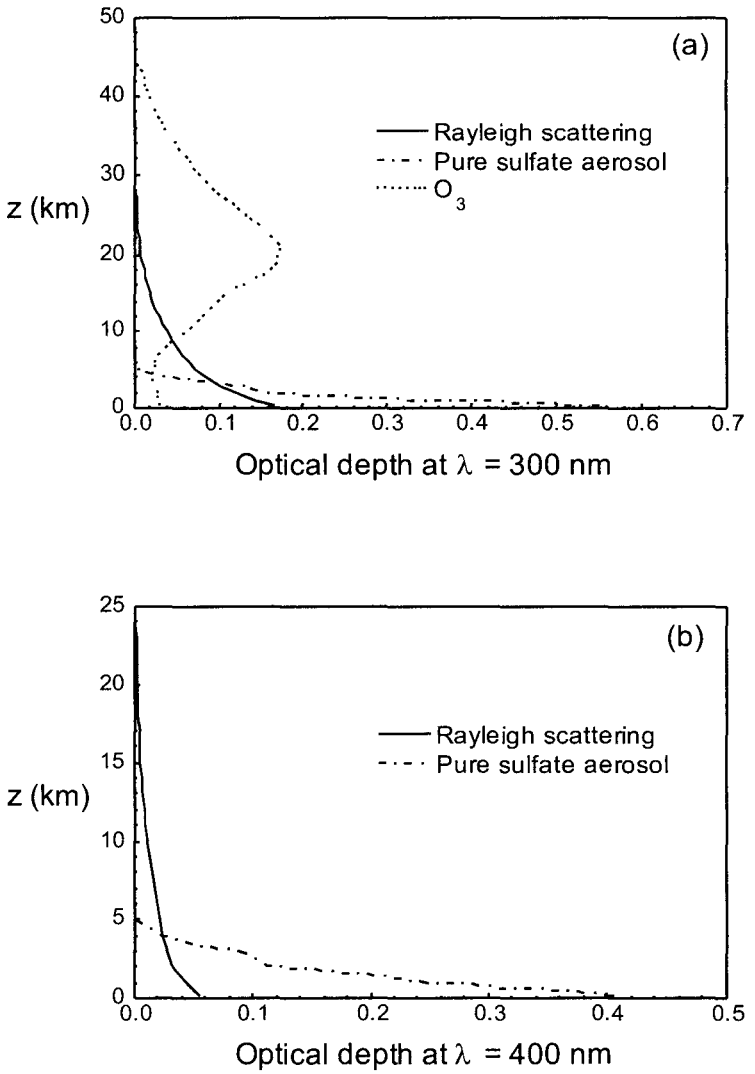

Figure 4.1 Profiles of optical depth per km for Rayleigh scattering, ozone absorption, and urban sulfate scattering at λ= 300 nm (a) and 400 nm (b). Profiles are obtained by dividing the atmosphere into layers of 1 km.

defined as that of a layer of 1-km thickness. The optical depth of Rayleigh scattering and aerosols is larger at UV wavelengths than it is at visible wavelengths; that of mineral dust is more or less constant over these wavelengths (Table 4.1).

Photolysis rates are computed by equation (4.1). Sources of absorption cross section and quantum yield data are listed in Table 4.2 for 14 photolysis reactions of importance in tropospheric chemistry.

4.4 Effects of Aerosols on Tropospheric Photolysis Rates

We have performed detailed calculations of photolysis as a function of altitude, aerosol, and cloud state for all 14 photochemical reactions in Table 4.2; in the interest of space, we present here only $J(O_3 \rightarrow O(^1D))$, $J(NO_2)$, and $J(HCHO)$. Tropospherically averaged photolysis rates are given in Section 4.4.1 for all 14 reactions.

4.4.1 Effect of Sulfate Aerosol on Photolysis Rates

The impact of sulfate aerosol on $J(O_3 \rightarrow O(^1D))$, $J(NO_2)$, and $J(HCHO)$ at 0° solar zenith angle is shown in Figure 4.2. The optical depth of continental sulfate aerosol is 0.057 at 550-nm wavelength, whereas that of sulfate at urban conditions is 0.57 at the same wavelength.

In the absence of clouds and aerosols, $J(O_3 \rightarrow O(^1D))$ exhibits a weak maximum at about 5-km altitude, which results from the competing effect of a decrease in actinic

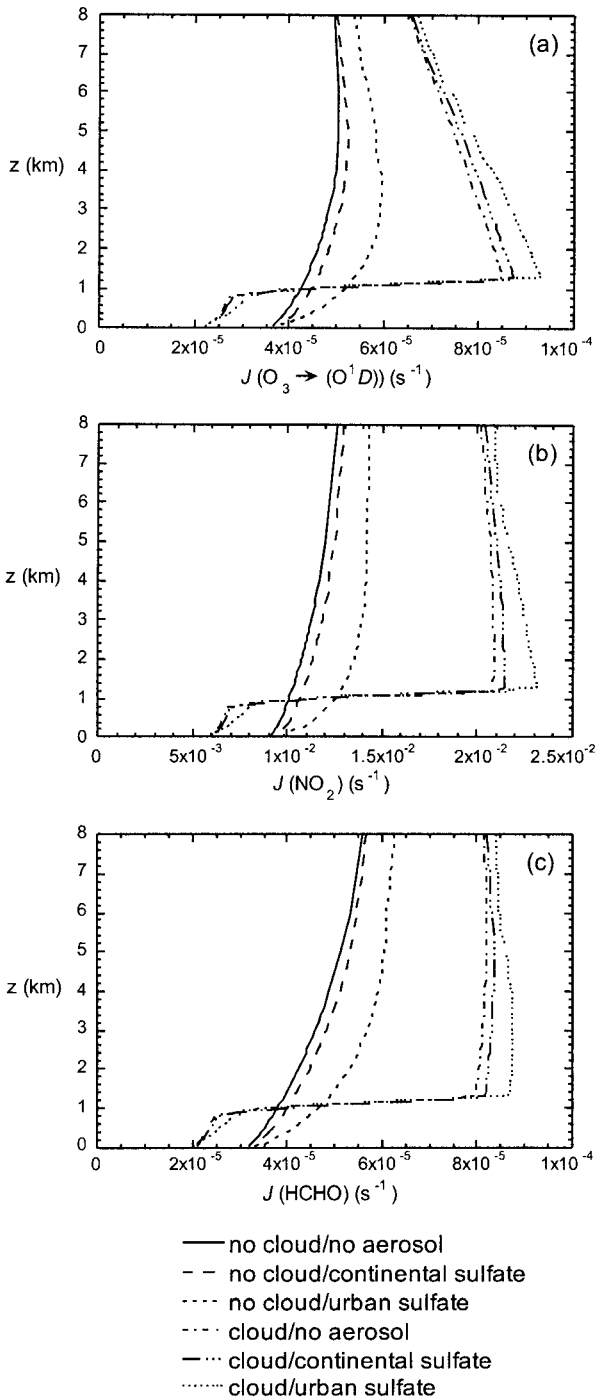

Figure 4.2 Vertical profiles of (a) $J(O_3 \rightarrow O(^1D))$, (b) $J(NO_2)$, and (c) $J(HCHO)$ at 0° solar zenith angle with and without cloud layer. The effect of sulfate aerosol is presented for both continental and urban conditions. Cloud layer has a thickness of 500 m and is centered at 950-m altitude.

Table 4.1 Total Optical depth for Major Atmospheric Components Considered in This Study

Atmospheric Components	Total Optical Depth	
	λ=300 nm	λ=400 nm
Rayleigh molecules	1.22	0.36
Ozone	3.34	0.00
Aerosols		
Pure $(NH_4)_2SO_4$ (continental)	0.13	0.09
Pure $(NH_4)_2SO_4$ (urban)	1.34	0.92
Pure soot (continental)	0.03	0.02
Pure soot (urban)	0.26	0.18
Internal mixture (urban)	1.63	1.12
External mixture (urban)	1.60	1.10
Mineral dust	0.11	0.12
Cloud (500 m thick)	15.0	15.0

flux with decreasing altitude and an increase in temperature (the higher the temperature, the higher the O_3 absorption) with decreasing altitude. When $(NH_4)_2SO_4$ aerosol is added to a clear atmosphere, $J(O_3 \rightarrow O(^1D))$ increases everywhere except at the surface, because the increased diffuse actinic flux offsets the loss in direct actinic flux at the surface. As shown by numerous other studies, the presence of a cloud layer (no aerosol) increases J values above and within the upper part of the cloud, while reducing J values below and within the lower portion of the cloud. The addition of $(NH_4)_2SO_4$ aerosol to the cloudy atmosphere mainly increases $J(O_3 \rightarrow O(^1D))$ above and at the top of the cloud layer, but the magnitude of the increase is smaller than that resulting from $(NH_4)_2SO_4$ aerosol under clear sky conditions, because the cloud layer shields the scattering effect of sulfate aerosol located below the cloud layer. $J(NO_2)$ and $J(HCHO)$ exhibit aerosol and cloud effects similar to those for $J(O_3 \rightarrow O(^1D))$.

To examine the effect of solar zenith angle, we consider urban sulfate only, since the effect of sulfate aerosol at continental background levels on J values is small. At a

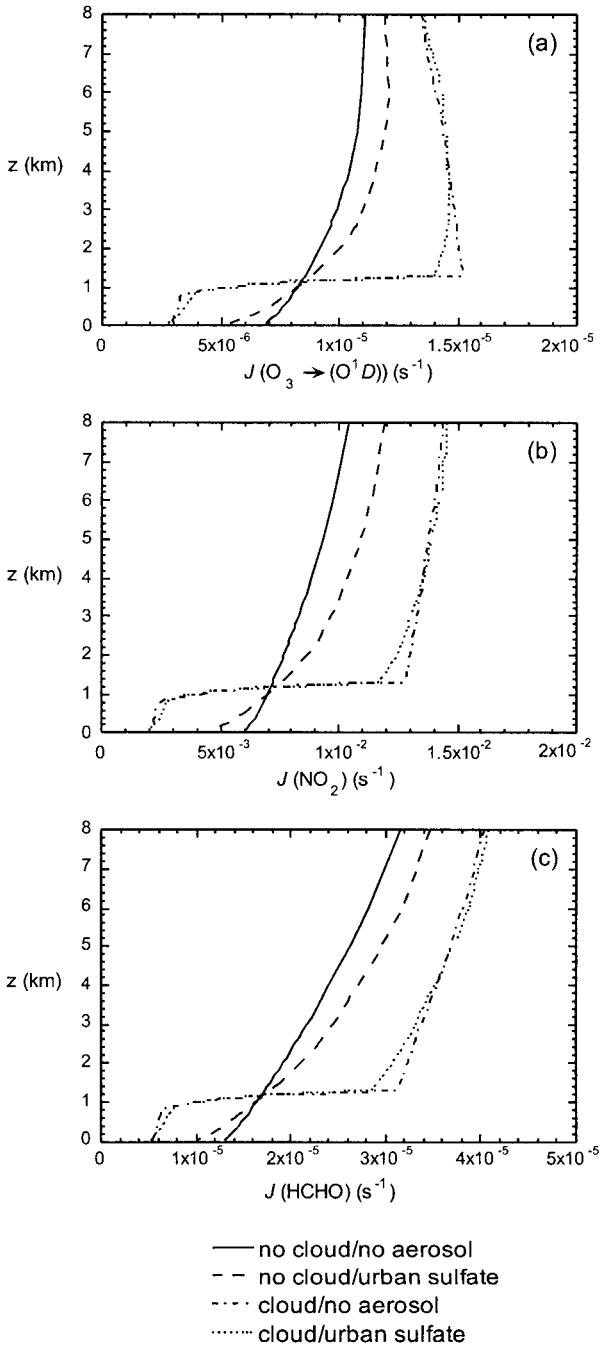

Figure 4.3 Vertical profiles of (a) $J(O_3 \rightarrow O(^1D))$, (b) $J(NO_2)$, and (c) $J(HCHO)$ at 60° solar zenith angle with and without cloud layer. Pure sulfate is at urban conditions. Cloud layer has a thickness of 500 m and is centered at 950-m altitude. Note the horizontal scale is different from that used in Figure 4.2.

solar zenith angle of 60° (Figure 4.3), J values are significantly reduced compared with their values at 0° solar zenith angle (Figure 4.2). There is a crossover of J values for no cloud/no aerosol and no cloud/pure sulfate at an altitude of about 1 km, which is a result of the fact that at larger solar zenith angles the stronger backscattering by sulfate aerosol [*Wiscombe and Grams*, 1976] reduces the available UV flux near the surface but increases it at higher altitudes. Above the cloud layer, urban sulfate aerosol slightly increases J values at higher altitudes (about 4 km here), while it reduces the cloudy sky J values between the top of the cloud layer and 4-km altitude. There are two reasons for this behavior: First, in the scenario considered, about 48% of the total mass of sulfate aerosol is located below the cloud layer. As solar zenith angle increases, the optical path through the cloud increases, producing the same effect as that of a thicker cloud layer. Backscattering by

Table 4.2 Absorption Cross Section and Quantum Yield Data Used in Present Work

Photolysis Reactions	Absorption Cross Section	Quantum Yield (ϕ)	Wavelength Rage, nm
$O_3 \rightarrow O(^3P)+O_2$	*Malicet et al.* [1995] *WMO* [1985]	*DeMore et al.* [1997]	290–700
$O_3 \rightarrow O(^1D)+O_2$	*Malicet et al.* [1995]	*DeMore et al.* [1997][a] *Takahashi et al.* [1998]	290–329
$NO_2 \rightarrow NO+O$	*DeMore et al.* [1997]	*DeMore et al.* [1997]	290–424
$NO_3 \rightarrow NO+O_2$	*Sander* [1986]	*Johnston et al* [1996]	400–691
$NO_3 \rightarrow NO_2+O$	*Sander* [1986]	*Johnston et al* [1996]	400–691
$N_2O_5 \rightarrow NO_3+NO_2$	*DeMore et al.* [1997]	ϕ=1.0	290–380
$H_2O_2 \rightarrow OH+OH$	*DeMore et al.* [1997]	ϕ=1.0	290–350
$HONO \rightarrow OH+NO$	*DeMore et al.* [1997]	ϕ=1.0	310–396
$HO_2NO_2 \rightarrow HO_2+NO_2$	*DeMore et al.* [1997]	ϕ=0.67	290–325
$HO_2NO_2 \rightarrow OH+NO_3$	*DeMore et al.* [1997]	ϕ=0.33	290–325
$HCHO \rightarrow HCO+H$	*DeMore et al.* [1997]	*DeMore et al.* [1997]	301–356
$HCHO \rightarrow CO+H_2$	*DeMore et al.* [1997]	*DeMore et al.* [1997]	301–356
$CH_3OOH \rightarrow CH_3O+OH$	*DeMore et al.* [1997]	ϕ=1.0	290–360
$CH_3COCH_3 \rightarrow$products	*Gierczak et al.* [1998]	*Gierczak et al.* [1998]	290–349

[a]The values of $\phi(O(^1D))$ recommended by *DeMore et al.* [1997] do not include the generation of $O(^1D)$ from spin-forbidden channel $O_3+h\nu \rightarrow O(^1D)+O_2(a^1\Delta_g)$. For this channel a temperature independent quantum yield of 0.08 in the wavelength rage 318–329 nm has been determined by *Takahashi et al.* [1998] and is included in the present calculation.

sulfate aerosol below the cloud layer is almost completely shielded, and the small change in J above the cloud layer is produced solely by sulfate aerosol located above the cloud layer. Second, above the cloud layer, sulfate aerosol has the same effect as it does under clear sky conditions; that is, it increases J values above and within the upper part of the aerosol layer but reduces them within the lower part of the aerosol layer.

4.4.2 Effect of Soot Aerosol on Photolysis Rates

The effect of soot aerosol on $J(O_3 \rightarrow O(^1D))$, $J(NO_2)$, and $J(HCHO)$ at 0° solar zenith angle is shown in Figure 4.4 for continental soot conditions (optical depth τ_{soot}= 0.012 at a wavelength of 550 nm) and for urban soot conditions (τ_{soot}= 0.12 at the same wavelength). Soot aerosol in the cloud-free atmosphere reduces J values at all altitudes, with the maximum reduction occurring near the surface where the soot mass concentration is highest. In the cloudy atmosphere, soot aerosol absorbs both incident radiation and radiation reflected by the high-albedo cloud layer; hence it significantly reduces J values above the cloud layer, with the magnitude of reduction several times higher than that under clear sky conditions.

Under background continental conditions, soot aerosol has a small effect on clear sky J values but can noticeably reduce photolysis rates when clouds are present; for the conditions considered in Figure 4.4, continental soot aerosol can reduce J values above the cloud by about 8%. For a solar zenith angle of 60° (not shown), photolysis rates exhibit the same form as those in Figure 4.4 but shift to smaller values.

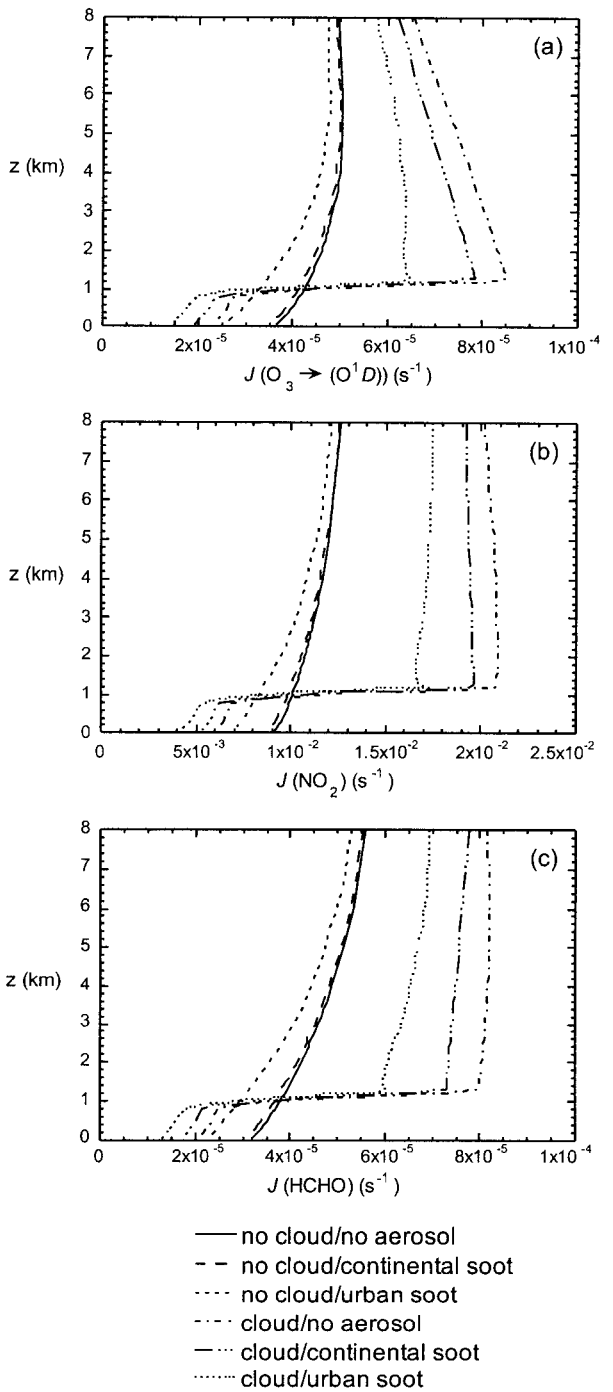

Figure 4.4 Vertical profiles of (a) $J(O_3 \rightarrow O(^1D))$, (b) $J(NO_2)$, and (c) J(HCHO) at 0° solar zenith angle with and without cloud layer. The effect of soot aerosol is presented for both continental and urban conditions. Cloud layer has a thickness of 500 m and is centered at 950-m altitude.

4.4.3 Effect of Internal and External Aerosol Mixtures on Photolysis Rates

Atmospheric aerosols exist as mixtures. For the two species, $(NH_4)_2SO_4$ and soot, in an internal mixture, every particle contains both species, whereas an external mixture consists of pure $(NH_4)_2SO_4$ particles and pure soot particles. With every particle exhibiting some absorption, an internal mixture has a lower single-scattering albedo than the corresponding external mixture does [*Haywood and Shine*, 1995].

$J(O_3 \rightarrow O(^1D))$ in the absence or presence of the 500-m cloud layer is shown in Figure 4.5 for four cases: (1) no aerosol, (2) pure soot, (3) internal mixture, and (4) external mixture. The internal and external mixtures contain the same amount of soot as that in the pure soot aerosol, but they contain additional sulfate aerosol. Figure 4.5a is for 0° solar zenith angle, whereas Figure 4.5b corresponds to 60° solar zenith angle. The behavior of $J(NO_2)$ and $J(HCHO)$ is similar to that of $J(O_3 \rightarrow O(^1D))$ and is not shown here.

Consider first the behavior of $J(O_3 \rightarrow O(^1D))$ at a solar zenith angle of 0°. Under cloud-free conditions, an internal mixture causes a slight reduction in $J(O_3 \rightarrow O(^1D))$ above a certain altitude (2 km for the present conditions), while an external mixture causes an increase in $J(O_3 \rightarrow O(^1D))$ there as a result of the higher single-scattering albedo. Since aerosol concentration is assumed to increase linearly with decreasing altitude, the reduction of $J(O_3 \rightarrow O(^1D))$ by both internal aerosol mixtures and external aerosol mixtures increases rapidly as the altitude decreases. The presence of $(NH_4)_2SO_4$ in the mixtures causes the extinction coefficient of the mixtures to be higher than that of pure soot. Thus the

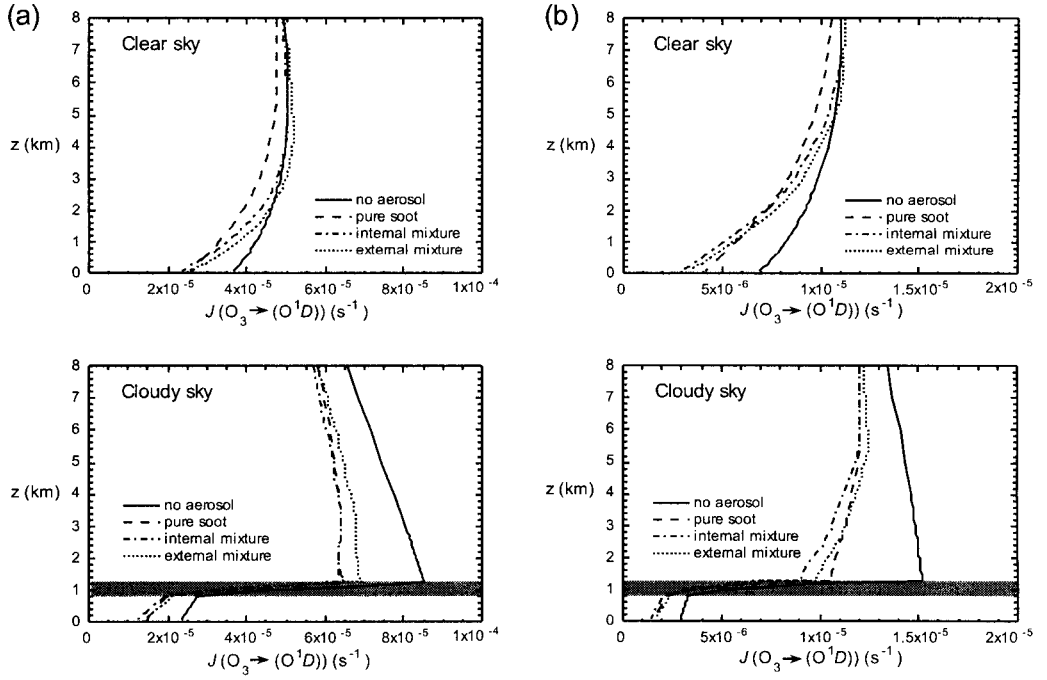

Figure 4.5 Vertical profiles of $J(O_3 \rightarrow O(^1D))$ for pure soot, internal $(NH_4)_2SO_4$-soot, and external $(NH_4)_2SO_4$-soot mixtures with and without cloud layer. Left column (a) is for 0° solar zenith angle and the right column (b) is for 60° solar zenith angle. Shaded region is the cloud layer that has a thickness of 500 m and is centered at 950-m altitude.

reduction in $J(O_3 \rightarrow O(^1D))$ near the surface in the presence of either an internal mixture or an external mixture is greater than that caused by pure soot. When a cloud is present, both internal mixtures and external mixtures reduce $J(O_3 \rightarrow O(^1D))$ at all altitudes, with the internal mixture always leading to a larger reduction than that of the external mixture. Because the absorption coefficient of an internal mixture is larger than that of pure soot, but since the internal mixture also contains sulfate, its scattering effect is much stronger than that of soot alone. In the presence of a thick cloud, absorption is accentuated; thus absorption by the internal mixture becomes stronger that that by pure soot [*Liao and*

Seinfeld, 1998].

At a solar zenith angle of 60°, when no cloud is present, because of the increased upscattering by sulfate at higher solar zenith angles, the mixtures lead to a reduction in $J(O_3 \rightarrow O(^1D))$ below 5-km altitude, producing a crossover of $J(O_3 \rightarrow O(^1D))$ for pure soot and that for mixtures at about 1.5-km altitude. In the presence of the cloud layer, mixtures cause a larger reduction in $J(O_3 \rightarrow O(^1D))$ between the top of the cloud layer and about 4-km altitude than pure soot does.

In summary, aerosol mixtures may either increase or decrease J values under clear sky conditions, depending on the mixture single-scattering albedo, solar zenith angle, and altitude. Regardless of whether aerosol mixtures enhance or reduce J values in a clear atmosphere, they always lead to a reduction in J values in the presence of a cloud.

4.4.4 Effect of Mineral Dust Aerosol on Photolysis Rates

Mineral dust aerosol in the lowest several kilometers of the atmosphere exerts the same effect on photolysis rates as that of the sulfate-soot mixtures studied does. The effect of an elevated layer of mineral dust aerosol on $J(O_3 \rightarrow O(^1D))$ is shown in Figures 4.6a and 4.6b, where a vertically uniform dust layer of column burden 100 mg m^{-2} is assumed to be located at 3–6 km. In a clear atmosphere, at 0° solar zenith angle, the dust layer reduces photolysis rates at all altitudes, with maximum reduction occurring within the dust layer itself. At 60° solar zenith angle, the upscattering by mineral dust is increased; thus maximum reduction in clear sky J shifts to the bottom of or below the dust layer. In the presence of the cloud layer, an elevated dust layer reduces J above cloud at all solar zenith

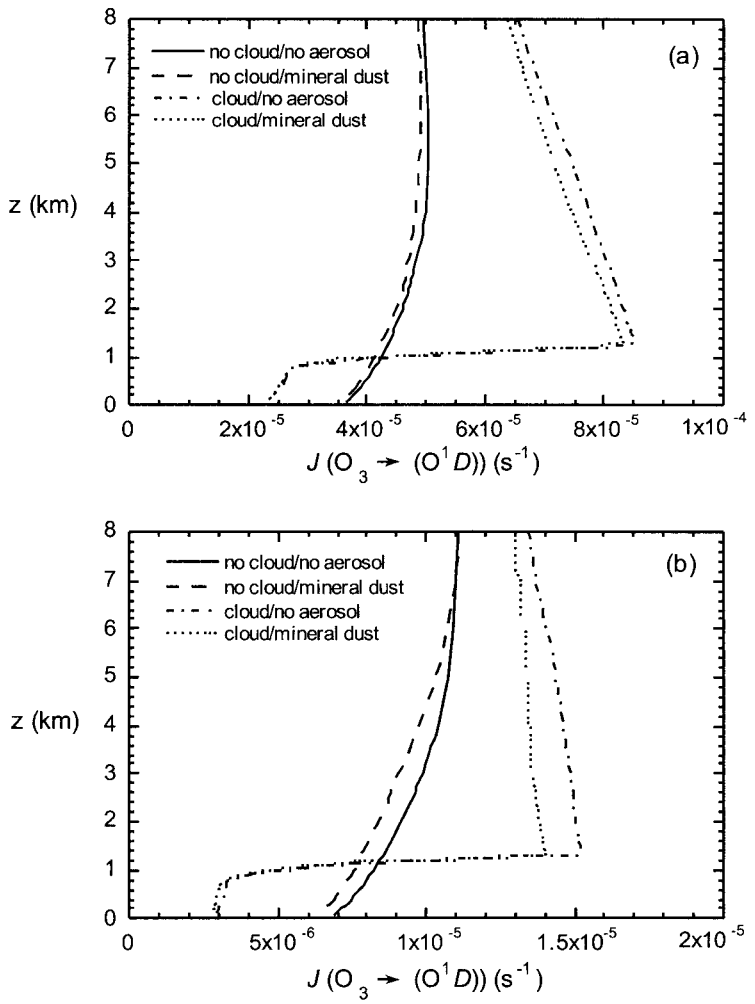

Figure 4.6 Vertical profiles of $J(O_3 \rightarrow O(^1D))$ in the presence of an elevated layer of mineral dust aerosol with and without cloud layer. (a) solar zenith angle = 0° (b) solar zenith angle = 60°. Dust layer is located at 3-6 km, while the 500-m thick cloud layer is centered at 950-m altitude. Note (a) and (b) have different horizontal scales.

angles. The effect of an elevated layer of mineral dust on all other J values is similar to that on $J(O_3 \rightarrow O(^1D))$ and thus is not shown here.

4.5 Effect of Cloud Thickness on Photolysis Rates

To examine the effect of cloud thickness on photolysis rates, we compute $J(O_3 \rightarrow O(^1D))$ (Figure 4.7) at the two altitudes of 5 km (above cloud and at the top of the aerosol layer) and 300 m (below cloud) as a function of cloud thickness. Urban sulfate and soot are considered here at a solar zenith angle of 0°. The behavior of $J(O_3 \rightarrow O(^1D))$ is representative of that of other photolysis reactions.

At 5 km, the presence of sulfate aerosol always increases J values at any cloud thickness, with the fractional increase becoming smaller as the cloud layer gets thicker. This behavior is expected because of the shielding effect of the cloud. In contrast, soot aerosol always reduces J, with the fractional reduction increasing as cloud thickness increases. The larger the cloud albedo, the greater the amount of radiation reflected back to the soot aerosol above the cloud and absorbed.

At 300-m altitude (below cloud), aerosol effects are maximum under clear sky conditions. As the cloud layer becomes thicker, the sulfate effect quickly becomes negligible, whereas the relative reduction in J by soot aerosol gets somewhat smaller.

4.6 Uncertainties in Predicted Effects

Uncertainties in the absolute values of the modeled photolysis rates are not a result of the mathematical methods used to solve the radiative transfer equations. The main sources of inaccuracy are incomplete or insufficient input parameters [*Weihs and Webb*,

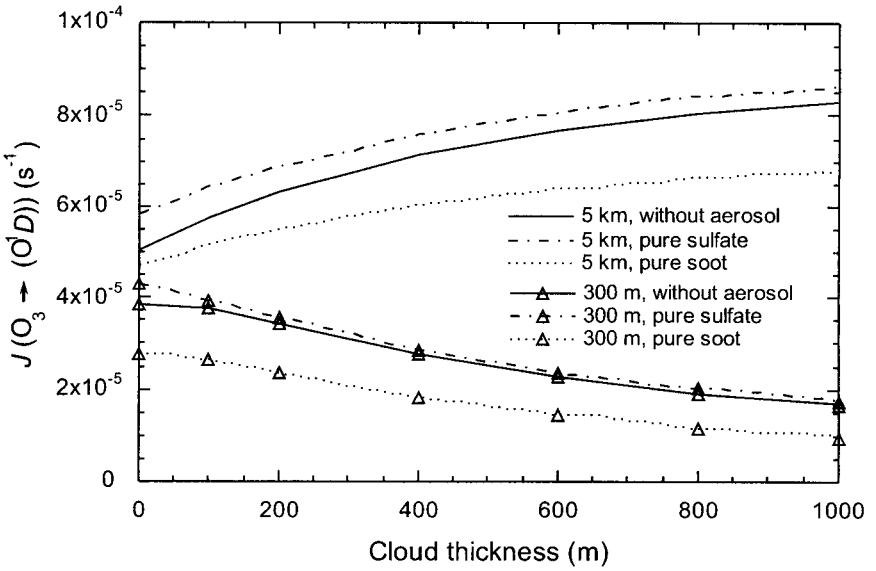

Figure 4.7 $J(O_3 \rightarrow O(^1D))$ at altitudes of 5 km and 300 m as a function of cloud thickness for three cases: (1) no aerosol; (2) pure sulfate aerosol under urban conditions, and (3) pure soot aerosol under urban conditions. Cloud layer of liquid water content 0.2 g m^{-3} and effective droplet radius 10 μm centered at 950-m altitude.

1997; *Reuder and Schwander*, 1999]. Photolysis rates predicted with models depend on parameters that include solar zenith angle, surface albedo, spectral resolution, vertical resolution, number of radiative streams, vertical profile of ozone, absorption cross section and quantum yield data for specific species, as well as optical properties (optical depth, single-scattering albedo, and asymmetry factor) of aerosols and clouds. Sensitivity studies have shown that among these parameters, the most important are solar zenith angle, surface albedo, column burden of ozone, and optical properties of aerosols and clouds [*Demerjian et al.*, 1980; *Ruggaber et al.*, 1994]. Since the effects of solar zenith angle, different aerosol types, and cloud thickness have been studied in previous sections, only the effects of surface albedo and ozone column burden will be discussed here.

We have considered urban and continental aerosols in our study because the effect of marine aerosol is expected to be small as a result of its small optical depth. For land surfaces, the albedo depends on the type and amount of vegetation, the type and moisture content of the soil, snow cover, solar zenith angle, and wavelength. One important land surface condition to examine is a surface with fresh snow cover. A wavelength-independent surface albedo of 0.8 is assumed, and we consider both urban sulfate conditions and urban soot conditions at 0° solar zenith angle. Results are compared with those shown in Figures 4.2 and 4.4 to investigate the effect of surface albedo when it is changed from the value used by *Demerjian et al.* [1980] to 0.8. Qualitatively, effects of aerosols on photolysis rates at high albedo are the same as those obtained with the previous albedo of *Demerjian et al.* [1980] For the case of urban sulfate, the high albedo leads to a decrease in the effect on photolysis rates with increasing height under clear sky conditions, since multiple scattering is strongest near the surface. For the case of urban soot, the high albedo causes a more significant reduction in both clear sky photolysis rates and cloudy sky photolysis rates; while urban soot aerosol reduces photolysis rates by about 10–20% when the surface albedo is that used by *Demerjian et al.* [1980], it can reduce photolysis rates at all altitudes by about 30–40% over high-albedo surfaces.

Ozone column burden may vary by more than 200 Dobson units (DU) within a year [*Ruggaber et al.*, 1994]. This change in ozone column burden can significantly affect the photolysis rates of the species that dissociate at wavelengths <325 nm. However, our tests have shown that the change of ozone column burden simply shifts the photolysis rate of a species to a smaller or larger value; the qualitative results concerning the effects of

aerosols on photolysis rates obtained in sections 4.1-4.4 do not change with varying ozone column burden.

4.7 Tropospheric Averaged Photolysis Rates

Tropospheric averaged photolysis rates for all the reactions in Table 4.2 are presented in Table 4.3 at a cloud thickness of 500 m and a solar zenith angle of 0°. Under clear sky conditions, sulfate aerosol at the urban level increases all J values by 10–18%, while soot aerosol reduces all J values by 6–11%. When the 500-m cloud layer is present, sulfate aerosol increases all J values by about 5%, and soot aerosol reduces J values by amounts between 9 and 19%. The tropospheric average photolysis ratios show again that a cloud layer reduces the effect of sulfate aerosol but enhances that of soot aerosol.

The current results show that urban aerosols produce a change in photolysis rates of the order of 10–20% when averaged through the troposphere. This value can be larger locally. The aerosol effect is significant when we compare it to the general uncertainty in measuring photolysis rates in a clear or cloudy atmosphere. Although the absolute accuracy of photolysis measurements by a spectroradiometer is estimated to be between ± 15 and $\pm 20\%$ depending on the quality of the molecular absorption cross section and quantum yield data, at least three quarters of the uncertainties are of systematic nature caused by the calibration of the detectors [*Shetter and Müller*, 1999]. Thus one can expect that the effect of urban and regional aerosols on photolysis rates should be detectable under both clear sky conditions and cloudy sky conditions and that the effect of absorbing aerosols (in the

Table 4.3 Effects of Urban Sulfate and Soot on Tropospheric Averaged Photolysis Rates

Photolysis Reactions	J_i(no aerosol/no cloud)	J_i(aerosol/no cloud)/ J_i(no aerosol/no cloud)		J_i(no aerosol/cloud)	J_i(aerosol/cloud)/ J_i(no aerosol/cloud)	
		sulfate	soot		sulfate	soot
$O_3 \rightarrow O(^3P)+O_2$	4.92×10^{-4}	1.12	0.93	7.74×10^{-4}	1.05	0.89
$O_3 \rightarrow O(^1D)+O_2$	4.78×10^{-5}	1.15	0.91	6.79×10^{-5}	1.05	0.83
$NO_2 \rightarrow NO+O$	1.16×10^{-2}	1.18	0.92	1.91×10^{-2}	1.05	0.83
$NO_3 \rightarrow NO+O_2$	2.79×10^{-2}	1.11	0.94	4.42×10^{-2}	1.04	0.91
$NO_3 \rightarrow NO_2+O$	2.13×10^{-1}	1.12	0.94	3.42×10^{-1}	1.05	0.90
$N_2O_5 \rightarrow NO_3+NO_2$	4.46×10^{-5}	1.18	0.89	6.86×10^{-5}	1.06	0.81
$H_2O_2 \rightarrow OH+OH$	9.77×10^{-6}	1.17	0.90	1.50×10^{-5}	1.05	0.81
$HONO \rightarrow OH+NO$	2.69×10^{-3}	1.18	0.92	4.37×10^{-3}	1.05	0.83
$HO_2NO_2 \rightarrow HO_2+NO_2$	4.68×10^{-6}	1.16	0.91	6.92×10^{-6}	1.05	0.82
$HO_2NO_2 \rightarrow OH+NO_3$	2.30×10^{-6}	1.16	0.91	3.41×10^{-6}	1.05	0.82
$HCHO \rightarrow HCO+H$	4.92×10^{-5}	1.17	0.90	7.50×10^{-5}	1.05	0.81
$HCHO \rightarrow CO+H_2$	7.22×10^{-5}	1.17	0.91	1.14×10^{-4}	1.05	0.81
$CH_3OOH \rightarrow CH_3O+OH$	8.17×10^{-6}	1.17	0.91	1.26×10^{-5}	1.05	0.81
$CH_3COCH_3 \rightarrow$ Products	1.26×10^{-6}	1.14	0.92	1.81×10^{-6}	1.05	0.83

Cloud thickness is 500 m, and solar zenith angle is 0°.

form of internal or external mixtures) at continental conditions should be detectable in the presence of low-level stratus clouds.

4.8 Conclusions

A one-dimensional radiative model is applied to study the effects of aerosols on tropospheric photolysis rates under both clear sky conditions and cloudy sky conditions. Aerosol types considered are pure sulfate, pure soot, and the mixtures of sulfate and soot, as well as mineral dust. In the absence of clouds, soot aerosol reduces photolysis rates at all altitudes, whereas sulfate aerosol generally increases photolysis rates above and in the upper part of the aerosol layer but reduces photolysis rates in the lower part of the aerosol layer and at the surface. Aerosol mixtures may reduce or increase photolysis rates from those under clear sky conditions, depending on the single-scattering albedo, solar zenith angle, and altitude. An elevated layer of mineral dust aerosol mainly reduces photolysis rates but may increase J values above the layer at high solar zenith angles. The results obtained here for clear sky conditions are consistent with those presented by *Dickerson et al.* [1997] and *Jacobson* [1998].

When a low-level stratus cloud is present, sulfate aerosol may increase photolysis rates above the cloud, but the magnitude of increase is smaller than that resulting from sulfate aerosol under clear sky conditions. Soot aerosol, aerosol mixtures, and mineral dust absorb more radiation and hence reduce photolysis rates above the cloud layer. Even though aerosol mixtures and mineral dust may increase photolysis rates under clear sky

conditions, they always lead to a reduction in J values in the presence of low-level clouds.

Acknowledgement. This work was supported by National Science Foundation grant ATM-9614105 and NASA grant NAG5-3553.

References

Castro, T., L. G. Ruizsuarez, J. C. Ruizsuarez, M. J. Molina, and M. Montero, Sensitivity analysis of a UV-radiation transfer model and experimental photolysis rates of NO_2 in the atmosphere of Mexico City, *Atmos. Environ., 31*, 609–620, 1997.

Chandrasekhar, S., *Radiative Transfer*, Dover, Mineola, N.Y., 1960.

Crawford, J., D. Davis, G. Chen, R. Shetter, M. Müller, J. Barrick, and J. Olson, An assessment of cloud effects on photolysis rate coefficients: Comparison of experimental and theoretical values, *J. Geophys. Res., 104*, 5725–5734, 1999.

d'Almeida, G. A., P. Koepke, and E. P. Shettle, *Atmospheric Aerosols: Global Climatology and Radiative Characteristics*, 261 pp., A. Deepak, Hampton, Va., 1991.

Demerjian, K. L., K. L. Schere, and J. T. Peterson, Theoretical estimates of actinic (spherially integrated) flux and photolytic rate constants of atmospheric species in the lower troposphere, *Adv. Environ. Sci. Technol., 10*, 369–459, 1980.

DeMore, W. B., C. J. Howard, S. P. Sander, A. R. Ravishankara, D. M. Golden, C. E. Kolb, R. F. Hampson, M. J. Molina, and M. J. Kurylo, Chemical kinetics and photochemical data for use in stratospheric modeling, *JPL Publ.*, 97–4, 1997.

Dentener, F. J., G. R. Carmichael, Y. Zhang, J. Lelieveld, and P. J. Crutzen, Role of mineral aerosol as a reactive surface in the global troposphere, *J. Geophys. Res., 101*, 22,869–22,899, 1996.

Dickerson, R. R., S. Kondragunta, G. Stenchikov, K. L. Civerolo, B. G. Doddridge, and B.

N. Holben, The impact of aerosols on solar ultraviolet-radiation and photochemical smog, *Science, 215*, 827–830, 1997.

Erlick, C., and J. E. Frederick, Effects of aerosols on the wavelength dependence of atmospheric transmission in the ultraviolet and visible, 2, Continental and urban aerosols in clear skies, *J. Geophys. Res., 103*, 23,275–23,285, 1998.

Erlick, C., J. E. Frederick, V. K. Saxena, and B. N. Wenny, Atmospheric transmission in the ultraviolet and visible: Aerosols in cloudy atmospheres, *J. Geophys. Res., 103*, 31,541–31,556, 1998.

Forster, P. M. D., Modeling ultraviolet radiation at the Earth's surface, I, The sensitivity of ultraviolet radiances to atmospheric changes, *J. Appl. Meteorol., 34*, 2412–2425, 1995.

Fuglestvedt, J. S., J. E. Jonson, and I. S. A. Isaksen, Effects of reductions in stratospheric ozone on tropospheric chemistry through changes in photolysis rates, *Tellus, Ser. B, 46*, 172–192, 1994.

Gierczak, T., J. B. Burkholder, S. Bauerle, and A. R. Ravishankara, Photochemistry of acetone under tropospheric conditions, *Chem. Phys., 231*, 229–244, 1998.

Hale, G. M., and M. R. Querry, Optical constants of water in the 200 nm to 200 mm wavelength region, *Appl. Opt., 12*, 555–563, 1973.

Haywood, J. M., and K. P. Shine, The effect of anthropogenic sulfate and soot on the clear sky planetary radiation budget, *Geophys. Res. Lett.*, 22, 603–606, 1995.

Jacobson, M. Z., Studying the effects of aerosols on vertical photolysis rate coefficient and temperature profiles over an urban airshed, *J. Geophys. Res.*, 103, 10,593–10,604, 1998.

Jacobson, M. Z., Isolating nitrated and aromatic aerosols and nitrated aromatic gases as sources of ultraviolet light absorption, *J. Geophys. Res.*, 104, 3527–3542, 1999.

Johnston, H. S., H. F. Davis, and Y. T. Lee, NO_3 photolysis product channels: Quantum yields from observed energy thresholds, *J. Phys. Chem.*, 100, 4713–4723, 1996.

Kim, Y. P., J. H. Seinfeld, and P. Saxena, Atmospheric gas aerosol equilibrium, 1, Thermodynamic model, *Aerosol Sci. Technol., 19*, 157–181, 1993a.

Kim, Y. P., J. H. Seinfeld, and P. Saxena, Atmospheric gas-aerosol equilibrium, 2, Analysis of common approximations and activity-coefficient calculation methods, *Aerosol Sci. Technol., 19*, 182–198, 1993b.

Krol, M. C., and M. van Weele, Implications of variations in photodissociation rates for global tropospheric chemistry, *Atmos. Environ., 31*, 1257–1273, 1997.

Landgraf, J., and P. J. Crutzen, An efficient method for online calculations of photolysis and heating rates, *J. Atmos. Sci., 55*, 863–878, 1998.

Lantz, K. O., R. E. Shetter, C. A. Cantrell, S. J. Flocke, J. G. Calvert, and S. Madronich, Theoretical, actinometric, and radiometric determinations of the photolysis rate coefficient of NO_2 during the Mauna Loa Observatory Photochemistry Experiment 2, *J. Geophys. Res., 101*, 14,613–14,629, 1996.

Liao, H., and J. H. Seinfeld, Effect of clouds on direct aerosol radiative forcing of climate, *J. Geophys. Res., 103*, 3781–3788, 1998.

Liu, S. C., and M. Trainer, Responses of the tropospheric ozone and odd hydrogen radicals to column ozone change, *J. Atmos. Chem., 6*, 221–233, 1988.

Liu, S. C., S. A. McKeen, and S. Madronich, Effect of anthropogenic aerosols on biologically active ultraviolet radiation, *Geophys. Res. Lett., 18*, 2265–2268, 1991.

Ma, J., Effects of stratospheric ozone depletion on tropospheric chemistry through changes in UV-B radiation, *TNO-MW-R-95/127*, Neth. Organ. for Appl. Sci., Delft, Netherlands, 1995.

Ma, J., and R. Guicherit, Effects of stratospheric ozone depletion and tropospheric pollution on UV-B radiation in the troposphere, *Photochem. Photobiol., 66*, 346–355, 1997.

Madronich, S., Intercomparison of NO_2 photodissociation and UV radiometer measurements, *Atmos. Environ., 21*, 569–578, 1987a.

Madronich, S., Photodissociation in the atmosphere, 1, Actinic flux and the effects of ground reflections and clouds, *J. Geophys. Res., 92*, 9740–9752, 1987b.

Madronich, S., and C. Granier, Impact of recent total ozone changes on tropospheric ozone photodissociation, hydroxyl radicals, and methane trends, *Geophys. Res. Lett., 19*, 465–467, 1992.

Malicet, J., D. Daumont, J. Charbonnier, C. Parisse, A. Chakir, and J. Brion, Ozone UV spectroscopy, 2, Absorption cross-sections and temperature-dependence, *J. Atmos.*

Chem., 21, 263–273, 1995.

Matthijsen, J., P. J. H. Builtjes, E. W. Meijer, and G. Boersen, Modeling cloud effects on ozone on a regional scale: A case study, *Atmos. Environ., 31*, 3225–3236, 1997.

Matthijsen, J., K. Suhre, R. Rosset, F. L. Eisele, R. L. Mauldin III, and D. J. Tanner, Photodissociation and UV-radiative transfer in a cloudy atmosphere: Modeling and measurements, *J. Geophys. Res., 103*, 16,665–16,676,1998.

Neckel, H., and D. Labs, The solar radiation between 3300Å and 12500Å, *Sol. Phys., 90*, 205–258, 1984.

Papayannis, A., D. Balis, A. Bais, H. van der Bergh, B. Calpini, E. Durieux, L. Fiorani, L. Jaquet, I. Ziomas, and C. S. Zerefos, Role of urban and suburban aerosols on solar UV radiation over Athens, Greece, *Atmos. Environ., 32*, 2193–2201, 1998.

Patterson, E. M., D. A. Gillette, and B. H. Stockton, Complex index of refraction between 300 and 700 nm for Saharan aerosols, *J. Geophys. Res., 82*, 3151–3160, 1977.

Pilinis, C., and J. H. Seinfeld, Continued development of a general equilibrium model for inorganic multicomponent atmospheric aerosols, *Atmos. Environ., 21*, 2453–2466, 1987.

Repapis, C. C., H. T. Mantis, A. G. Paliatsos, C. M. Philandras, A. F. Bais, and C. Meleti, Case study of UV-B modification during episodes of urban air pollution, *Atmos. Environ., 32*, 2203–2208, 1998.

Reuder, J., T. Gori, L. Kins, and R. Dlugi, Determination of photolysis frequencies of

ozone and nitrogen dioxide during SANA 2: The influence of tropospheric aerosol particles, *Meteorol. Z. N. F., 5*, 234–244, 1996.

Reuder J., and H. Schwander, Aerosol effects on UV radiation in nonurban regions, *J. Geophys. Res., 104*, 4065–4077, 1999.

Ruggaber, A., R. Dlugi, and T. Nakajima, Modeling radiation quantities and photolysis frequencies in the troposphere, *J. Atmos. Chem., 18*, 171–120, 1994.

Sander, S. P., Temperature-dependence of the NO_3 absorption spectrum, *J. Phys. Chem., 90*, 4135–4142, 1986.

Shetter, R. E., and M. Müller, Photolysis frequency measurements using actinic flux spectroradiometry during the PEM-Topics mission: Instrument description and some results, *J. Geophys. Res., 104*, 5647–5661, 1999.

Slingo, A., and H. M. Schrecker, On the shortwave radiative properties of stratiform water clouds, *Q. J. R. Meteorol. Soc., 108*, 407–426, 1982.

Sloane, C. S., Optical properties of aerosols of mixed composition, *Atmos. Environ., 18*, 871–878, 1984.

Sloane, C. S., Effect of composition on aerosol light-scattering efficiencies, *Atmos. Environ., 20*, 1025–1037, 1986.

Sloane, C. S., and G. T. Wolff, Prediction of ambient light scattering using a physical model responsive to relative humidity: Validation with measurements from Detroit, *Atmos. Environ., 19*, 669–680, 1985.

Sloane, C. S., J. Watson, J. Chow, L. Pritchett, and L. W. Richards, Size-segregated fine particle measurements by chemical species and their impact on visibility impairment in Denver, *Atmos. Environ., Part A, 25*, 1013–1024, 1991.

Sokolik, I., A. Andronova, and T. C. Johnson, Complex refractive index of atmospheric dust aerosols, *Atmos. Environ., 27*, 2495–2502, 1993.

Stamnes, K., S. C. Tsay, W. Wiscombe, and K. Jayaweera, Numerically stable algorithm for discrete-ordinate-method radiative transfer in multiple scattering and emitting layered media, *Appl. Opt., 27*, 2502–2509, 1988.

Takahashi, K., N. Taniguchi, Y. Matsumi, M. Kawasaki, and M. N. R. Ashfold, Wavelength and temperature dependence of the absolute O(^1D) production yield from the 305–329 nm photodissociation of ozone, *J. Chem. Phys., 108*, 7161–7172, 1998.

Thompson, A. M., The effect of clouds on photolysis rates and ozone formation in the unpolluted troposphere, *J. Geophys. Res., 89*, 1341–1349, 1984.

Thompson, A. M., M. A. Owens, and R. W. Stewart, Sensitivity of tropospheric oxidants to global chemical and climate change, *Atmos. Environ., 23*, 516–532, 1989.

Toon, O. B., J. B. Pollack, and B. N. Khare, The optical constants of several atmospheric aerosol species: Ammonium sulfate, aluminum oxide, and sodium chloride, *J. Geophys. Res., 81*, 5733–5748, 1976.

Tsay, S. C., and K. Stamnes, Ultraviolet radiation in the arctic: The impact of potential ozone depletions and cloud effects, *J. Geophys. Res., 97*, 7829–7840, 1992.

van Weele, M., and P. G. Duynkerke, Effect of clouds on the photodissociation of NO_2: Observations and modeling, *J. Atmos. Chem., 16*, 231–255, 1993.

Weihs, P., and A. R. Webb, Accuracy of spectral UV model calculations, 1, Consideration of uncertainties in input parameters, *J. Geophys. Res., 102*, 1541–1550, 1997.

Wiscombe, W. J., The delta-M method: Rapid yet accurate radiative flux calculations for strongly asymmetric phase functions, *J. Atmos. Sci., 34*, 1408–1422, 1977.

Wiscombe, W., and G. Grams, The backscattered fraction in two-stream approximations, *J. Atmos. Sci., 33*, 2440–2451, 1976.

Woods, T. N., et al., Validation of the UARS solar ultraviolet irradiances: Comparison with the ATLAS 1 and 2 measurements, *J. Geophys. Res., 101*, 9541–9569, 1996.

World Climate Program, A preliminary cloudless standard atmosphere for radiation computation, report, World Meteorol. Organ., Geneva, 1986.

World Meteorological Organization (WMO), Atmospheric ozone: 1985, Report No. 16, Geneva, 1985.

Chapter 5

Interactions between Tropospheric Chemistry and Aerosols in a Unified GCM Simulation

ABSTRACT

A unified tropospheric chemistry-aerosol model has been developed within the Goddard Institute for Space Studies general circulation model (GCM). The model includes a detailed simulation of tropospheric ozone-NO_X-hydrocarbon chemistry and a thermodynamic representation of sulfate/nitrate/ammonium aerosols. Two-way coupling between aerosols and chemistry provides consistent chemical fields for aerosol dynamics and aerosol mass for heterogeneous processes and calculations of gas-phase photolysis rates. Although the current version of the unified model does not include prognostic treatments of black carbon, organic carbon, and mineral dust aerosols, we include effects of these particles on photolysis and heterogeneous processes by using three-dimensional off-line fields. Considering both mineral dust uptake of HNO_3 and wet scavenging of HNO_3 on ice leads to closer agreement between predicted gas-phase HNO_3 concentrations and measurements than in previous global chemical transport model simulations, especially in the middle to upper troposphere. The unified model also simulates sulfate and nitrate aerosols that are associated with mineral dust. Heterogeneous reactions generally reduce O_3 and non-dust SO_4^{2-} concentrations and may locally increase or reduce non-dust NO_3^- and NH_4^+ concentrations depending on whether dust is present. As a result of the coupling between chemistry and aerosols, global burdens (concentrations) of both gas-phase and aerosol species are predicted to respond nonlinearly to changing emissions of NO_X, NH_3 and sulfur. For example, an across-the-board 50% increase in global NO_X emissions is predicted to increase burdens of gas-phase HNO_3, O_3, non-dust SO_4^{2-}, non-dust NO_3^-, NH_4^+, and dust-associated NO_3^- by 37%, 13%, 4%, 12%, 5%, and 22%, respectively, and to reduce

burdens of NH_3 and dust-associated SO_4^{2-} by 15% and 21%, respectively. The present work represents the first step in the development of a fully-coupled climate/chemistry/aerosol model.

5.1 Introduction

Tropospheric O_3 and aerosols are controlled by a combination of direct and precursor emissions, chemical reactions in the atmosphere, and meteorological processes, each of which has the potential to be affected by climate change with resulting feedbacks. Better understanding of chemistry-aerosol-climate interactions is needed for assessments of future climate change [*National Research Council*, 2001].

A fully coupled chemistry-aerosol-climate model, a so-called unified model, will allow one to address how changes in emissions will affect future abundances of tropospheric O_3, CH_4, and aerosols over the next century. Understanding of chemistry-aerosol-climate interactions is complicated by the many feedbacks from climate change to tropospheric chemistry and aerosols. For example, changes in the atmospheric water cycle affect O_3 photochemistry [*Johnson et al.*, 1999] as well as the formation, optical properties, cloud activating properties, and wet scavenging of aerosols. Changes in tropospheric circulation affect the distributions and hence the radiative forcing of O_3 and aerosols [*Hansen et al.*, 1997]. Changes in stratospheric circulation affect stratosphere-troposphere exchange of O_3 and also modify the UV actinic flux in the troposphere. Rising temperatures affect emissions of NO_X, hydrocarbons, and ammonia [*Yienger and Levy*, 1995; *Guenther*

et al., 1995; *Bouwman et al.*, 1997]. Increasing deep convection enhances the lightning source of NO_X [*Sinha and Tuomi*, 1996; *Tuomi et al.*, 1996]. Increasing sea surface winds promote emissions of dimethylsulfide (DMS) and sea salt aerosol from the oceans [*Intergovernmental Panel on Climate Change (IPCC)*, 2001].

Over the past two decades, global simulations of O_3 and aerosols have evolved from using archived meteorological fields in chemical transport models (CTMs) to on-line simulations within general circulation models (GCMs) that have the potential to account for correlations among chemical, aerosol, and meteorological variables. Tropospheric O_3 chemistry has been modeled in CTMs by *Levy et al.* [1985], *Crutzen and Zimmermann* [1991], *Müller and Brasseur* [1995], *Brasseur et al.* [1998], *Wang et al.* [1998], and in GCMs by *Roelofs and Lelieveld* [1995], *Roelofs et al.* [1997], *Mickley et al.* [1999], and *Roelofs and Lelieveld* [2000]. Global aerosol simulations of sulfate [*Erickson et al.*, 1991; *Langner and Rodhe*, 1991; *Penner et al.*, 1994; *Pham et al.*, 1995; *Chin et al.*, 1996, 2000; *Feichter et al.*, 1996; *Chuang et al.*, 1997; *Lelieveld et al.*, 1997; *Kasibhatla et al.*, 1997; *Kjellstrom*, 1998; *Roelofs et al.*, 1998; *Restad et al.*, 1998; *Koch et al.*, 1999; *Adams et al.*, 1999, 2001; *Barth et al.*, 2000], biomass burning and/or black carbon [*Penner et al.*, 1993; *Cooke and Wilson*, 1996; *Liousse et al.*, 1996; *Cooke et al.*, 1999; *Kanakidous et al.*, 2000], nitrate [*Adams et al.*, 1999, 2001], ammonium [*Dentener and Crutzen*, 1994; *Adams et al.*, 1999, 2001], and mineral dust [*Tegen and Fung*, 1994,1995; *Dentener et al.*, 1996] have been reported. *Roelofs et al.* [1998] considered coupling between tropospheric chemistry and sulfate aerosol but did not systematically examine the interactions between gas-phase chemistry and aerosols.

While concentrations of gas-phase species govern many aspects of the formation and growth of aerosols, particles, in turn, influence gas-phase atmospheric chemistry by altering photolysis rates [*Demerjian et al.*, 1980; *Ruggaber et al.*, 1994; *Lantz et al.*, 1996; *Castro et al.*, 1997; *Landgraf and Crutzen*, 1997; *Dickerson et al.*, 1997; *Jacobson*, 1998; *Liao et al.*, 1999] and by serving as sites for heterogeneous conversion of gas-phase species [*Dentener and Crutzen*, 1993; *Andreae and Crutzen*, 1997]. Previous on-line tropospheric chemistry (aerosol) models generally used off-line aerosol (gas-phase species) fields. For example, concentrations of OH, NO_3, HO_2, or O_3 required in sulfate aerosol simulations have been imported from off-line atmospheric chemistry models [*Feichter et al.*, 1996; *Koch et al.*, 1999, *Adams et al.*, 1999; *Barth et al.*, 2000], and off-line aerosol concentrations have been used in global chemistry models to simulate heterogeneous processes [*Brasseur et al.*, 1998; *Wang et al.* 1998; *Mickley et al.* 1999]. Off-line fields can not account for two-way interactions between tropospheric chemistry and aerosols, which are desired in simulations when climate changes feed back into gas-phase chemistry and aerosols.

To move toward incorporating interactions and feedbacks among tropospheric chemistry, aerosol formation, and climate change in a general circulation model, we report here the development of a unified model that simulates atmospheric chemistry and sulfate/nitrate/ammonium aerosols on-line in the Goddard Institute for Space Studies (GISS) GCM version II prime. This work represents the first phase of the development of the fully coupled model depicted schematically in Figure 5.1. Full simulation of tropospheric chemistry provides consistent chemical fields for aerosol dynamics, including

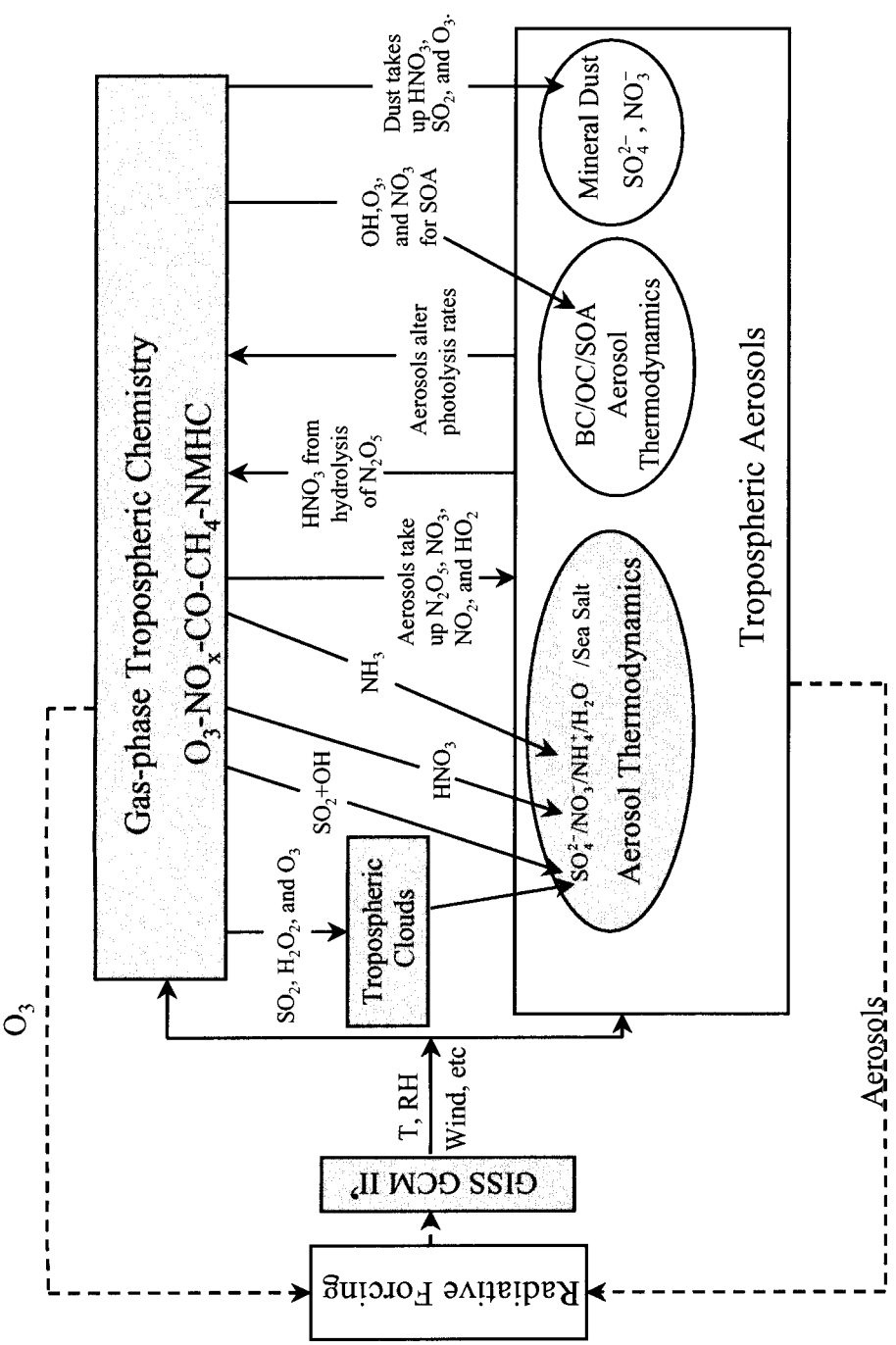

Figure 5.1 Structure of the GCM-atmospheric chemistry-aerosol-climate coupled model. Shaded components and interactions indicated by solid lines are included in the current work. Off-line fields of black carbon (BC), organic carbon (OC, including secondary organic aerosols, denoted SOA), and mineral dust are used for simulations of heterogeneous reactions and photolysis rates. Sea salt aerosol is not included in the current work.

OH, H_2O_2, and O_3 for sulfate formation, HNO_3 for nitrate formation, and NH_3 for ammonium aerosol formation; in turn, the model provides consistent aerosol fields for simulations of heterogeneous processes and gas-phase photolysis rates. Although the version of the unified model presented here does not include prognostic calculations of black carbon (BC), organic carbon (OC), and mineral dust aerosols, we include effects of these particles on photolysis rates and heterogeneous reactions by using three-dimensional monthly mean BC, OC, mineral dust concentration fields. Sea salt aerosol is not included in the current model. The unified model includes the tropospheric chemical mechanism developed by *Mickley et al.* [1999] and the thermodynamic representation of sulfate/nitrate/ammonium aerosols of *Adams et al.* [1999, 2001].

We describe the coupled GCM-atmospheric chemistry-aerosol model in Section 5.2, and discuss the emission inventories in Section 5.3. Section 5.4 presents simulated concentrations of aerosols and related gas-phase species. We discuss the important processes that affect gas-phase HNO_3 concentrations in Section 5.5. In Section 5.6, we examine the effect of aerosols on gas-phase photolysis, and in Section 5.7 we investigate the effects of heterogeneous reactions on predicted concentrations of gas-phase and aerosol species. Section 5.8 studies the sensitivity of predicted concentrations to emissions of NO_X, NH_3, and sulfur. In Section 5.9, we examine the sensitivity of sulfate concentrations to assumptions used in calculations of cloud pH.

5.2 Unified Model

The unified model consists of four major components: (1) the Goddard Institute for Space Studies general circulation model II-prime (GISS GCM II'); (2) the Harvard tropospheric O_3-NO_X-hydrocarbon chemical mechanism [*Mickley et al.*, 1999, and references therein]; (3) the Fast-J scheme for the calculation of atmospheric photolysis rates [*Wild et al.*, 2000]; and (4) the aerosol thermodynamic equilibrium model ISORROPIA [*Nenes et al.*, 1998] for computing the local equilibrium of the aerosol sulfate/nitrate/ammonium/water system.

5.2.1 GISS GCM II'

The GISS GCM II', as described by *Rind and Lerner* [1996] and by *Rind et al.* [1999], has a resolution of 4° latitude by 5° longitude, with 9 vertical layers in a σ-coordinate system extending from the surface to 10 mbar. In comparison with the original GISS GCM II [*Hansen et al.*, 1983], this version has improved treatments of the boundary layer, convection, land surface, and cloud liquid water budget [*Rind and Lerner*, 1996]. The version of GISS GCM II' used in this study employs monthly mean ocean temperature maps. The dynamical time step is 1 h. The variables passed from GISS GCM II' to the tropospheric chemistry and aerosol modules are listed in Table 5.1.

Table 5.1 GCM Variables Passed to Tropospheric Chemistry and Aerosol Modules

GCM variables	For computations of
Frequency and amount of precipitation	Soil NO_X emissions; wet deposition
Frequency of convective events	Lightning NO_X emissions
Boudary layer height	Dry depositon
Surface wind velocity	Dry deposition; DMS emission
Surface albedo	Dry deposition
Cloud optical depth	Dry depositon; Isoprene emission flux; Photolysis rates
Temperature	Reaction rates, Dry deposition; Photolysis rates; Aerosol thermodynamic equilibrium
Relative humidity	Reaction rates; Aerosol thermodynamic equilibrium
Air pressure	Reaction rates; Photolysis rates
Cloud volume fraction	In-cloud sulfate formation

5.2.2 Tropospheric Chemistry

The gas-phase tropospheric chemical mechanism represents tropospheric O_3-NO_X-hydrocarbon chemistry based on 110 chemical species (24 tracers) and 305 chemical reactions. The chemistry subroutines are called every 4 h, and the chemical mechanism is integrated with a fast Gear solver [*Jacobson and Turco*, 1994]. Gas-phase chemical reactions added to the Harvard mechanism to account for sulfate and nitrate aerosol formation are listed in Table 5.2. In addition to the 24 tracers included in the model of *Mickley et al.* [1999], six are added for aerosols: SO_2, SO_4^{2-}, DMS, NH_3, NH_4^+, and NO_3^-. The suite of tracers transported in the GISS GCM II' is listed in Table 5.3.

Table 5.2 Additional Gas-Phase Chemical Reactions Related to Sulate and Nitrate Aerosols

Reaction	Rate (cm^3 $molecule^{-1}$ s^{-1})	Reference
DMS + OH → $0.75SO_2$ + 0.25 MSA	$\frac{1.7\times 10^{-42}\exp(7810/T)[O_2]}{1+5.5\times 10^{-31}\exp(7460/T)[O_2]}$	*Chin et al.* [1996]
DMS + OH → SO_2	$9.6\times10^{-12}\exp(-234/T)$	*Chin et al.* [1996]
DMS + NO_3 →HNO_3 + SO_2	$1.9\times10^{-13}\exp(-520/T)$	*Atkinson et al.* [1992]
SO_2+OH+M→H_2SO_4+M	$k_0(T)[1+k_0(T)/k_\infty]^{-1}F_c^{\{1+[\log_{10}(k_0(T)/k_\infty)]^2\}^{-1}}$ where $k_0(T)=4.0\times10^{-31}(T/300)^{-3.3}$[M] $k_\infty=2\times10^{-12}$ F_c=0.45	*Atkinson et al.* [1992]
NH_3+OH→NH_2+H_2O	$1.7\times10^{-12}\exp(-710/T)$	*DeMore et al.* [1997]

Table 5.3 GCM Chemical Tracers

Tracers	Composition
O_X	$O_3 + O + NO_2 + 2\times NO_3$
NO_X	$NO + NO_2 + NO_3 + HNO_2$
HNO_3	
HNO_4	
N_2O_5	
PAN	Peroxyacetyl nitrate
H_2O_2	
CO	
C_3H_8	
C_2H_6	
ALK4	lumped $\geq C_4$ alkanes
PRPE	lumped $\geq C_3$ alkenes
isoprene	
acetone	
CH_3OOH	
CH_2O	
CH_3CHO	
RCHO	lumped $\geq C_3$ aldehydes
MEK	lumped $\geq C_4$ ketones
methyl vinyl ketone	
methacrolein	
MPAN	peroxymethacryloyl nitrate
PPN	lumped peroxyacyl nitrates
R4N2	lumped alkyl nitrates
SO_2	
SO_4^{2-}	
DMS	
NH_3	
NH_4^+	
NO_3^-	

5.2.2.1 Heterogeneous Reactions

Hydrolysis of N_2O_5 on wetted surfaces of $SO_4^{2-}/NO_3^-/NH_4^+/H_2O$, organic carbon (OC), and mineral dust aerosols is included, and the HNO_3 produced equilibrates between the gas and aerosol phases. We also consider irreversible absorption of NO_3, NO_2, and HO_2 on wetted surfaces of $SO_4^{2-}/NO_3^-/NH_4^+/H_2O$, OC, and mineral dust aerosols. Despite the uncertainties associated with the uptake of SO_2, HNO_3, and O_3 by mineral dust [*Dentener*

et al., 1996], we include those heterogeneous reactions since studies have shown that these reactions are important to gas-phase chemistry [*Dentener et al.*, 1996; *Galy-Lacaux and Modi*, 1998; *Tbazaedeh et al.*, 1998; *Song and Carmichael*, 2001; *Galy-Lacaux et al.*, 2001]. The first-order loss rate of a species on an aerosol surface is represented as shown by *Schwartz* [1986].

Global, three-dimensional mass concentrations of $SO_4^{2-}/NO_3^-/NH_4^+/H_2O$ aerosol are simulated by the unified simulation. We use three-dimensional monthly mean OC concentration fields (S. Chung, personal communication, 2001) generated in a simulation with the same GISS GCM II' meteorology as used here, and mineral dust fields from a different GISS GCM simulation [*Tegen and Fung*, 1994]. Black carbon is assumed not to participate in heterogeneous chemistry. Although we consider water associated with $SO_4^{2-}/NO_3^-/NH_4^+$ aerosol in the calculation of surface area, we do not consider water uptake by OC and mineral dust. Sulfate, organic carbon, black carbon, and mineral dust aerosols are assumed to be externally mixed.

For calculations of heterogeneous chemistry, aerosol size information is needed to obtain aerosol surface area concentration and surface mean radius. We assume a log-normal size distribution for dry $SO_4^{2-}/NO_3^-/NH_4^+$ particles with a median radius of 0.05 μm and geometric standard deviation of 2.0. In each grid cell, the ratio of wet to dry mass of $SO_4^{2-}/NO_3^-/NH_4^+$ aerosol is computed from thermodynamic equilibrium and is used to parameterize the size distribution of wet $SO_4^{2-}/NO_3^-/NH_4^+/H_2O$ aerosol as described by *Adams et al.* [2001]. We also assume a log-normal size distribution for each of OC and mineral dust aerosols, with a median radius of 0.0212 μm and a standard deviation of 2.24

for OC [*Cooke et al.*, 1999], and 0.88 μm and 1.7 for mineral dust [*Zhang and Carmichael*, 1999]. Densities are taken to be 1.8 g cm^{-3} for OC [*Cooke et al.*, 1999], and 2.6 g cm^{-3} for mineral dust [*Zhang and Carmichael*, 1999]. The density of $SO_4^{2-}/NO_3^-/NH_4^+/H_2O$ aerosol depends on its composition and is calculated as described by *Tang* [1997].

The reaction probability γ is assumed to be 0.1, 0.001, 0.0001, and 0.2 for N_2O_5, NO_3, NO_2 and HO_2, respectively [*Jacob*, 2000]. For the uptake of SO_2, HNO_3 and O_3 by mineral dust aerosol, following *Dentener et al.* [1996], we use a reaction probability $\gamma(HNO_3)$ of 0.1, and $\gamma(SO_2)$ of 3×10^{-4} for regions with RH<50% and $\gamma(SO_2)$ of 0.1 when RH>50% [*Dentener et al.*, 1996]. $\gamma(O_3)$ is assumed to be 5×10^{-5} [*Dentener et al.*, 1996]. On mineral dust particles, deposited SO_2 and HNO_3 exist in the forms of SO_4^{2-} and NO_3^-, respectively. Since off-line mineral dust fields are used in this study, dust surface SO_4^{2-} and NO_3^- are predicted as diagnostic variables rather than tracers.

It will turn out to be useful to separate sulfate that is not associated with mineral dust from that formed on mineral dust. Sulfate aerosol, which is emitted directly as primary particles, produced by gas-phase reaction of SO_2 with OH, or produced by in-cloud oxidation of SO_2 by H_2O_2 and O_3, will be denoted as SO_4^{2-}(*nondust*). Sulfate aerosol formed on mineral dust particles will be denoted as SO_4^{2-}(*dust*). Similarly, we denote non-dust nitrate aerosol as NO_3^-(*nondust*), and nitrate that forms on mineral dust particles as NO_3^-(*dust*). *Dentener et al.* [1996] assumed that uptake of SO_2 and HNO_3 by mineral dust takes place only when the dust alkalinity exceeds the acidity from the dust-associated sulfate and nitrate. If alkalinity is contributed by the calcium ion, uptake of SO_2 and HNO_3 occurs when $[Ca^{2+}]$–$[SO_4^{2-}(dust)]$–$0.5[NO_3^-(dust)]>0$. We assume that the Ca^{2+} content

of dust is 5% by weight [*Dentener et al.*, 1996].

Off-line simulated global mineral dust concentrations by *Tegen and Fung* [1994] are used as a basis for calculating heterogeneous reactions. In order to calculate the dust alkalinity, it is necessary to account for the deposition of dust aerosol that contains sulfate and nitrate. Therefore, for each grid cell we assume that the mass of dust deposited is simply balanced by an influx of fresh dust, and the fraction of $SO_4^{2-}(dust)$ and $NO_3^-(dust)$ deposited is the same as the fraction of deposited dust. We use monthly total (dry plus wet) deposition data (in kg m^{-2} $month^{-1}$) from *Tegen and Fung* [1995] and scale the total deposition at the surface to all grid cells above it by assuming that the deposition in a grid cell is proportional to the dust mass contained in it. It should be noted that by assuming in each grid cell the amount of fresh incoming dust is balanced by that deposited during a time step (in order to maintain a fixed global amount of dust), the change of dust alkalinity during transport is not accounted for. After emission, fresh dust particles take up SO_2 and HNO_3 as they are transported; thus, the alkalinity of dust particles in areas far away from source regions should be lower than that of freshly emitted dust particles. Our treatment of mineral dust has the effect of overestimating the dust-associated alkalinity in areas far away from dust sources while underestimating it in dust source regions. Consequently, this assumption may lead to an overestimation of the uptake of SO_2 and HNO_3 by dust removed from sources and an underestimation of uptake close to dust source regions. This treatment will also affect predicted vertical distributions of sulfate and nitrate that are associated with dust because of the assumed vertical distribution of dust deposition. More accurate simulation of dust uptake of gases requires treating both dust amount and dust alkalinity as

Table 5.4 Aqueous Reactions Involved In-Cloud Production of Sulfate

Reactions	k_{298}[a]	E/R	References
	Aqueous Chemistry		
(1) $HSO_3^- + H_2O_2 \rightarrow SO_4^{2-} + 2H^+ + H_2O$	7.45×10^{7}[b]	4759	*Jacob* [1986]
(2) $HSO_3^- + O_3 \rightarrow SO_4^{2-} + H^+ + O_2$	3.7×10^{5}	5300	*Barth et al.* [2000]
(3) $SO_3^{2-} + O_3 \rightarrow SO_4^{2-} + O_2$	1.5×10^{9}	5280	*Barth et al.* [2000]
	Equilibria		
(4) $H_2O_2(g) \rightleftharpoons H_2O_2(aq)$	7.4×10^{4}	-6643	*Jacob* [1986]
(5) $O_3(g) \rightleftharpoons O_3(aq)$	1.15×10^{-2}	-2560	*National Bureau of Standards* [1965]
(6) $SO_2(g) \rightleftharpoons SO_2(aq)$	1.2	-3155	*Jacob* [1986]
(7) $H_2SO_3 \rightleftharpoons HSO_3^- + H^+$	1.3×10^{-2}	-2015	*Maahs* [1982]
(8) $HSO_3^- \rightleftharpoons SO_3^{2-} + H^+$	6.3×10^{-8}	-1505	*Maahs* [1982]

[a] Units for second-order aqueous-phase reactions are $M^{-1}s^{-1}$. Units for solubility constants are M $atom^{-1}$. Units for dissociation constants are M. Reaction rates are of the form $k = k_{298}\exp[-\frac{E}{R}(\frac{1}{T} - \frac{1}{298})]$, unless otherwise noted.

[b] $k = k_{298}\exp[-\frac{E}{R}(\frac{1}{T} - \frac{1}{298})][H^+]$

prognostic tracers.

Figure 5.2 shows the annual average of the monthly mineral dust fields from *Tegen and Fung* [1994]. Mineral dust concentrations are the sum of both natural (undisturbed) and disturbed soils.

5.2.2.2 Aqueous-phase SO_2 Oxidation

Reaction rates and equilibria for aqueous-phase oxidation of SO_2 by H_2O_2 and O_3 are given in Table 5.4. Note that oxidation by O_3 is very sensitive to pH. To compute rates of oxidation, cloud droplet pH is determined based on electroneutrality:

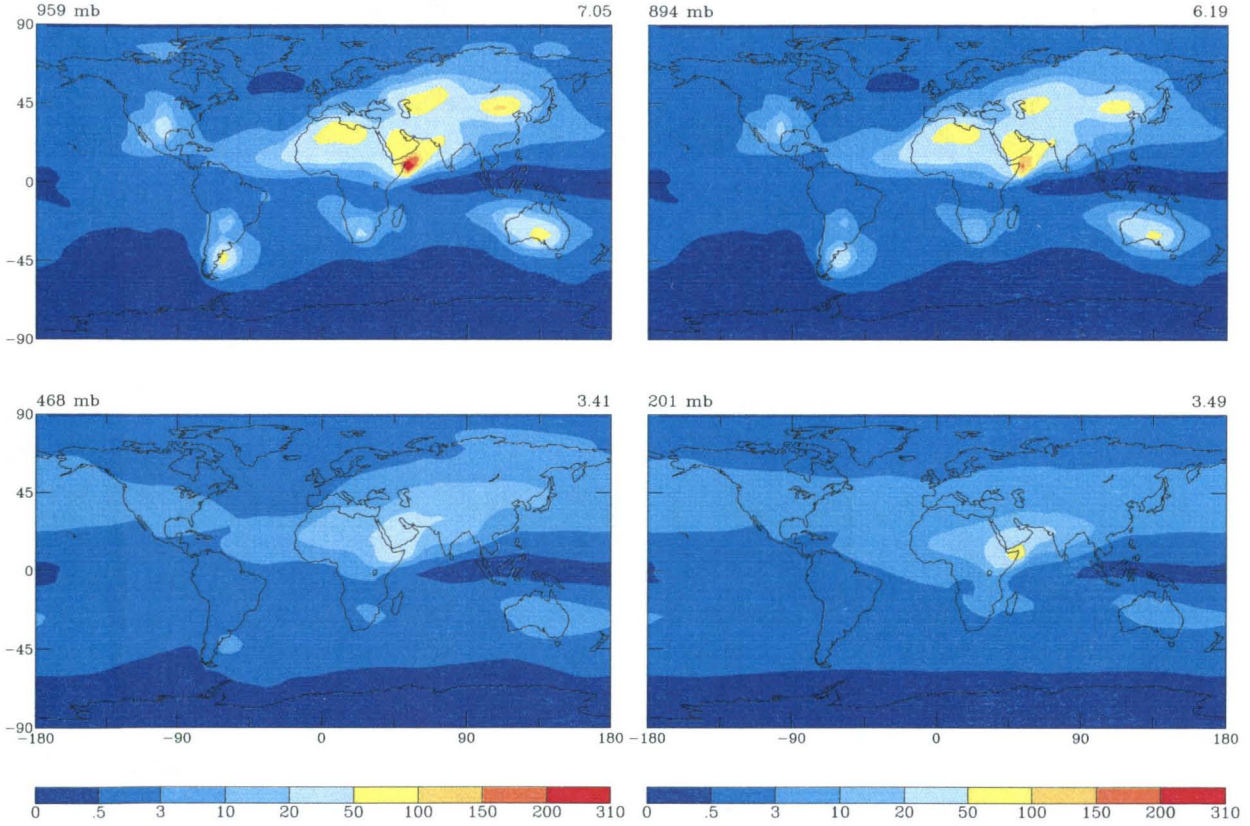

Figure 5.2 Annual average concentration (μg dust/kg air) of the monthly mineral dust fields [*Tegen and Fung*, 1994]. Above each panel, the pressure level of the corresponding model layer is indicated, as is the average concentration in that layer.

$[H^+]=[HSO_3^-]+2[SO_4^{2-}(nondust)]+[NO_3^-(nondust)]-[NH_4^+]$. H_2O_2 and O_3 fields for each grid cell and at each time step are predicted directly from the tropospheric chemistry. To account for changes of pH and of H_2O_2 and SO_2 aqueous-phase concentrations that occur over short time scales, as shown by *Barth et al.* [2000], aqueous-phase chemistry is integrated independently using a 4-min time step.

It should be noted that mineral dust and associated sulfate and nitrate are assumed not to affect cloud pH. This may be an acceptable assumption because the main concentrations of clouds are not over dust source regions. A limitation of the pH calculation is the lack of inclusion of organic acids. We expect to overestimate cloud pH wherever concentrations of organic acids are high.

5.2.3 Gas-Phase Photolysis

Rates of 40 photolysis reactions are computed every 4 h using the Fast-J code of *Wild et al.* [2000], which accounts for absorption by O_2 and O_3, Rayleigh scattering, and Mie scattering by clouds and aerosols, using seven wavelength channels of varying widths covering the spectral range from 289 to 800 nm. We account for effects of $SO_4^{2-}(nondust)/NO_3^-(nondust)/NH_4^+/H_2O$, OC, BC, and mineral dust aerosols on photolysis rates. Mass of $SO_4^{2-}(nondust)/NO_3^-(nondust)/NH_4^+/H_2O$ aerosol, cloud optical depth, temperature, air pressure, surface albedo, and solar zenith angle are passed from the GCM to the Fast-J routine. Monthly mean fields of OC and mineral dust aerosols are those used in the heterogeneous calculations (see Section 5.2.2.1). Monthly mean fields of BC are also from S. Chung (personal communication, 2001). Climatological O_3 distributions

[*McPeters*, 1993] is used in Fast-J since most of the ozone column is in the stratosphere.

Optical properties of clouds and aerosols are calculated by Mie theory [*Hansen and Travis*, 1974]. For temperatures equal to or exceeding 233 K, clouds diagnosed in GCM are assumed to be liquid, the scattering phase functions of which are calculated by assuming a Gamma distribution with constant α=6 and a mode radius of 8.0 μm [*Oliver et al.*, 2000]. At temperatures less than 233 K, clouds are assumed to consist of irregular ice particles, with phase functions calculated following the method of *Mishchenko et al.* [1996]. For calculations of aerosol optical depth and phase functions, refractive indices for "water-soluble" aerosol from *d'Almeida et al.* [1991] are used for SO_4^{2-}(*nondust*)/NO_3^-(*nondust*)/NH_4^+/H_2O and OC. "Water-soluble" aerosol as described in *d'Almeida et al.* [1991] includes sulfates, nitrates, as well as water-soluble organic aerosols. Refractive indices for BC and mineral dust aerosols are from *Liao et al.* [1999]. The size distributions of OC and mineral dust aerosols are those used in computing heterogeneous reactions. For BC, a log-normal distribution with a median radius of 0.0118 μm and a geometric standard deviation of 2.0 is assumed, with the density assumed to be 1.0 g cm^{-3} [*Haywood and Ramaswamy*, 1998]. We assume that wet SO_4^{2-}(*nondust*)/NO_3^-(*nondust*)/NH_4^+/H_2O aerosol has a log-normal distribution with a median radius of 0.09 μm and a geometric standard deviation of 2.0.

Note that for the Fast-J calculation we use the assumed size distribution for SO_4^{2-}(*nondust*)/NO_3^-(*nondust*)/NH_4^+/H_2O aerosol instead of the actual size distribution computed from chemical equilibrium at the local RH. This approximation reduces significantly the computing time needed for calculating aerosol phase functions. (*Lantz*

et al. [1996] showed that when aerosol optical depth is smaller than 0.8, the prevailing situation on the scale of global models, photolysis rates of NO_2 change only about 4% when the aerosol asymmetry factor varies from 0.45 to 0.95. Thus the effect of aerosols on photolysis rates is relatively insensitive to the details of aerosol phase functions in this case.)

5.2.4 Aerosol Equilibrium

Volatile atmospheric species tend to partition themselves between gas and aerosol phases in accordance with thermodynamic equilibrium [*Seinfeld and Pandis*, 1998]. As used by *Adams et al.* [1999] (hereinafter referred to as Adams99), the thermodynamic equilibrium model ISORROPIA [*Nenes et al.*, 1998] is employed to simulate the partitioning of ammonia, nitric acid, and water between gas and aerosol phases. At RH<100%, ISORROPIA computes the equilibrium composition of an internally-mixed aerosol consisting of sulfate, nitrate, chloride, ammonium, sodium, and water. (Sodium and chloride are not considered in the present study.) For the SO_4^{2-}(*nondust*)/NO_3^-(*nondust*)/NH_4^+/H_2O system, the inputs needed by ISORROPIA are the total concentrations of NH_3+NH_4^+, HNO_3+NO_3^-(*nondust*), and SO_4^{2-}(*nondust*), together with the ambient relative humidity and temperature. As discussed in Adams99, we assume aerosol particles exist in a hydrated, metastable state between their crystallization and deliquescence humidities. Since non-dust aerosols and mineral dust are assumed not to interact, sulfate and nitrate associated with mineral dust aerosol do not affect the thermodynamic equilibrium of SO_4^{2-}(*nondust*)/NO_3^-(*nondust*)/NH_4^+/H_2O.

5.2.5 Dry and Wet Deposition

Calculation of dry deposition follows the procedure described by *Wang et al.* [1998]. Deposition velocities of O_3, NO_2, NO, HNO_3, PAN, H_2O_2, CH_2O, SO_2, and NH_3 are determined following the resistance-in-series scheme of *Wesely* [1989]. The dry deposition velocity is inversely proportional to the sum of the aerodynamic resistance, sublayer resistance, and the surface resistance. Aerodynamic and sublayer resistances are calculated using local GCM surface fluxes of momentum and heat. Surface resistances for different species and for different surface types are based largely on the canopy model of *Wesely* [1989], with several improvements as described by *Wang et al.* [1998] to allow its extension to the global scale. Particle deposition velocities are calculated by using the parameters described for sulfate in *Koch et al.* [1999].

The wet deposition scheme is that reported by *Koch et al.* [1999]. Wet deposition of dissolved tracers is treated separately for large-scale and convective clouds, following the GCM cloud schemes described in *Del Genio and Yao* [1993] and Del *Genio et al.* [1996]. Dissolved gases and aerosols are scavenged within and below precipitating clouds. Sulfate, ammonium, and nitrate aerosols are assumed to be fully soluble, and the solubility of gases is determined by their effective Henry's law constants. The scavenged species return to the air if falling precipitation evaporates. We also consider scavenging of gas-phase HNO_3 by ice clouds. Uptake of HNO_3 by ice crystals follows *Lawrence and Crutzen* [1998]. Ice crystals can fall out, evaporate, or persist as determined by GCM cloud scheme.

5.3 Emissions

Estimated present-day global annual emissions are listed in Table 5.5. Emissions for NO_X, CO, and non-methane hydrocarbons follow those in *Mickley et al.* [1999]. Sulfur emissions follow *Koch et al.* [1999]; anthropogenic emissions include seasonally-varying fossil fuel combustion and industrial activities compiled by the Global Emissions of Inventory Activity (GEIA) [*Benkovitz et al.*, 1996], which is representative of 1985 emissions. Three percent of GEIA sulfur emissions are assumed to be sulfate, with the remainder SO_2. Other anthropogenic sources of SO_2 include biomass burning and aircraft emissions. Ammonia emissions are given by *Bouwman et al.* [1997], which take into account the major categories of domesticated animals, fertilizer application, and biomass burning.

5.4 Coupled Chemistry-Aerosol Simulations

The focus of this work is to explore the implications of coupled interaction between gas-phase chemistry and aerosols. Simulations were performed with all components coupled on line, as described in Section 5.2. The baseline simulation considers: (1) the effects of all aerosol classes (SO_4^{2-}(*nondust*)/NO_3^-(*nondust*)/NH_4^+/H_2O, OC, BC, and mineral dust) on photolysis rates; (2) in-cloud oxidation of SO_2 by both H_2O_2 and O_3; and (3) heterogeneous reactions on SO_4^{2-}(*nondust*)/NO_3^-(*nondust*)/NH_4^+/H_2O, OC, and mineral dust aerosol surfaces. All simulations were conducted for an 18-month period, with the first 6 months ignored for spin-up. One year of coupled simulation of global dynamics,

Table 5.5 Global Annual Emissions

Species	Emission rate	
NO_X		
Fossil fuel combustion	20	
Biomass burning	11	
Soil	4.4	
Lightning	3.5	
Aircraft	0.5	
Stratosphere[a]	0.1	
Total	40[b]	(Tg N yr^{-1})
CO		
Fossil fuel combustion	390	
Wood fuel combustion	130	
Biomass burning	510	
Total	1030[b]	(Tg CO yr^{-1})
Isoprene		
Vegetation	550[b]	(Tg C yr^{-1})
Ethane		
Industrial	6.2	
Biomass burning	2.4	
Total	8.6[b]	(Tg C yr^{-1})
Propane[e]		
Industrial	6.7	(Tg C yr^{-1})
$\geq C_4$ alkanes		
Industrial	30[b]	(Tg C yr^{-1})
$\geq C_4$ alkenes		
Industrial	10	
Biogenic sources	16	
Biomass burning	12	
Total	38[b]	(Tg C yr^{-1})
Acetone		
Biomass burning	9	
Biogenic sources	14	
Total	23[b]	(Tg C yr^{-1})
SO_2		
GEIA industrial emissions	66.6	
Biomass burning	2.3	
Aircraft	0.1	
Volcanoes (noneruptive)	3.5	
Total	72.5[c]	(Tg S yr^{-1})
DMS		
Oceanic source	10.7[c]	(Tg S yr^{-1})
NH_3		
Domesticated animals	21.6	
Fertilizers	9.0	
Oceans	8.2	
Biomass burning	5.9	
Crops	3.6	
Humans	2.6	
Soils under natural vegetation	2.4	
Other	0.4	
Total	53.6[d]	(Tg N yr^{-1})

[a] Downward transport of NO_X across the tropopause. This transport also supplies 0.38 Tg N yr^{-1} of HNO_3 globally. [b]*Mickley et al.* [1999]. [c]*Koch et al.* [1999]. [d]*Bouwman et al.* [1997]. [e]Included in the model as a direct emission of acetone; the yield of acetone from oxidation of propane is specified as 80% [*Singh et al.*, 1994].

gas-phase chemistry, and aerosols required about 6 days on one 250-MHz MIPS R10000 processor of a SGI Origin 2100 system.

Gas-phase tropospheric chemistry simulations using the current chemical mechanism have been compared extensively with observations by *Mickley et al.* [1999]; these need not be repeated here. We do focus, however, on the comparison of predicted gas-phase HNO_3 with measurements, since predicted HNO_3 concentrations by the unified model include scavenging of HNO_3 by ice clouds and aerosol interactions and are significantly different from those of *Mickley et al.* [1999]. Aerosol simulations in the unified model follow the sulfate simulation of *Koch et al.* [1999], and the NO_3^- and NH_4^+ simulations of Adams99. Adams99 have presented detailed predictions for SO_4^{2-}(*nondust*), NO_3^-(*nondust*), and NH_4^+ aerosols; based on off-line concentrations of gas-phase HNO_3, HO_2, OH, simulated concentrations were generally within a factor of two of observations. By comparing aerosol predictions from the unified model with those of Adams99, we can examine the effect of full gas-phase/aerosol coupling and the sensitivity of aerosol concentrations to off-line fields.

5.4.1 Sulfur Dioxide

Global SO_2 levels are determined mainly by emissions, dry deposition, dust uptake, and conversion to sulfate. Predicted annual, zonal average mixing ratios of SO_2 are shown in Figure 5.3. As expected, SO_2 exhibits its largest concentrations in the Northern Hemisphere, with annual and zonal average mixing ratios exceeding 1 ppbv in the middle latitudes near the surface. In the Southern Hemisphere, continental and oceanic emissions

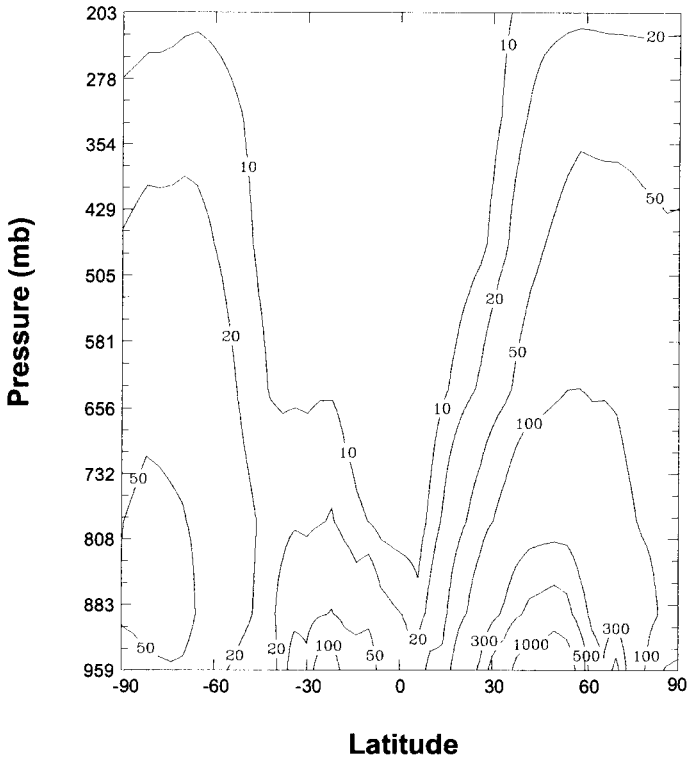

Figure 5.3 Predicted annual, zonal average SO_2 mixing ratios (pptv).

result in a small peak in the subtropics, and emissions of DMS from the oceans produce high latitude, lower tropospheric mixing ratios of about 50 pptv. A comparison of the present predictions to those of *Koch et al.* [1999] shows that in the Northern Hemisphere, current predictions are about 50 pptv lower above about 650 mb in the middle latitudes and throughout the atmosphere at high latitudes. The difference is a result of the inclusion of both in-cloud oxidation of SO_2 by O_3 and uptake of SO_2 by mineral dust aerosol. The importance of in-cloud oxidation by O_3 has been demonstrated by *Rasch et al.* [2000]. We will explore the effect of SO_2 uptake by mineral dust subsequently.

Koch et al. [1999] showed that their simulation led to excessive SO_2 over North America and Europe, with larger biases occurring in the northernmost regions during

wintertime. Inclusion of in-cloud oxidation of SO_2 by O_3 in the unified model improves the comparison with observations. In-cloud SO_2 oxidation by ozone is most important in winter when SO_2 emissions are high and H_2O_2 is limiting.

Table 5.6 presents the yearly-integrated sources and sinks for SO_2. The emissions follow thos of *Kosh et al.* [1999]. Loss of SO_2 through reaction with OH, 7.3 TG S yr^{-2}, is less than the 13.1 TG S yr^{-1}obtained by *Koch et al.* [1999] because of the inclusion of in-cloud SO_2 oxidation by O_3 and dust uptake. Oxidation by OH, H_2O_2, and O_3 accounts for 15%, 65%, and 20% of total SO_2 loss from oxidation pathways, respectively. The 20% loss though oxidation by O_3 agrees well with the result of *Roelofs et al.* [1998]. Dust uptake explains about 5% of the global sink of SO_2.

Table 5.6 Global Budget for SO_2

Sources (Tg S yr^{-1})	
Industrial emissions	64.9
Biomass burning	2.3
Volcanoes	3.4
DMS oxidation	12.4
Total sources	83.0
Sinks (Tg S yr^{-1})	
Oxidaton	
by OH	7.3
by H_2O_2	31.8
O_3	9.5
Dust uptake	3.9
Dry deposition	27.7
Wet deposition	2.8
Total sinks	83.0
Burden (Tg S)	0.26
Residence time (days)	1.1

5.4.2 Sulfate

Figure 5.4 shows predicted annual average SO_4^{2-}(*nondust*) and SO_4^{2-}(*dust*) mixing ratios near the surface and at 468 mb in the baseline simulation. The largest SO_4^{2-}(*nondust*) mixing ratios are predicted over the industrialized areas of Europe, North America, central and eastern Asia. Comparison of the annual averaged SO_4^{2-}(*nondust*) mixing ratios to those of Adams99 shows that the coupled model predicts a 36% higher global mean mixing ratio of SO_4^{2-}(*nondust*) near the surface but about 40% lower global mean mixing ratio in the middle to upper troposphere. The major factors leading to these differences are the inclusion of in-cloud oxidation of SO_2 by O_3 and dust uptake of SO_2. As a result of including in-cloud oxidation of SO_2 by O_3, predicted boundary layer SO_4^{2-}(*nondust*) mixing ratios exceed 1 ppbv in a large area extending from Europe to central Asia. And, since the oxidation of SO_2 by O_3 effectively allows SO_2 scavenging when H_2O_2 is titrated, less SO_2 is transported to higher layers to be subsequently oxidized to sulfate. Our simulation improves the wintertime agreement between predicted SO_4^{2-}(*nondust*) and observations. *Koch et al.* [1999] found that that their predicted SO_4^{2-}(*nondust*) was generally low in Europe during wintertime when in-cloud SO_2 oxidation by ozone is important. Mineral dust takes up SO_2 near the dust source regions but this process is not dominant in determining the global mean mixing ratio of SO_4^{2-}(*nondust*) in the surface layer. The global and annual average burden of SO_4^{2-}(*nondust*) predicted in the unified model is 1.64 Tg, which is 78% of that predicted by Adams99.

Concentrations of SO_4^{2-}(*dust*) depend on the levels of dust aerosol, the alkalinity of the dust particles, the availability of SO_2, and relative humidity (Section 5.2.2.1). The

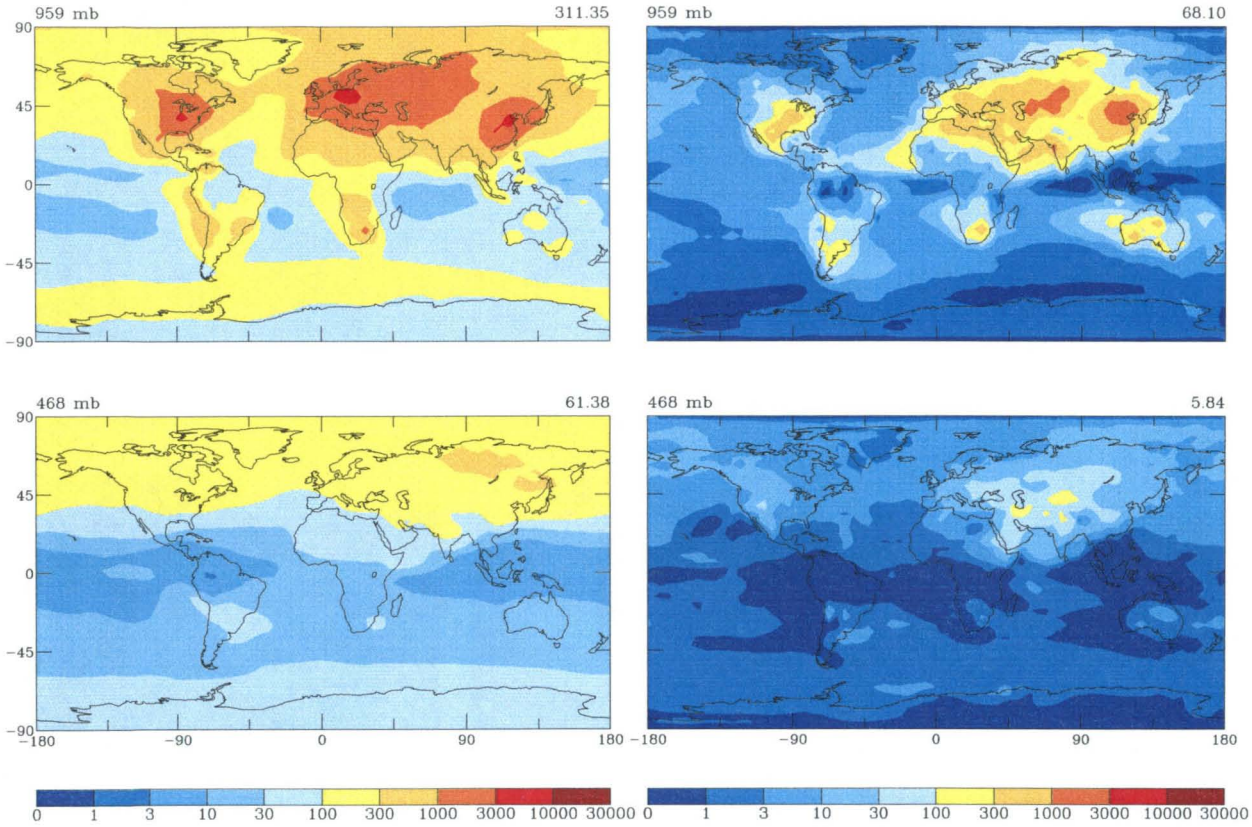

Figure 5.4 Predicted annual average mixing ratios (pptv) of SO_4^{2-}(*nondust*) (left column) and SO_4^{2-}(*dust*) (right column) near the surface and at 468 mb in the baseline simulation. See text for the definitions of SO_4^{2-}(*nondust*) and SO_4^{2-}(*dust*). Note that 1 μg m^{-3} SO_4^{2-} = 258 pptv SO_4^{2-} at 298 K and 1000 mb. Above each panel, the pressure level of the corresponding model layer is indicated, as is the average mixing ratio in that layer.

largest $SO_4^{2-}(dust)$ mixing ratios are predicted over central and northeast Asia.

Figure 5.5(a) shows the predicted percent of annual mean total sulfate occurring on mineral dust at the surface layer. In the vicinity of dust source regions, such as central Asia, northeast Asia, Australia, and the coast of the northern Indian Ocean, more than 50% of total sulfate is predicted to be associated with mineral dust. Over a large portion of the Eurasian continent, 30–50% of total sulfate is predicted to be formed on dust particles. The fraction of sulfate on dust found here is in general agreement with that reported by *Dentener et al.* [1996]. *Dentener et al.* [1996] predicted a maximum located over Western Africa, while the current model predicts maxima over Australia and the northern Indian Ocean, corresponding to dust maxima in Figure 5.2. This difference might be caused either by the different meteorological fields or by the fact that *Dentener et al.* [1996] assumed the North African dust source was strongest in the Sahel region, whereas it was assumed to be strongest somewhat more northerly over Saudi Arabia/Horn of Africa in the study of *Tegen and Fung* [1994], from which the current mineral dust fields are taken.

5.4.3 Nitric Acid

Predicted January and July HNO_3 mixing ratios near the surface and at 468 mb are shown in Figure 5.6. During daytime, nitric acid is produced by the reaction of NO_2 and OH and at night by hydrolysis of N_2O_5 on aerosol surfaces. Gas-phase HNO_3 is removed by reaction with OH, photolysis, wet and dry deposition, as well as by conversion to aerosol nitrate. Predicted Northern Hemisphere HNO_3 mixing ratios are higher in January than in July, reflecting less ventilation, loss of HNO_3 by photolysis, reaction with OH, and

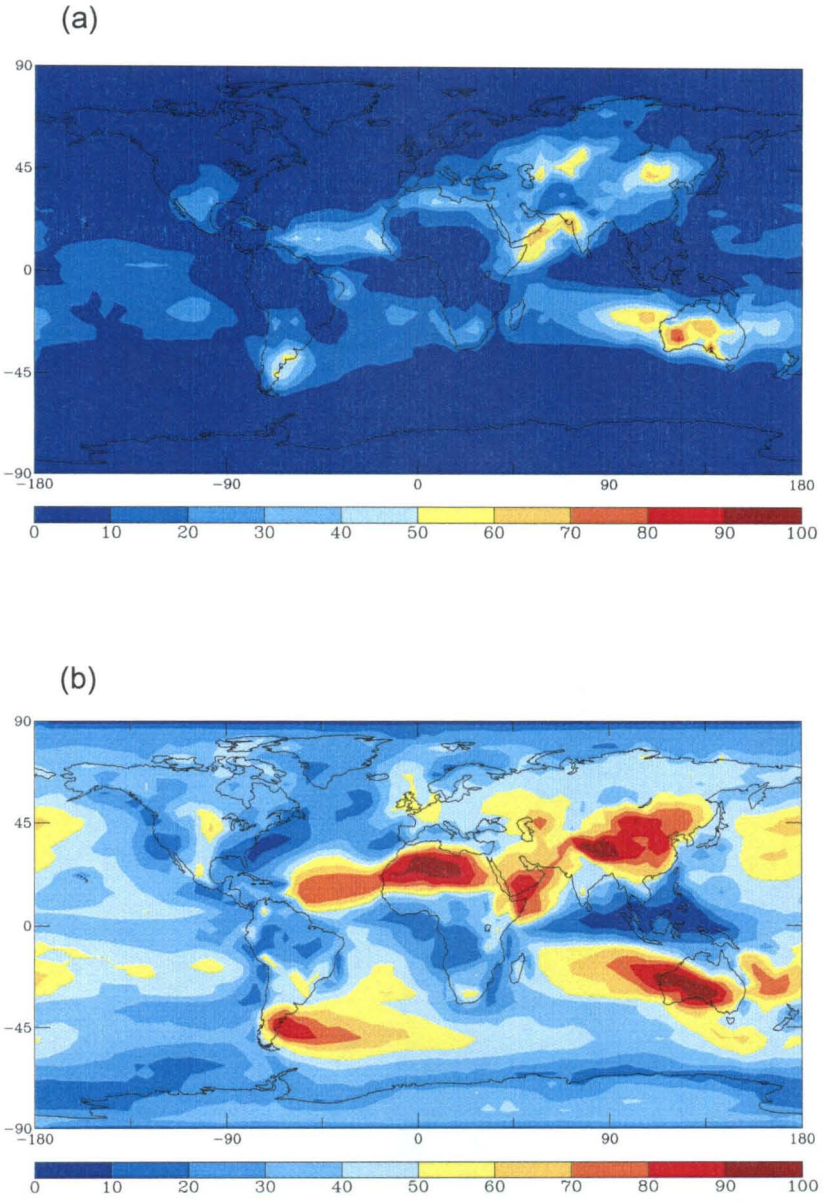

Figure 5.5 (a) Percent of total sulfate ($SO_4^{2-}(nondust)$+$SO_4^{2-}(dust)$) predicted to occur on mineral dust particles in the surface layer; (b) Percent of total nitrate (gas-phase HNO_3+$NO_3^-(nondust)$+$NO_3^-(dust)$) occurring as nitrate aerosol ($NO_3^-(nondust)$+$NO_3^-(dust)$) in the surface layer.

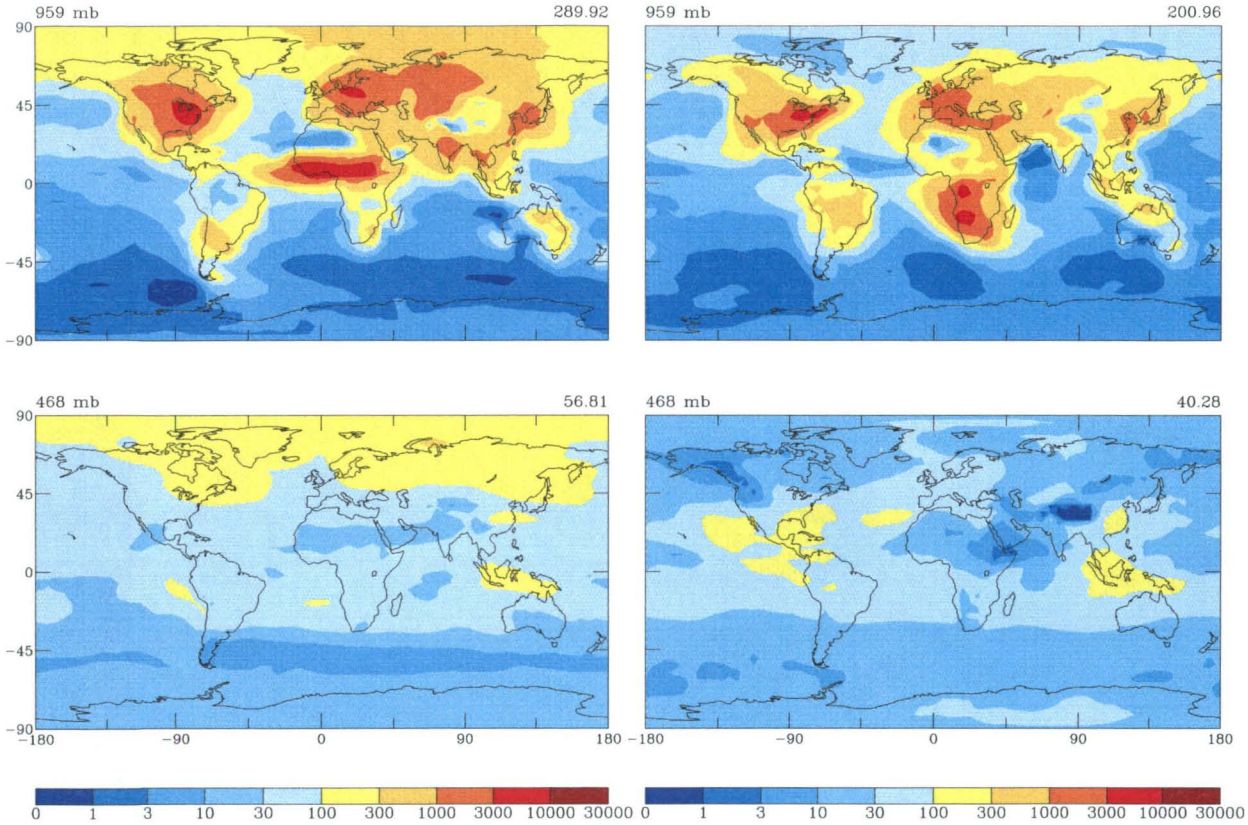

Figure 5.6 Predicted monthly mean gas-phase HNO_3 mixing ratios (pptv) near the surface and at 468 mb in January (left column) and July (right column) for the baseline simulation. Above each panel, the pressure level of the corresponding model layer is indicated, as is the average mixing ratio for that layer.

deposition in winter. Largest predicted HNO_3 mixing ratios occur in the boundary layer of industrialized areas of Europe, North America, central and eastern Asia, and over biomass burning regions in the tropics. In these regions calculated mixing ratios generally exceed 1 ppbv in the boundary layer. HNO_3 mixing ratios at 468 mb are considerably smaller than those near the surface, with a global average mixing ratio in the middle troposphere about 20% of that in the surface layer. Over northern Africa and southern Asia, predicted HNO_3 mixing ratios at 468 mb are less than 30 pptv, considerably lower than those of about 200 pptv predicted by *Wang et al.* [1998]. This difference is a result of predicted uptake of HNO_3 by mineral dust aerosol (see Section 5.4.4).

Figure 5.7 compares predicted gas-phase HNO_3 profiles with aircraft measurements. As compared with *Wang et al.* [1998] and *Mickley et al.* [1999], calculated gas-phase HNO_3 profiles for the baseline case exhibit consistently closer agreement with observed profiles in almost all regions, especially the middle to upper troposphere. Although baseline upper troposphere HNO_3 mixing ratios are somewhat underestimated in locations such as the East China Sea, tropical South Atlantic, and Southern Africa, upper tropospheric HNO_3 is simulated well at all other locations. Previous overestimates of HNO_3 in the remote troposphere are greatly improved, with inclusion of wet deposition of HNO_3 on ice and uptake of HNO_3 by mineral dust aerosol. We will examine further the important processes that affect gas-phase HNO_3 concentrations in Section 5.5.

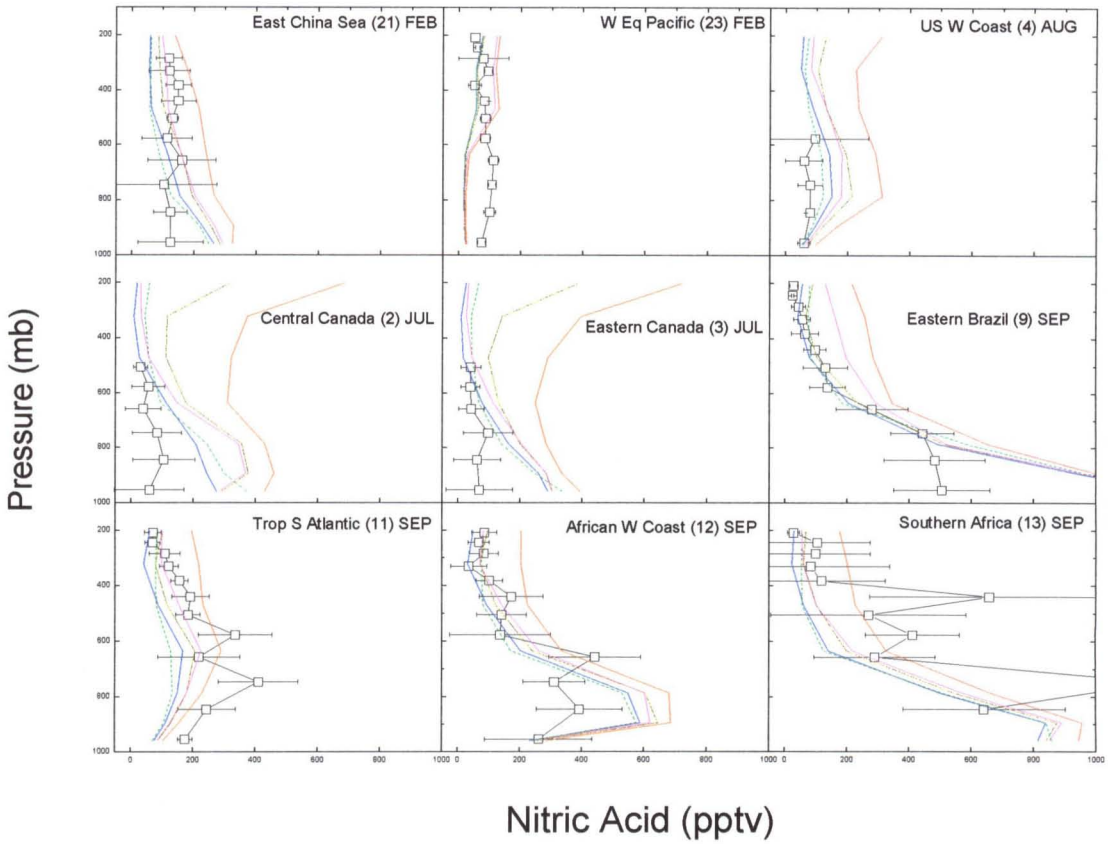

Figure 5.7 Comparison of observed vertical profiles of gas-phase HNO_3 with predicted profiles from different sensitivity studies. The region named in each panel is defined in *Wang et al.* [1998]. Open squares and solid lines are median observations, with standard deviations represented by solid horizontal bars. Model results are monthly mean predictions averaged over the grid cells encompassing each region. Lines include gas-phase HNO_3 predicted in the baseline simulation (blue), gas-phase HNO_3 from a sensitivity run with gas-aerosol partitioning removed from the baseline run (green), sensitivity run with dust uptake of HNO_3 removed (yellow), and sensitivity run with wet deposition of HNO_3 on ice removed (magenta). Gas-phase HNO_3 profiles predicted when all of the gas-aerosol partitioning, dust uptake of HNO_3, and wet deposition of HNO_3 on ice are removed from the baseline run are given by red lines.

5.4.4 Aerosol Nitrate

In the absence of mineral dust aerosol, nitrate aerosol occurs mainly as neutralized ammonium nitrate, in an amount as determined by thermodynamic equilibrium. The presence of sulfate aerosol reduces nitrate formation because ammonia reacts preferentially with sulfate. Predicted annual average baseline mixing ratios of NO_3^-(*nondust*) and NO_3^-(*dust*) are shown in Figure 5.8. Boundary layer NO_3^-(*nondust*) mixing ratios exceed 1 ppbv occur in Europe, eastern China, and the eastern United States. Locations and magnitudes of peak NO_3^-(*nondust*) mixing ratios are consistent with those of Adams99. Compared with the NO_3^-(*nondust*) formation in the northern mid-latitudes, NO_3^-(*nondust*) formation in the biomass burning regions is less as a result of NH_3 limitation [*Adams et al.*, 1999]. NO_3^-(*dust*) mixing ratios exceeding 1 ppbv are predicted near the surface in dust source regions. On a global mean basis, NO_3^-(*dust*) formation is predicted to exceed NO_3^-(*nondust*) formation; near the surface, the predicted global average mixing ratio is 100 pptv for NO_3^-(*dust*) and 75 pptv for NO_3^-(*nondust*), while at 468 mb altitude, it is 41 pptv for NO_3^-(*dust*) and 18 pptv for NO_3^-(*nondust*).

Figure 5.5(b) shows for the surface layer the percent of total nitrate (gas-phase HNO_3+NO_3^-(*nondust*)+NO_3^-(*dust*)) predicted to occur as nitrate aerosol (NO_3^-(*nondust*)+ NO_3^-(*dust*)). On an annual average basis, nitrate formed on mineral dust governs the distribution of high ratios of aerosol nitrate to total nitrate. Near dust source regions, more than 50% of total nitrate is in the aerosol phase, with values approaching 100% over the Sahara Desert, central Asia and Australia, where the formation of nitrate is limited by the availability of gas-phase HNO_3.

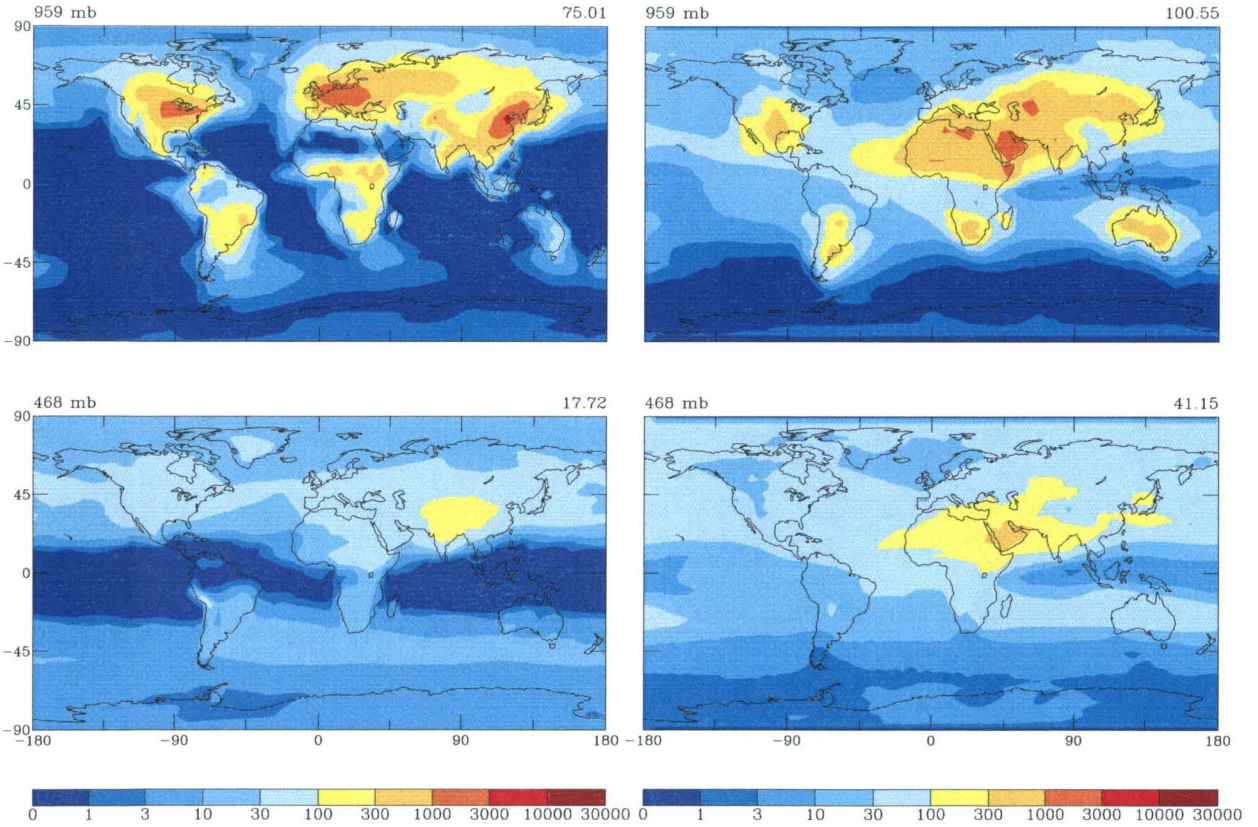

Figure 5.8 Predicted annual average mixing ratios (pptv) of NO_3^- (*nondust*) (left column) and NO_3^- (*dust*) (right column) near the surface and at 468 mb. Above each panel, the pressure level of the corresponding model layer is indicated, as is the average mixing ratio for that layer. Note that 1 μg m^{-3} = 400 pptv NO_3^- at 298 K and 1000 mb.

5.4.5 Ammonia and Ammonium

Predicted annual average mixing ratios of gas-phase ammonia near the surface and at 468 mb are shown by the left column of Figure 5.9. Locations and magnitudes of peak ammonia levels in India, China, Eastern Europe, and Brazil agree well with those of Adams99. Throughout the boundary layer, NH_3 concentrations are determined mainly by emissions and uptake by sulfate aerosol. The largest mixing ratios are predicted to exceed 3 ppbv, with continental mixing ratios generally exceeding 100 pptv. Predicted ammonia mixing ratios generally decrease rapidly with altitude, with the global mean mixing ratio at 468 mb about 12% of the surface value. As a result of the strong emissions of NH_3 in India, NH_3 mixing ratios in this region still exceed 1 ppbv at 468 mb.

Predicted annual average mixing ratios of particulate ammonium are shown by the right column of Figure 5.9. Highest ammonium mixing ratios, over 3 ppbv, are found in industrialized areas, such as the eastern United States, Europe, and China. Mixing ratios generally exceed 300 pptv over the continents. These results are also in good agreement with those of Adams99.

5.4.6 Ozone

Predicted monthly mean ozone mixing ratios (ppbv) near the surface and at 468 mb in January and July are shown in Figure 5.10 for the baseline simulation. Boundary layer ozone concentrations over industrial regions in the Northern Hemisphere and over biomass burning regions in the tropics are in the range of 40–70 ppbv, levels that are consistent

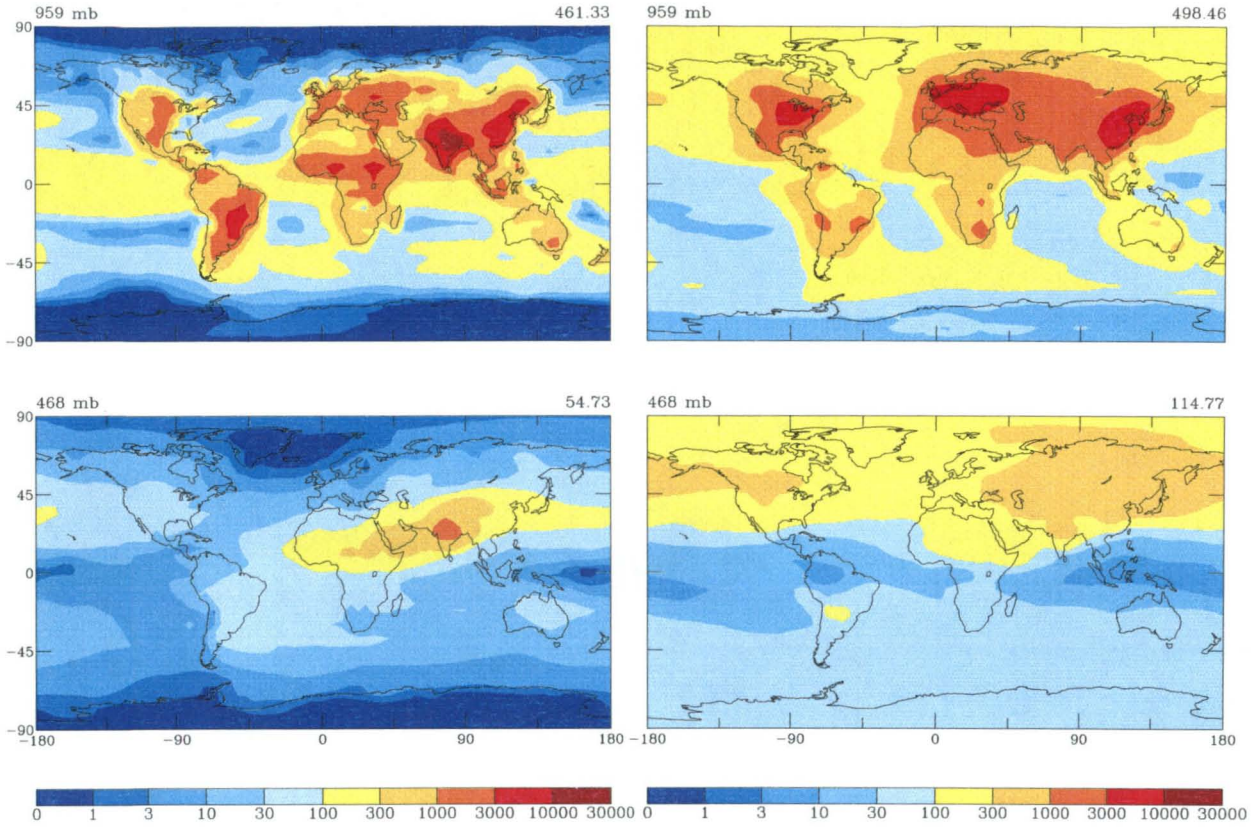

Figure 5.9 Predicted annual average mixing ratios (pptv) of gas-phase NH_3 (left column) and aerosol phase NH_4^+ (right column) near the surface and at 468 mb for baseline simulation. Note that 1 μg m^{-3} NH_3 = 1457 pptv NH_3 and 1 μg m^{-3} NH_4^+ = 1377 pptv NH_4^+ at 298 K and 1000 mb. Above each panel, the pressure level of the corresponding model layer is indicated, as is the average mixing ratio in that layer.

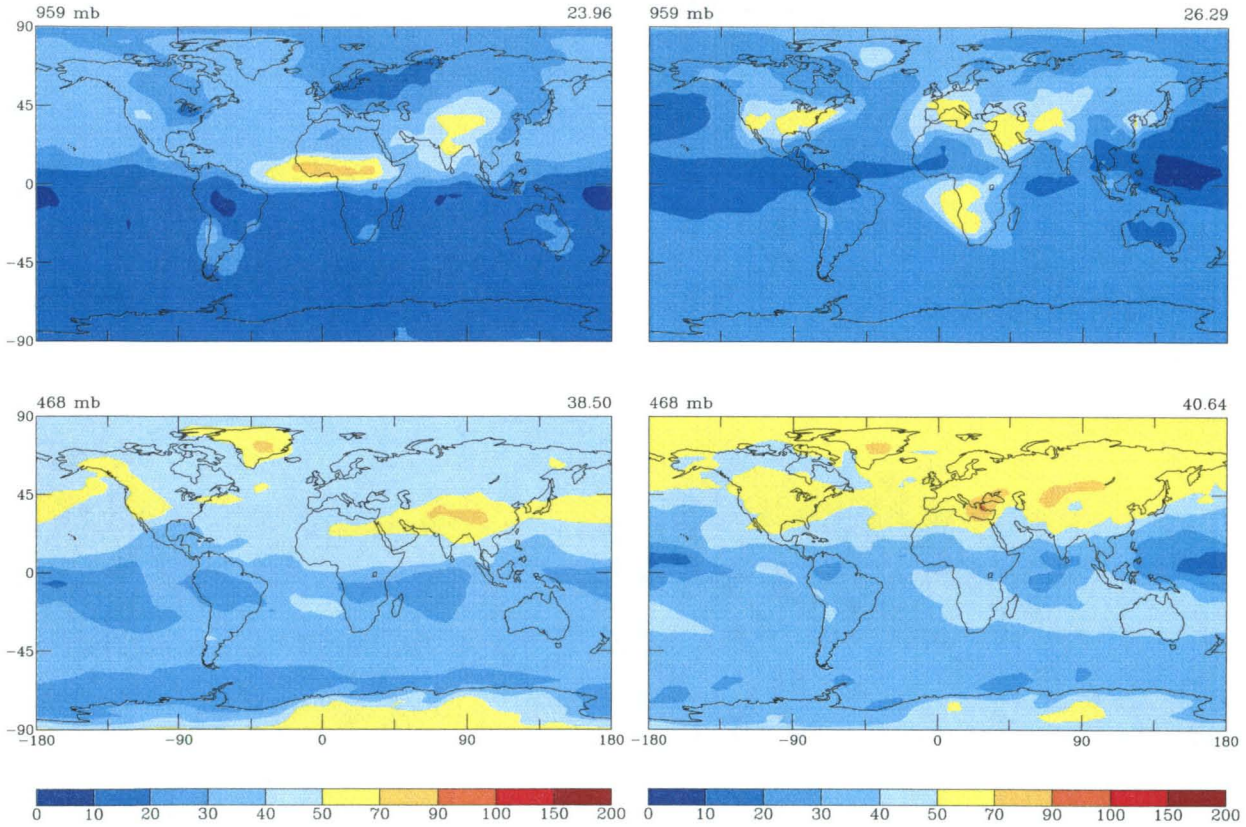

Figure 5.10 Predicted monthly mean ozone mixing ratios (ppbv) near the surface and at 468 mb in January (left column) and July (right column). Above each panel, the pressure level of the corresponding model layer is indicated, as is the average mixing ratio in that layer.

with those predicted by *Mickley et al.* [1999]. Predicted O_3 mixing ratios at 468 mb generally exceed those near the surface, as a result of emissions of NO_X from lightning and biomass burning, deep convection from the continental boundary layer, transport from the stratosphere, as well as less dry deposition.

A global budget of odd oxygen (O_X) is presented in Table 5.7. For the purpose of this budget, $O_X$is defined as the sume of O_3, O, NO_2, $2\times NO_3$, HNO_4, $3\times NO_2O_5$, and the peroxyacylnitrates; ozone makes up over 99% of O_X globally. Calculated O_3 in situ chemical production and loss rates, 3761 Tg yr^{-1} and 3412 Tg yr^{-1}, respectively, are lower than the production rate of 4330 Tg yr^{-1} the loss rate of 3960 Tg yr^{-1} obtained by *Mickley et al.* [1999] for the present-day atmosphere. The difference arises because the unified model considers additional NO_Xremoval by nitrate, ammonium, OC, and mineral dust aerosols as well as aerosol water. Mineral dust is predicted to take up 50 Tg O_3 per year.

Table 5.7 Global Budget for Tropospheric Ozone

Sources (Tg O_3 yr^{-1})	
In situ chemical production	3761
Transport from stratosphere	401
Total sources	4162
Sinks (Tg O_3 yr^{-1})	
In situ chemical loss	3412
Dust uptake	50
Dry deposition	700
Total sinks	4162
Burden (Tg O_3)	318
Residence time (days)	28

Budgets are for the odd oxygen family defined as the sum of O_3,O,NO_2,$2\times NO_3$, HNO_4, $3\times NO_2O_5$, and the peroxyacylnitrates.

5.5 Important Processes that Affect Gas-Phase HNO_3 Concentrations

Observed gas-phase HNO_3 concentrations in the remote troposphere are generally lower than those predicted by tropospheric chemical transport models [*Hauglustaine et al.*, 1998; *Wang et al.*, 1998; *Lawrence and Crutzen*, 1998]. Phenomena that have not generally been included in global CTM simulations but have the potential to lead to lower predicted gas-phase HNO_3 levels include equilibrium gas-aerosol partitioning of HNO_3, uptake of HNO_3 by mineral dust aerosol, and scavenging of gas-phase HNO_3 by ice cloud particles (which can precipitate or evaporate before reaching the surface). To examine the relative importance of each of these three processes, we perform three sensitivity runs with each of the processes removed from the baseline simulation.

Figure 5.11(a) shows the annual, zonal average mixing ratios (pptv) of gas-phase HNO_3 for the baseline simulation, while the other panels of Figure 5.11 present the ratio of the annual, zonal mean gas-phase HNO_3 mixing ratios obtained in each sensitivity run to the baseline values. Without equilibrium gas-aerosol partitioning (Figure 5.11(b)), predicted gas-phase HNO_3 mixing ratios are up to 30% larger near the surface and up to 60% larger in the upper troposphere. (Note the absolute concentrations of HNO_3 are small in the upper troposphere.) This is expected because particulate ammonium nitrate formation occurs mainly over polluted areas near the surface, and in the upper troposphere where SO_4^{2-}(*nondust*) concentrations are low and free NH_3 over strong NH_3 emissions is available for ammonium nitrate formation. What is not expected in the absence of gas-aerosol partitioning is a 10–20% decrease in predicted gas-phase HNO_3 in the

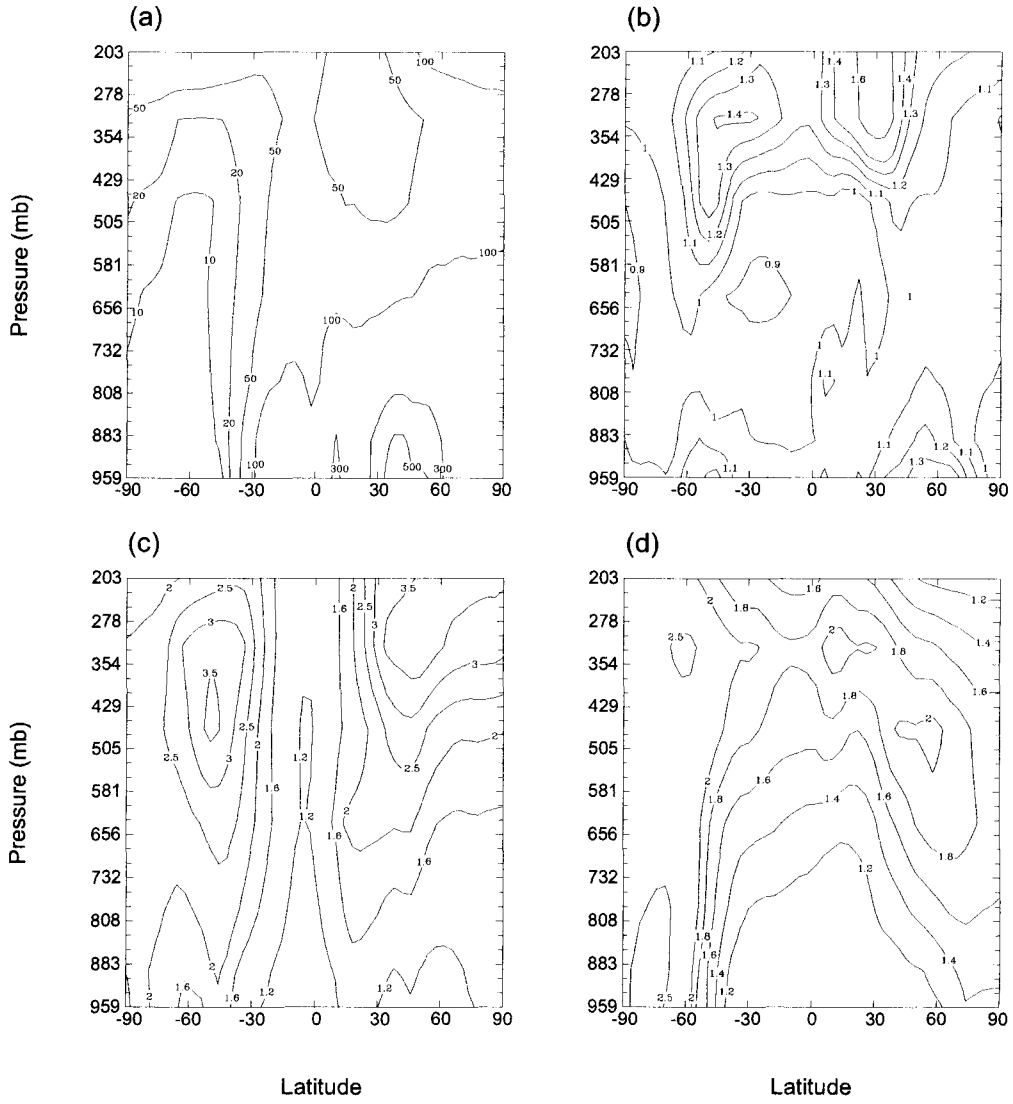

Figure 5.11 (a) Predicted annual, zonal average HNO_3 mixing ratios (pptv) for the baseline run; the remaining plots show the ratio of the annual, zonal mean mixing ratios of gas-phase HNO_3 (relative to the baseline simulation) considering: (b) gas-aerosol partitioning removed from the baseline simulation; (c) dust uptake of HNO_3 removed from the baseline simulation; and (d) wet deposition of HNO_3 on ice removed from the baseline simulation.

middle troposphere over the subtropics of the Southern Hemisphere. When gas-aerosol partitioning is ignored, gas-phase HNO_3 does not survive long distance transport because of dry deposition of gas-phase HNO_3. However, aerosol nitrate is transported longer distances than HNO_3 since nitrate particles have lower dry deposition velocity, and these particles may release gas-phase HNO_3 when conditions, such as temperature and relative humidity, change. As a consequence, the simulation without gas-aerosol partitioning predicts less gas-phase HNO_3 over the oceans and in the remote troposphere, leading to the reduction shown in Figure 5.11(b). The zonal mean reduction occurs only in the middle troposphere of the SH. In other latitudes and altitudes, the decrease from transport is too small to offset the increase in gas-phase HNO_3 in polluted areas and in the upper troposphere.

Without uptake of HNO_3 by mineral dust (Figure 5.11(c)), predicted gas-phase HNO_3 mixing ratios increase everywhere in the atmosphere compared with baseline values. While absolute increases in HNO_3 are about 100–150 pptv in the Northern Hemisphere (not shown), which are vertically fairly homogeneous, the highest percentage increase, about 300%, occurs near 300 mb in the middle to high latitudes of the Northern Hemisphere, and near 400 mb in the middle latitudes of the Southern Hemisphere. Significant dust uptake of HNO_3 generally occurs in areas with high HNO_3 and dust concentrations, but uptake of HNO_3 in the lower troposphere is affected by simultaneous uptake of SO_2, which is also important in determining dust alkalinity. With low SO_2 concentrations in the upper troposphere, uptake of HNO_3 can occur as long as the dust particles are alkaline, and HNO_3 is not limiting.

Deposition of HNO_3 on ice also plays an important role in governing HNO_3

concentrations. Without deposition of HNO_3 on ice (Figure 5.11(d)), HNO_3 concentrations in the middle to upper troposphere increase significantly from baseline values.

Dust uptake of HNO_3 and scavenging of HNO_3 by ice are the most important factors that lower predicted gas-phase HNO_3 concentrations from those determined solely on the basis of gas-phase chemistry. Equilibrium gas-aerosol partitioning affects mainly HNO_3 concentrations in the polluted boundary layer and in the upper troposphere. These conclusions are also supported by Figure 5.7, which compares baseline HNO_3 levels to those from different sensitivity runs for different regions. Over US West Coast, central and eastern Canada, dust uptake is found to have dominant effect on gas-phase HNO_3 mixing ratios, since over these regions the HNO_3 mixing ratios increase significantly when dust uptake is removed from the baseline simulation. Over eastern Brazil and equatorial west Pacific, deposition on ice has dominant effect. Figure 5.7 also shows gas-phase HNO_3 profiles for a simulation with all of the dust uptake, equilibrium gas-aerosol partitioning, and wet deposition on ice removed from the baseline simulation. Differences between HNO_3 profiles demonstrate the importance of including all three processes discussed in simulations of gas-phase HNO_3.

5.6 Effect of Aerosols on Gas-Phase Chemistry Through Photolysis Rates

Figure 5.12 shows the annual mean baseline aerosol optical depth at 600 nm, based on SO_4^{2-}(*nondust*)/NO_3^-(*nondust*)/NH_4^+/H_2O, OC, BC, and mineral dust. Highest optical depths of 0.4–0.5 are predicted over Europe and eastern Asia. Optical depths of 0.2–0.5

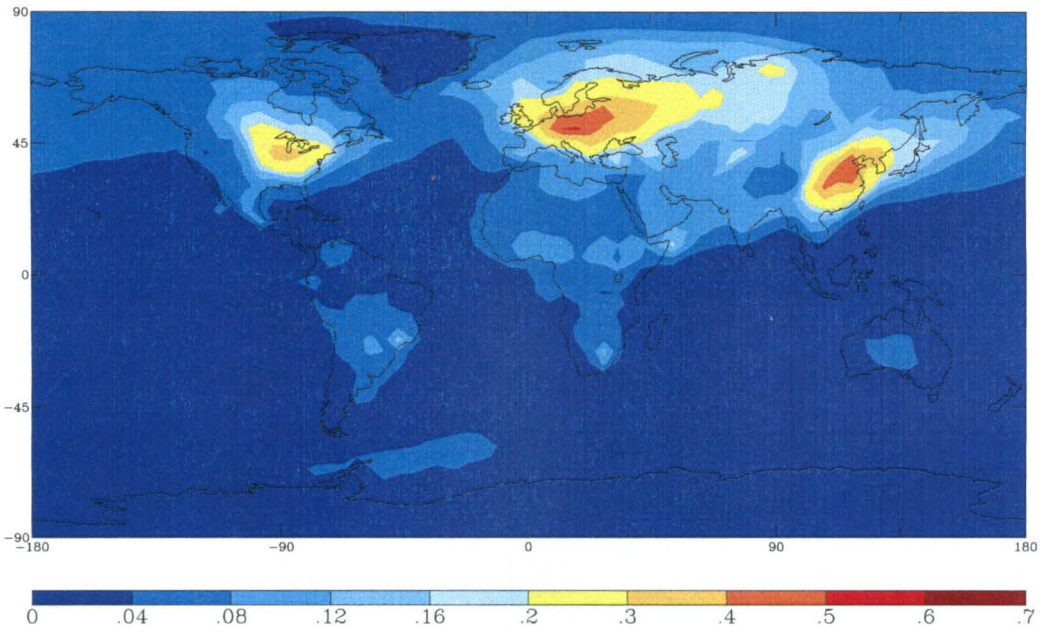

Figure 5.12 Predicted annual mean aerosol optical depth at 600 nm. Aerosols considered are SO_4^{2-}(*nondust*)/NO_3^-(*nondust*)/NH_4^+/H_2O, OC, BC, and mineral dust.

over Europe, eastern China, and eastern United states are consistent with those observed in these areas [*Ghan et al.*, 2001].

To examine the effect of aerosols on gas-phase chemistry by altering photolysis rates, we perform a sensitivity run with all aerosols removed from the Fast-J scheme. Although urban scattering aerosols can alter photolysis rates by about 10–20% at small solar zenith angles [*Liao et al.*, 1999], the global effect of aerosols on HNO_3 and O_3 through altered photolysis rates is found to be small. At the surface layer, including aerosols in photolysis rate calculations leads to a maximum reduction of about 25 pptv in HNO_3 mixing ratios over central Africa, India, central and northeast Asia; this amount is to be compared with HNO_3 mixing ratios exceeding 1 ppbv in those regions. The largest reduction of about 1 ppbv in O_3 mixing ratios is found in regions with maximum HNO_3

reduction, but, as with HNO_3, the reduction is negligible compared with O_3 mixing ratios of 30–50 ppbv. Changes in HNO_3 and O_3 concentrations at 468 mb are even smaller than those at the surface. The small effects of aerosols found here agree with results of *Fiore et al.* ["Background ozone over the United States in summer: origin and contribution to pollution episodes," submitted to *Journal of Geophysical Research*, 2001], which show that inclusion of aerosols in photolysis rate calculations changes monthly mean O_3 by less than 0.2 ppbv anywhere.

5.7 Effect of Aerosols on Gas-Phase Chemistry and Aerosol Formation by Heterogeneous Reactions

5.7.1 Aerosol Surface Area

Heterogeneous reactions occur on the surfaces of SO_4^{2-}(*nondust*)/NO_3^-(*nondust*)/NH_4^+/H_2O, OC, and mineral dust aerosols. In order to evaluate the role of each class of aerosol in heterogeneous chemistry, we calculate first the annual mean aerosol surface area concentrations (10^{-9} cm^2 cm^{-3}) for (a) SO_4^{2-}(*nondust*)/NO_3^-(*nondust*)/NH_4^+/H_2O, (b) OC, and (c) mineral dust (Figure 5.13). Surface area concentrations of SO_4^{2-}(*nondust*)/NO_3^-(*nondust*)/NH_4^+/H_2O aerosol are much higher than those of OC and mineral dust; on a global mean basis, the surface areas of SO_4^{2-}(*nondust*)/NO_3^-(*nondust*)/NH_4^+/H_2O, OC, and mineral dust account for about 83%, 14%, and 3% of total aerosol surface area near the surface. Thus, heterogeneous reactions of N_2O_5, NO_3, NO_2, and HO_2, which occur on wet surfaces of aerosols, are largely determined by the SO_4^{2-}(*nondust*)/NO_3^-(*nondust*)/NH_4^+/H_2O surface

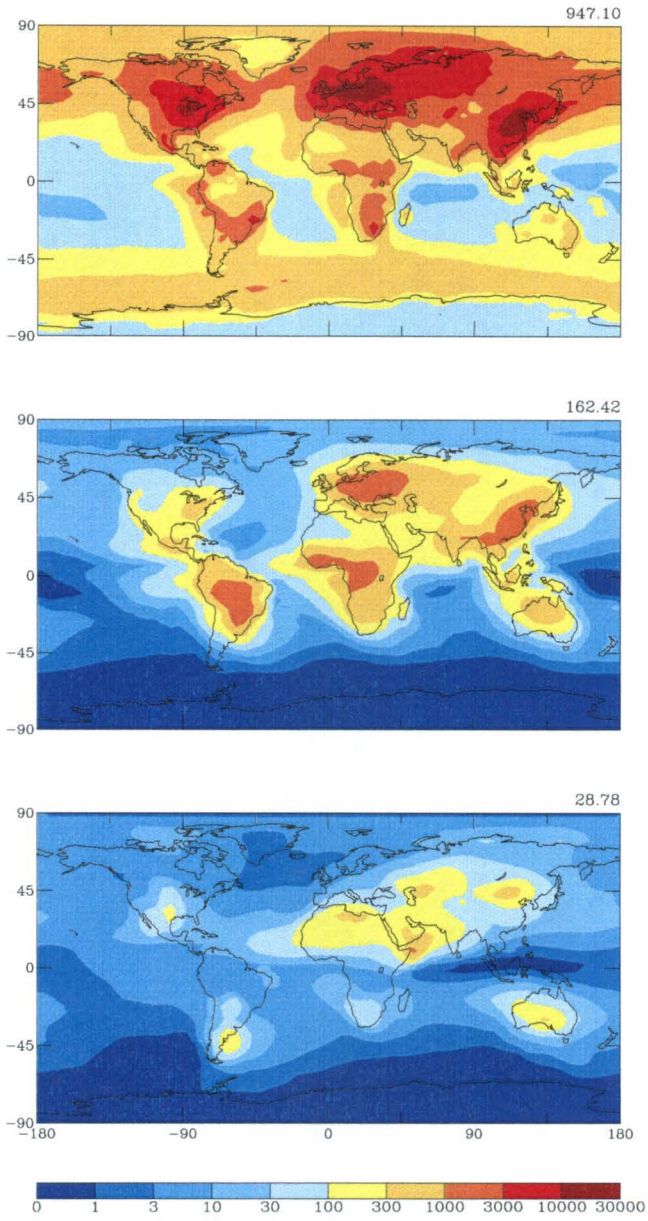

Figure 5.13 Annual mean aerosol surface area concentrations (10^{-9} cm^2 cm^{-3}) in the GCM surface layer for: SO_4^{2-}(*nondust*)/NO_3^-(*nondust*)/NH_4^+/H_2O (top panel); OC (middle panel); and mineral dust (bottom panel). Above each panel, the average value in that layer is indicated.

area. Although the predicted surface area of mineral dust aerosol is only a small fraction of total global aerosol surface area, mineral dust plays an important role in gas-phase chemistry through uptake of O_3, SO_2 and HNO_3.

5.7.2 Effects on Concentrations of Gas-Phase Species and Aerosols

To determine the effects of heterogeneous reactions on gas-phase and aerosol chemistry, a sensitivity simulation is performed with all heterogeneous reactions (except in-cloud SO_2 oxidation) removed from the baseline simulation. Annual average NO_X, O_3, SO_4^{2-}(*nondust*), NO_3^-(*nondust*), and NH_4^+ concentrations in the absence of heterogeneous reactions can be compared with the baseline values. Figure 5.14 shows, for each species, the ratio of annual mean baseline mixing ratios (in the presence of aerosols) to those in the absence of heterogeneous reactions in the surface layer.

5.7.2.1 Gas-Phase Species

The presence of aerosols leads to reduction in NO_X concentrations in the middle to high latitudes in both Northern and Southern Hemispheres (Figure 5.14(a)), with the maximum reduction of about 80% occurring at high latitudes of the NH. With high aerosol concentrations and low OH abundance at high latitudes of the NH, NO_X loss depends mainly on heterogeneous reactions. Since predicted aerosol concentrations in the SH are much smaller than those in the NH, the reduction of NO_X by heterogeneous reactions is found to be only about 10–30% in the middle to high latitudes of the SH. NO_X concentrations are not sensitive to heterogeneous reactions in the tropics, where the

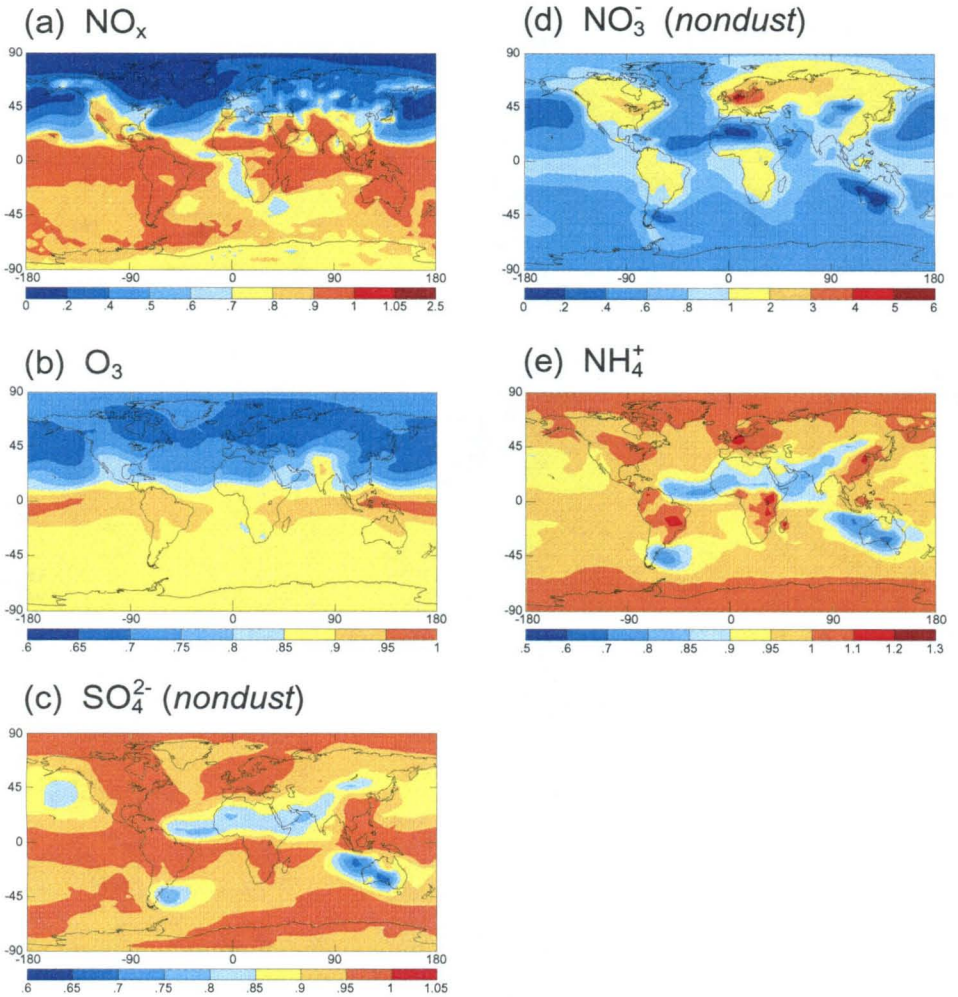

Figure 5.14 Ratio of annual mean mixing ratios calculated in the baseline run to those obtained in the absence of all heterogeneous reactions. For (a) NO_X, (b) O_3, (c) SO_4^{2-} (*nondust*), (d) NO_3^- (*nondust*), and (e) NH_4^+ in the GCM surface layer.

daytime reaction of NO_2 with OH is the most important NO_X removal mechanism. These effects of heterogeneous reactions on NO_X are similar to those found by *Dentener and Crutzen* [1993] in the SH and tropics. In the high latitudes of the NH, the simulation of *Dentener and Crutzen* [1993], which considered heterogeneous reactions of NO_3 and N_2O_5 on non-dust sulfate particles, predicted NO_X reductions of 80% from October to April and of 10–20% in summer. Present work predicts annual mean NO_X reductions of about 80% in the high latitudes of the NH, reflecting the effects of NO_3^-(*nondust*), ammonium, OC, and mineral dust aerosols.

As a result of NO_X removal by aerosols and dust uptake of O_3, predicted baseline ozone concentrations are lower than those in the absence of heterogeneous reactions (Figure 5.14(b)). Ozone concentrations at NH high latitudes are predicted to be reduced by about 30% near the surface. Reactions on aerosols generally reduce O_3 concentrations by 10 to 15% in the SH. Of the two factors that cause O_3 reduction, dust uptake of O_3 and NO_X removal by SO_4^{2-}(*nondust*)/NO_3^-(*nondust*)/NH_4^+/H_2O, OC, and mineral dust, the latter is slightly more influential; the predicted global annual average O_3 burden would increase by 7% in the absence of dust uptake and by 16% in the absence of both dust uptake and NO_X removal.

Since the unified model considers O_3 reduction from both dust uptake of O_3 and NO_X removal on SO_4^{2-}(*nondust*)/NO_3^-(*nondust*)/NH_4^+/H_2O, OC, and mineral dust aerosols, ozone reductions obtained here cannot be compared directly with those predicted by *Dentener and Crutzen* [1993] or *Dentener et al.* [1996]. *Dentener and Crutzen* [1993] considered only O_3 reduction from heterogeneous reactions of NO_3 and N_2O_5 on non-

dust sulfate particles, while *Dentener et al.* [1996] considered only O_3 reduction from dust uptake. However, in the high latitudes of the NH and SH, where dust concentrations are not high, O_3 reductions predicted in this work are in close agreement with those of *Dentener and Crutzen* [1993]. We obtain about 5–10% higher O_3 reductions in the high latitudes of the NH as a result of higher predicted NO_X removal there. Over Saudi Arabia/Horn of Africa, where the dust mass is the largest (Figure 5.2), O_3 reduction predicted in this work is about 15–20%, which is higher than the reduction of about 8% in same area obtained by *Dentener et al.* [1996]. This difference may result from the higher NO_X reduction predicted in the unified model and the different dust concentrations in different models.

5.7.2.2 Aerosols

Heterogeneous reactions affect not only concentrations of gas-phase species but also those of aerosols. SO_4^{2-}(*nondust*) concentrations are reduced by dust uptake (Figure 5.14(c)). Near the surface, reductions of SO_4^{2-}(*nondust*) exceeding 20% occur near dust sources such as the Sahara Desert, central and eastern Asia, Australia, and southern South Africa.

Changes in NO_3^-(*nondust*) mixing ratios near the surface (Figure 5.14(d)) reflect the changes in gas-phase HNO_3 mixing ratios. The baseline run predicts higher concentrations over almost all continental areas except those near the dust sources.

The changes in NH_4^+ (Figure 5.14(e)) depend on the changes in SO_4^{2-}(*nondust*) and NO_3^-(*nondust*). In the surface layer, NH_4^+ mixing ratios are reduced by dust uptake of SO_2 and HNO_3 near the dust source regions such as the Sahara Desert, the Arabian Peninsula,

central Asia, southern South America, and Australia. Heterogeneous reactions increase surface NH_4^+ mixing ratios in the industrialized areas in Europe, South America, Africa, and eastern Asia, corresponding to the increase of SO_4^{2-}(*nondust*) and NO_3^-(*nondust*) there. In these regions, NH_4^+ concentrations are increased by 10–20%.

5.7.3 Effects on Global and Annual Average Burdens

To see the overall effects of heterogeneous reactions, we list in Table 5.8 global and annual average burdens for the baseline run (with all the heterogeneous reactions) and in the absence of heterogeneous reactions. Without heterogeneous reactions (dust uptake of SO_2), the burdens of SO_2 and SO_4^{2-}(*nondust*) are about 10% higher than those simulated with dust uptake, which has important implications for radiative forcing of sulfate. Compared with the baseline run, the predicted HNO_3 burden is 40% higher, and the O_3 burden increases by 16% in the absence of heterogeneous reactions. When compared with the baseline run, a higher NH_4^+ burden but lower NH_3 and NO_3^-(*nondust*) burdens in the absence of heterogeneous reactions indicate that the changes in the concentrations of these species are mainly affected by additional SO_4^{2-}(*nondust*) formation.

Since direct radiative forcing depends roughly linearly on burdens, we can give an approximate estimate of the effect of heterogeneous reactions on radiative forcing of O_3 or non-dust sulfate aerosol. *Mickley et al.* [1999] estimated that the global mean radiative forcing of O_3 is 0.44 W m^{-2} for a predicted global O_3 burden of 360 Tg. Since the baseline simulation in this work predicts a global ozone burden of 318 Tg, the radiative forcing by ozone is roughly $0.44 \times 318/360 = 0.38$ W m^{-2}. Thus in the absence

of heterogeneous reactions, a 16% increase in O_3 burden can approximately lead to an increase in global mean ozone radiative forcing by 0.38 W $m^{-2} \times 0.16 \approx 0.06$ W m^{-2}. Similarly, since Adams99 predicted a non-dust sulfate burden of 2.09 Tg, and *Adams et al.* [2001] calculated a corresponding global mean forcing of -0.95 W m^{-2}, the 13% increase in SO_4^{2-}(*nondust*) burden in the absence of heterogeneous reactions roughly increases SO_4^{2-}(*nondust*) forcing by $-0.95 \times 1.64 \times 0.13/2.09 \approx -0.1$ W m^{-2}, where 1.64 Tg is the SO_4^{2-}(*nondust*) burden from the baseline simulation.

It should be noted that sulfate and nitrate aerosols associated with dust effectively will not change the radiative properties of dust particles. On each dust particle, masses of sulfate and nitrate account for only small fractions of dust mass.

5.7.4 Summary for Heterogeneous Reactions

The presence of heterogeneous reactions generally reduces O_3 and SO_4^{2-}(*nondust*) concentrations, but they may locally increase or reduce NO_3^-(*nondust*) and NH_4^+ concentrations depending on whether dust is present. Dust uptake of SO_2 and HNO_3 leads to reduced concentrations of SO_4^{2-}(*nondust*), NO_3^-(*nondust*), and NH_4^+ near dust source regions, which can reduce radiative cooling by SO_4^{2-}(*nondust*), NO_3^-(*nondust*), and NH_4^+. Some climate models have considered the effect of heterogeneous reactions on O_3 concentrations, but the effects of heterogeneous reactions on aerosol concentrations are generally not included in estimates of aerosol radiative forcing. This issue requires more detailed study.

Table 5.8 Global and Annual Average Burdens (Tg) for the Baseline Case and Sensitivity Cases

Species	Baseline case	NO_X emissions (+50%)	NH_3 emissions (+50%)	Sulfur emissions (+50%)	No heterogenous reactions
SO_2	0.52	0.52 (0%)	0.50 (-4%)	0.89 (+71%)	0.56 (+8%)
SO_4^{2-}(*nondust*)	1.64	1.70 (+4%)	1.66 (+1%)	2.38 (+45%)	1.85 (+13%)
HNO_3	1.44	1.97 (+37%)	1.37 (-5%)	1.48 (+3%)	2.02 (+40%)
O_3	318	360 (+13%)	314 (-1%)	319 (0%)	369 (+16%)
H_2O_2	3.70	3.66 (-1%)	3.73 (+1%)	3.66 (-1%)	3.88 (-9%)
NH_3	0.20	0.17 (-15%)	0.39 (+95%)	0.14 (-30%)	0.16 (-20%)
NH_4^+	0.42	0.44 (+5%)	0.54 (+29%)	0.48 (+14%)	0.45 (+7%)
NO_3^-(*nondust*)	0.17	0.19 (+12%)	0.32 (+88%)	0.10 (-41%)	0.15 (-12%)
SO_4^{2-}(*dust*)	0.19	0.15 (-21%)	0.20 (+5%)	0.29 (+53%)	
NO_3^-(*dust*)	0.50	0.61 (+22%)	0.47 (-6%)	0.48 (-4%)	

Numbers in parentheses are percentage changes compared with the baseline case.

5.8 Sensitivity of Gas-Phase Chemistry and Aerosols to NO_X, NH_3, and Sulfur Emissions

In a set of three sensitivity runs, total global emissions of each of NO_X, NH_3, and sulfur are increased by 50%. Table 5.8 shows the predicted baseline annual average global burden of the various gas-phase and aerosol species together with the burdens from the three sensitivity simulations. Burdens of gas-phase and aerosol phase species generally change nonlinearly with changes in emissions.

5.8.1 Sensitivity to NO_X Emissions

Compared with the baseline run, a 50% increase in NO_X emissions increases O_3, HNO_3, NO_3^-(*nondust*), and NO_3^-(*dust*) burdens by 13%, 37%, 12%, and 22%,

respectively. As expected, more NH_4NO_3 formation occurs when more HNO_3 is available, resulting in a 12% increase in the $NO_3^-(nondust)$ burden, a 5% increase in the NH_4^+ burden, and a 15% reduction in the NH_3 burden. More available gas-phase HNO_3 also leads to 22% more nitrate formation on dust particles. Dust particles with $[Ca^{2+}]>[SO_4^{2-}(dust)]+0.5[NO_3^-(dust)]$ can take up more HNO_3 when more HNO_3 is available, but, as a result, they take up less SO_2 once $[Ca^{2+}]>[SO_4^{2-}(dust)]+0.5[NO_3^-(dust)]$ is satisfied; $SO_4^{2-}(dust)$ burden is reduced by 21% in this sensitivity run.

An increase in NO_X emissions may influence in-cloud sulfate formation by aqueous oxidation of SO_2 by O_3 in several ways. The increase (or reduction) in O_3 concentrations can increase (or reduce) $SO_4^{2-}(nondust)$, and the changed $NO_3^-(nondust)$ and NH_4^+ can affect cloud pH. In this sensitivity run, reduction in SO_2 or the increase in $SO_4^{2-}(nondust)$ occurs in areas with increased ozone, indicating that the changes in O_3 concentrations are more dominant in in-cloud sulfate formation than the changes in cloud pH. Near dust sources, since increased NO_X emissions lead to less $SO_4^{2-}(dust)$ formation, more SO_2 is available for $SO_4^{2-}(nondust)$ formation, and $SO_4^{2-}(nondust)$ is predicted to increase by 30–100 pptv in these areas.

5.8.2 Sensitivity to NH_3 Emissions

Compared with the baseline simulation, a 50% increase in NH_3 emissions increases the predicted burdens of NH_3, NH_4^+, and $NO_3^-(nondust)$ by 95%, 29%, and 88%, respectively. With added NH_3 in the atmosphere, ammonium nitrate formation is limited by HNO_3; thus a 50% increase in NH_3 emissions is predicted to result in an increase in

NH_4^+ burden by only 29%, leading to a significant increase in the burden of NH_3.

Increasing NH_3 emission can also affect in-cloud sulfate formation through its effect on cloud pH. The burden of SO_2 is reduced by 4%. Some fraction of SO_2 reduction is caused by more conversion of SO_2 to SO_4^{2-}(*nondust*) in cloud droplets resulted from increased NH_4^+. And, because more HNO_3 exists as NH_4NO_3 when NH_3 emissions are increased, less gas-phase HNO_3 is available for dust uptake, and more SO_2 can be taken up by dust particles. The latter process also explains the 5% increase in SO_4^{2-}(*dust*) burden and the 6% reduction in NO_3^-(*dust*) burden.

5.8.3 Sensitivity to Sulfur Emissions

With a 50% increase in sulfur emissions, burdens of SO_2 and SO_4^{2-}(*nondust*) are 71% and 45% higher than those in the baseline case, respectively. Higher sulfate burdens also lead to more ammonium sulfate formation; hence, the burden of NH_4^+ increases by 14%, whereas that of NH_3 decreases by 30%. As a consequence of increased ammonium sulfate, the formation of NH_4NO_3 is reduced, and the burden of NO_3^-(*nondust*) decreases by 41% as compared with the baseline simulation. Increasing sulfur emissions also affects the formation of sulfate and nitrate on dust particles. With more SO_2, dust particles are expected to take up less HNO_3 because of competition for alkalinity. Compared with the baseline run, the burden of SO_4^{2-}(*dust*) increases by 53%, while that of NO_3^-(*dust*) decreases by only 4%. The small amount of NO_3^-(*dust*) reduction can be explained as follows. As shown in Table 5.8, less ammonium nitrate formation leaves 3% more HNO_3 in the gas-phase available for dust uptake. And, in dust source regions, where relative

humidity tends to be low, because of the assumed reaction probability dependence on RH, dust particles will take up HNO_3 preferentially. When these particles are transported to regions with RH exceeding 50%, some of the dust particles neutralized by nitrate are not available to uptake SO_2. Under such situations, the availability of more SO_2 affects the $NO_3^-(dust)$ burden only marginally.

5.9 Sensitivity of Sulfate Concentrations to Assumptions Used for Calculating pH of Cloud Droplets

In-cloud oxidation of SO_2 by O_3 is very sensitive to cloud pH. Simulation of cloud pH has inherent uncertainties as a result of their multiphase nature, inherent instability, and variability in chemical compositions. Since it is difficult to alter the cloud properties in the climate model without altering other thermodynamic variables that could also affect the sulfur chemistry, we focus on the sensitivity of $SO_4^{2-}(nondust)$ concentrations to assumed NH_4^+ and $NO_3^-(nondust)$ concentrations as used in previous global simulations.

Figure 5.15 shows the December-January-February (DJF) and June-July-August (JJA) averaged cloud pH at 787 mb. We chose this model layer because clouds occur the most frequently around 2 km altitude [*Liou*, 1992]. It should be noted that cloud fraction at each grid cell is usually smaller than 1.0, but cloud pH can only be shown for the whole cell. In the industrialized areas in the Northern Hemisphere, where in-cloud oxidation of SO_2 by O_3 is the most important, predicted cloud pH generally ranges from 2.5 to 3.5 in winter and 3.0 to 4.0 in summer. Higher cloud pH in summer can be explained by the stronger NH_3 emissions in summer than in winter. These predicted pH values compare

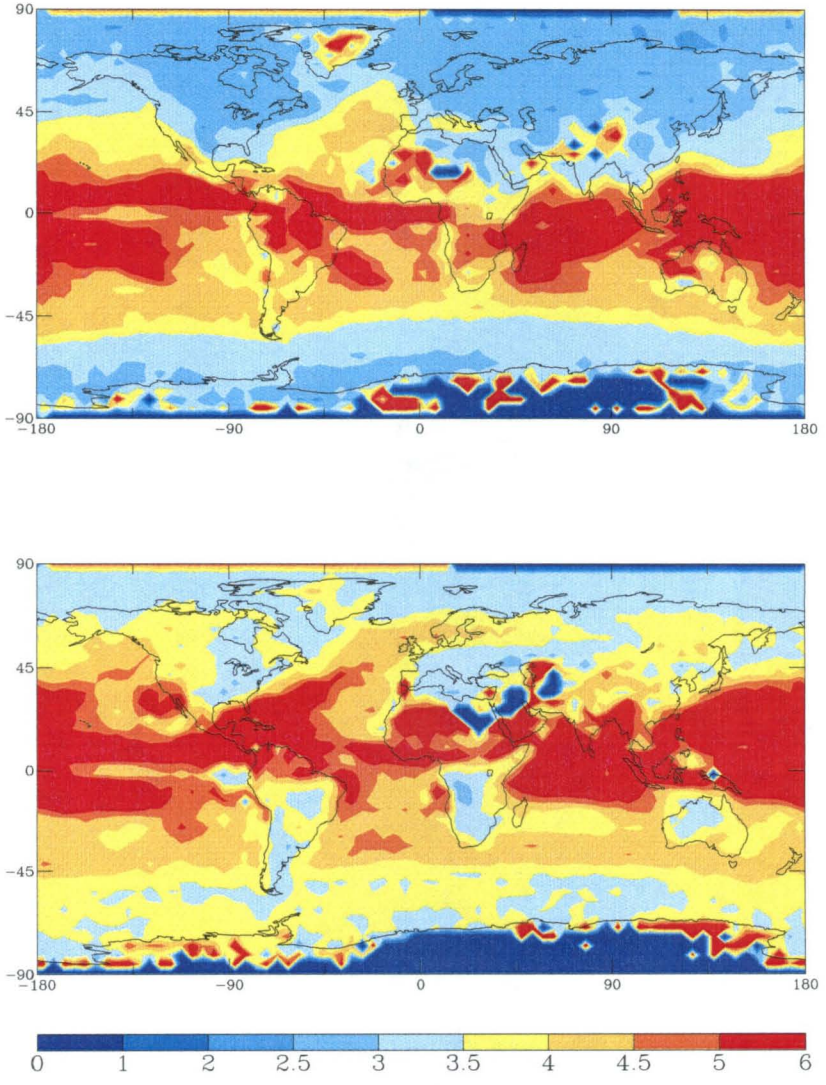

Figure 5.15 December-January-February (DJF) and June-July-August (JJA) averaged cloud pH at 787 mb (about 2 km altitude). pH values smaller than 1.0 indicate that no cloud is present during the 3-month period.

well with the measurements of *Kim et al.* [1992] and *Oberholzer et al.* [1992]. *Kim et al.* [1992] reported that from May to October, observed cloud water pH in the eastern United States was in the range of 2.4 to 4.9. *Oberholzer et al.* [1992] found that winter cloud pH in polluted central Switzerland ranged from 3.14 to 3.35.

Previous global calculations of cloud pH [*Roelofs et al.*, 1998; *Barth et al.*, 2000] generally assumed the molar ratio of NH_4^+ to SO_4^{2-}(*nondust*) in cloud drops to be 1.0 and did not take into account the effect of NO_3^-(*nondust*) on pH. To test the sensitivity of sulfate concentrations to those assumptions, a simulation is performed by setting in-cloud molar concentration of NH_4^+ be the same as that of SO_4^{2-}(*nondust*), and by setting the in-cloud NO_3^-(*nondust*) concentration to zero. The ratio of DJF averaged SO_4^{2-}(*nondust*) column burdens of this simulation to those obtained in the baseline simulation (with prognostic in-cloud ammonium and nitrate) is shown in Figure 5.16(a). During DJF, when aqueous oxidation of SO_2 by O_3 is important, the simulation with assumed ammonium and nitrate generally over-predicts SO_4^{2-}(*nondust*) column burdens at middle to high latitudes in both Northern and Southern Hemispheres, but tends to underestimate SO_4^{2-}(*nondust*) in the tropics and subtropics. An overestimate of SO_4^{2-}(*nondust*) of 5–10% is found over southern Canada and northeastern United States, an overestimate of 5–15% is found over the area that extends from the Northern Eurasian continent to the Arctic, and a underestimate of up to 15% is found over eastern Asia. The overestimate implies that the simulation with assumed ammonium and without nitrate predicts higher cloud pH (i.e., less acidity) and vise versa.

The results shown in Figure 5.16(a) can be explained by examining the ambient

molar ratio of NH_4^+ to SO_4^{2-}(*nondust*) (Figure 5.16(b)), which is obtained from the baseline simulation and averaged over DJF. Although the ratio shown here is not the ratio in cloud drops, the in-cloud molar ratio of sulfate to ammonium should have similar behavior as a result of mass exchange between cloud and ambient air through cloud scavenging and evaporation of rain and cloud water. At the surface layer, the predicted molar ratio of NH_4^+ to SO_4^{2-}(*nondust*) is generally lower than 1.0 from middle to high latitudes in both hemispheres. Assuming the molar ratio of NH_4^+ to SO_4^{2-}(*nondust*) to be 1.0 in those regions and ignoring nitrate leads to overestimation of cloud pH and overestimation of sulfate concentration in areas with high SO_2 emissions, as shown in Figure 5.16(a). The molar ratio of NH_4^+ to SO_4^{2-}(*nondust*) can be as high as 2 to 4 in many areas in the tropics and subtropics, but in most of these regions, H_2O_2 concentrations are relatively high compared to those in middle and high latitudes, and less SO_2 is available to form sulfate; hence, aqueous oxidation of SO_2 by O_3 is less important. In eastern Asia, since the molar ratio of NH_4^+ to SO_4^{2-}(*nondust*) is in the range of 2 to 4 and SO_2 emission is high, the simulation with assumed ammonium and in the absence of nitrate underpredicts pH and hence underestimates sulfate column burdens.

5.10 Summary and Conclusions

We have developed a unified model for the study of chemistry-aerosol-climate interactions by incorporating a coupled tropospheric chemistry-aerosol simulation in the GISS GCM II'. The model includes a detailed simulation of tropospheric ozone-NO_X-hydrocarbon chemistry and a thermodynamic representation of sulfate/nitrate/ammonium

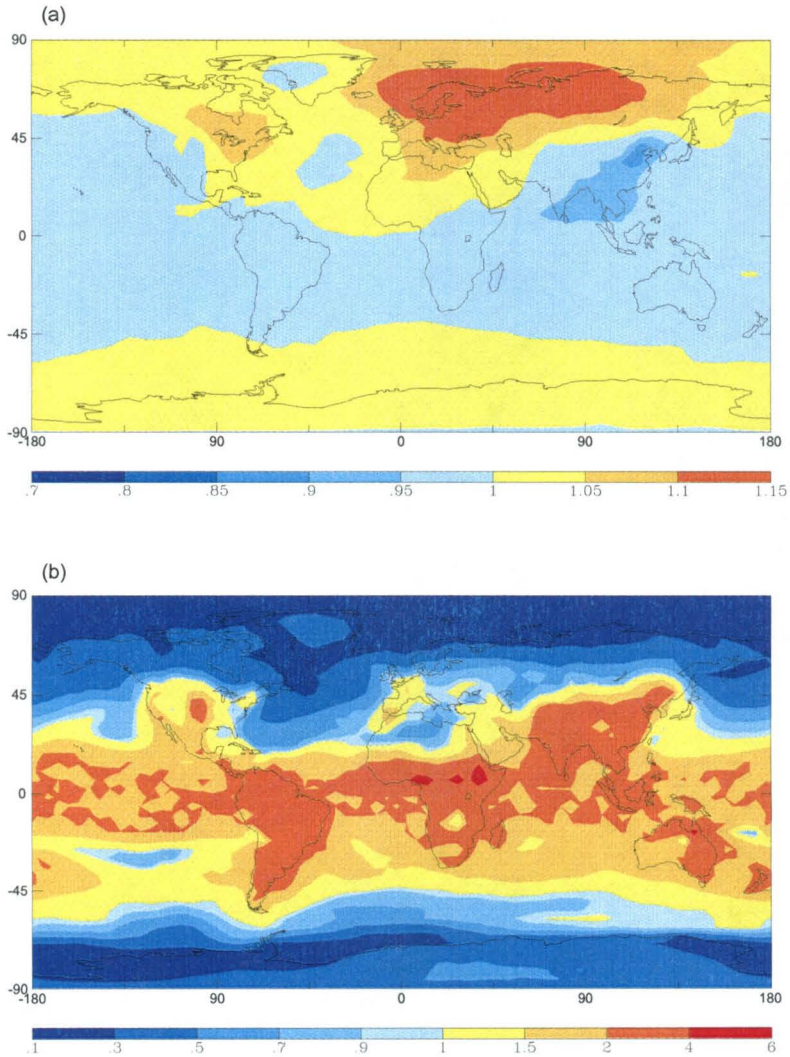

Figure 5.16 (a) Ratio of December-January-February (DJF) averaged SO_4^{2-}(*nondust*) column burdens calculated assuming the in-cloud NH_4^+/SO_4^{2-}(*nondust*) molar ratio = 1 and no NO_3^-(*nondust*) to those from the baseline run (with prognostic in-cloud NH_4^+ and NO_3^-(*nondust*)); (b) December-January-February (DJF) averaged molar ratio of NH_4^+ to SO_4^{2-}(*nondust*) in the surface layer for the baseline simulation.

aerosols. The model takes into account the effects of all aerosol classes (SO_4^{2-}(*nondust*)/NO_3^-(*nondust*)/NH_4^+/H_2O, OC, BC, and mineral dust) on photolysis rates, heterogeneous reactions of N_2O_5, NO_3, NO_2, and HO_2 on wetted aerosol surfaces, and uptake of SO_2, HNO_3 and O_3 by mineral dust. Although the current version of the unified model does not include prognostic treatments of black carbon, organic carbon, and mineral dust aerosols, we include effects of these particles on photolysis and heterogeneous processes by using three-dimensional off-line fields.

We have compared our coupled simulation with the tropospheric chemistry simulation of *Mickley et al.* [1999], the SO_4^{2-}(*nondust*) simulation of *Koch et al.* [1999], and the SO_4^{2-}(*nondust*)/NO_3^-(*nondust*)/NH_4^+ simulation of Adams99, which are the elements of the simulation that we unified. Since we include in-cloud oxidation of SO_2 by O_3 and uptake of SO_2 by mineral dust, predicted upper tropospheric SO_2 concentrations are lower than those of *Koch et al.* [1999] in the middle and high latitudes of the Northern Hemisphere. For the same reason, predicted annual and global mean SO_4^{2-}(*nondust*) concentration is 36% higher near the surface but 40% lower in the middle troposphere compared with the values obtained by Adams99. Compared with previous studies, predicted gas-phase HNO_3 concentrations show closer agreement with measurements as a result of dust uptake of HNO_3 and scavenging of HNO_3 by ice.

The unified model also simulates sulfate and nitrate aerosols that form on mineral dust particles. In the vicinity of dust source regions, more than 50% of total sulfate near the surface is predicted to be associated with mineral dust, which agrees with the results of *Dentener et al.* [1996]. On a global mean basis, based on currently available

chemical understanding, nitrate aerosol formation on dust particles is predicted to exceed that resulting from ammonium nitrate aerosol formation.

We have applied the unified model to investigate interactions between gas-phase chemistry and aerosols. The global effect of aerosols on gas-phase chemistry through altered photolysis rates is found to be small. Heterogeneous processes are shown to be important for both gas-phase species and aerosols. Although the surface area of mineral dust is predicted to be only a small fraction of total global aerosol surface area, based on current understanding mineral dust aerosol is predicted to play a significant role through uptake of O_3, SO_2, and HNO_3.

Interactions between gas-phase chemistry and aerosols are shown to be important in other aspects. For example, in-cloud sulfate formation is affected when O_3 concentration varies or when cloud droplet pH is influenced by aerosol formation. Sulfate and nitrate aerosol formation associated with mineral dust depends on the alkalinity of dust particles and availability of gas-phase HNO_3 and SO_2. Such processes interact with each other and lead to nonlinear changes in burdens of gas-phase species and aerosols when NO_X, ammonia, and sulfur emissions change. For example, an assumed across-the-board 50% increase in global NO_X emissions leads to predicted changes in burdens of HNO_3, O_3, SO_4^{2-}(*nondust*), NH_3, NH_4^+, NO_3^-(*nondust*), SO_4^{2-}(*dust*), and NO_3^-(*dust*) by +37%, +13%, +4%, -15%, +5%, +12%, -21% and +22%, respectively. An increase in NH_3 emissions mainly influences burdens of NH_3, NH_4^+, and NO_3^-(*nondust*). A 50% increase in sulfur emissions significantly impacts SO_4^{2-}(*nondust*), SO_4^{2-}(*dust*), and ammonium nitrate formation, while it has small impact on HNO_3, O_3, and NO_3^-(*dust*) burdens.

Sensitivity studies highlight the importance of using prognostic fields for aerosol simulation. Assuming the in-cloud molar ratio of NH_4^+/SO_4^{2-}(*nondust*) to be fixed at 1.0 and neglecting nitrate aerosol leads to an overestimate of winter SO_4^{2-}(*nondust*) burden by 5–15% over the North America and Eurasian continents, whereas it leads to a underestimate of the SO_4^{2-}(*nondust*) burden by 15% over eastern Asia.

The model presented here is the first step in the development of a unified climate/chemistry/aerosol model. In future work, sea salt, organic and black carbon, as well as mineral dust aerosols, will be integrated into the on-line GCM, including radiative forcing and climate response studies.

Acknowledgement. This work was supported by the National Aeronautics and Space Administration Earth Observing System Interdisciplinary Science program (NASA EOS-IDS). We also like to acknowledge the Center for Advanced Computing Research at Caltech for computing resources.

References

Adams, P. J., J. H. Seinfeld, and D. M. Koch, Global concentrations of tropospheric sulfate, nitrate, and ammonium aerosol simulated in a general circulation model, *J. Geophys. Res., 104*, 13,791–13,824, 1999.

Adams, P. J., J. H. Seinfeld, D. M. Koch, L. Mickley, and D. Jacob, General circulation model assessment of direct radiative forcing by the sulfate-nitrate-ammonium-water inorganic aerosol system, *J. Geophys. Res., 106*, 1097–1111, 2001.

Andreae, M. O., and P. J. Crutzen, Atmospheric aerosols: biogeochemical sources and role in atmospheric chemistry, *Science, 276*, 1052–1058, 1997.

Atkinson, R., D. L. Baulch, R. A. Cox, R. F. Hampson, Jr., J. A. Kerr, and J. Troe, Evaluated kinetic and photochemical data for tropospheric chemistry: Supplement IV, *Atmos. Environ., 26A*, 1187–1230, 1992.

Barth, M. C., P. J. Rasch, J. T. Kiehl, C. M. Benkovitz, and S. E. Schwartz, Sulfur chemistry in the National Center for Atmospheric Research Community Climate Model: Description, evaluation, features, and sensitivity to aqueous chemistry, *J. Geophys. Res., 105*, 1387–1415, 2000.

Benkovitz, C. M., M. T. Scholtz, J. Pacyna, L. Tarrason, J. Dignon, E. C. Voldner, P. A. Spiro, J. A. Logan, and T. E. Graedel, Global gridded inventories of anthropogenic emissions of sulfur and nitrogen, *J. Geophys. Res., 101*, 29,239–29,253, 1996.

Bouwman, A.F., D. S. Lee, W. A. H. Asman, F. J. Dentener, K. W. VanderHoek, and

J. G. J. Olivier, A global high-resolution emission inventory for ammonia, *Global Biogeochem. Cycles, 11*, 561–587, 1997.

Brasseur, G. P., D. A. Hauglustaine, S. Walters, P. J. Rasch, J.-F. Mller, C. Granier, and X. X. Tie, MOZART, a global chemical transport model for ozone and related chemical tracers, 1. Model description, *J. Geophys. Res., 103*, 28,265–28,289, 1998.

Castro, T., L. G. Ruizsuarez, J. C. Ruizsuarez, M. J. Molina, and M. Montero, Sensitivity analysis of a UV-radiation transfer model and experimental photolysis rates of NO2 in the atmosphere of Mexico City, *Atmos. Environ., 31*, 609–620, 1997.

Chatfield, R. B., Anomalous HNO_3/NO_X ratio of remote tropospheric air: Conversion of nitric acid to formic acid and NO_X, *Geophys. Res. Lett., 21*, 2705–2708, 1994.

Chin, M., D. J. Jacob, G. M. Gardner, M. S. Foreman-Fowler, P. A. Spiro, and D. L. Savoie, A global three-dimensional model of tropospheric sulfate, *J. Geophys. Res., 101*, 18,667–18,690, 1996.

Chin, M., R. B. Rood, S. J. Lin, J. F. Muller, and A. M. Thompson, Atmospheric sulfur cycle simulated in the global model GOCART: Model description and global properties, *J. Geophys. Res., 105*, 24,671–24,687, 2000.

Chuang, C. C., J. E. Penner, K. E. Taylor, A. S. Grossman, and J. J. Walton, An assessment of the radiative effects of anthropogenic sulfate, *J. Geophys. Res., 102*, 3761–3778, 1997.

Cooke, W. F., and J. J. N. Wilson, A global black carbon aerosol model, *J. Geophys. Res., 101*, 19,395–19,409, 1996.

Cooke, W. F., C. Liousse, H. Cachier, and J. Feichter, Construction of a $1° \times 1°$ fossil fuel emission data set for carbonaceous aerosol and implementation and radiative impact in the ECHAM4 model, *J. Geophys. Res., 104*, 22,137–22,162, 1999.

Crutzen, P. J., and P. H. Zimmermann, The changing photochemistry of the troposphere, *Tellus, 43AB*, 136–151, 1991.

d'Almeida, G. A., P. Koepke, and E. P. Shettle, *Atmospheric Aerosols: Global Climatology and Radiative Characteristics*, A. Deepak Publishing, Hampton, VA, 1991.

Del Genio, A. D., and M.-S. Yao, Efficient cumulus parameterization for long-term climate studies: The GISS scheme, in *The Representation of Cumulus Convection in Numerical Models, Monogr. 46*, edited by K. A. Emanuel and D. J. Raymond, pp. 181–184, AM. Meteorol. Soc., Boston, Mass., 1993.

Del Genio, A. D., M.-S. Yao, W. Kovari, and K. K.-W. Lo, A prognostic cloud water parameterization for global climate models, *J. Clim., 9*, 270–304, 1996.

Demerjian, K. L., K. L. Schere, and J. T. Peterson, Theoretical estimates of actinic (spherially integrated) flux and photolytic rate constants of atmospheric species in the lower troposphere, *Adv. Environ. Sci. Tech., 10*, 369–459, 1980.

DeMore, W. B., C. J. Howard, S. P. Sander, A. R. Ravishankara, D. M. Golden, C. E. Kolb, R. F. Hampson, M. J. Molina, and M. J. Kurylo, *Chemical Kinetics and Photochemical Data for Use in Stratospheric Modeling*, Jet Propulsion Laboratory, Pasadena, California, 1997.

Dentener, F. J., G. R. Carmichael, Y. Zhang, J. Lelieveld, and P. J. Crutzen, Role of mineral

aerosol as a reactive surface in the global troposphere, *J. Geophys. Res., 101*, 22,869–22,889, 1996.

Dentener, F. J., and P. J. Crutzen, Reaction of N_2O_5 on tropospheric aerosols: impact on the global distributions of NO_X, O_3, and OH, *J. Geophys. Res., 98*, 7149–7163, 1993.

Dentener, F. J., and P. J. Crutzen, A three-dimensional model of global ammonia cycle, *J. Atmos. Chem., 19*, 331–369, 1994.

Dickerson, R. R., S. Kondragunta, G. Stenchikov, K. L. Civerolo, B. G. Doddridge, and B. N. Holben, The impact of aerosols on solar ultraviolet-radiation and photochemical smog, *Science, 215*, 827–830, 1997.

Erickson, D. J., J. J. Walton, S. J. Ghan, and J. E. Penner, Three-dimensional modeling of the global atmospheric sulfur cycle: A first step, *Atmos. Environ., Part A, 25*, 2513–2520, 1991.

Fan, S.-M., D. J. Jacob, D. L. Mauzerall, J. D. Bradshow, S. T. Sandholm, D. R. Blake, H. B. Singh, R. W. Talbot, G. L. Gregory, and G. W. Sachse, photochemistry of reactive nitrogen in the subArctic troposphere in summer 1990: Observation and modeling, *J. Geophys. Res., 99*, 16,867–16,878, 1994.

Feichter, J., E. Kjellstrom, H. Rodhe, F. Dentener, J. Lelieveld, and G.-J. Roelofs, Simulation of the tropospheric sulfur cycle in a global climate model, *Atmos. Environ., 30*, 1693–1707, 1996.

Galy-Lacaux, C., and A. I. Modi, Precipitation chemistry in the Sahelian savanna of Niger, Africa, *J. Atmos. Chem., 30*, 319–343, 1998.

Galy-Lacaux, C., G. R. Carmichael, C. H. Song, J. P. Lacaux, H. Al Ourabi, and A. I. Modi, Heterogeneous processes involving nitrogenous compounds and Saharan dust inferred from measurements and model calculations, *J. Geophys. Res., 106*, 12,559–12,578, 2001.

Ghan, S., N. Laulainen, R. Easter, R. Wagener, S. Nemesure, E. Chapman, Y. Zhang, and R. Leung, Evaluation of aerosol direct radiative forcing in MIRAGE, *J. Geophys. Res., 106*, 5295–5316, 2001.

Guenther, A., C. N. Hewitt, D. Erickson, R. Fall, C. Geron, T. Graedel, P. Harley, L. Klinger, M. Lerdau, W. A. Mckay, T. Pierce, B. Scholes, R. Steinbrecher, R. Tallamraju, J. Taylor, and P. Zimmerman, A global model of natural volatile organic compound emissions, *J. Geophys. Res., 100*, 8873–8892, 1995.

Hansen, J., G. Russell, D. Rind, P. Stone, A. Lacis, S. Lebedeff, R. Ruedy, and L. Travis, Efficient three-dimensional global models for climate studies: Models I and II, *Mon. Weather Rev., 111*, 609–662, 1983.

Hansen, J. E., and L. D. Travis, Light scattering in planetary atmospheres, *Space Sci. Rev., 16*, 527–610, 1974.

Hansen, J., M. Sato, and R. Ruedy, Radiative forcing and climate response, *J. Geophys. Res., 102*, 6831–6864, 1997.

Hauglustaine, D. A., G. P. Brasseur, S. Walters, P. J. Rasch, J. F. Muller, L. K. Emmons, and C. A. Carroll, MOZART, a global chemical transport model for ozone and related chemical tracers 2. Model results and evaluation, *J. Geophys. Res., 103*, 28,291–

28,335, 1998.

Haywood, J. M., and V. Ramaswamy, Global sensitivity studies of the direct radiative forcing due to anthropogenic sulfate and black carbon aerosols, *J. Geophys. Res., 103*, 6043–6058, 1998.

Intergovernmental Panel on Climate Change (IPCC), *Climate Change 2001*, edited by J. T. Houghton et al., Cambridge Univ. Press, New York, 2001.

Jacob, D. J., Chemistry of OH in remote clouds and its role in the production of formic acid and peroxymonosulfate, *J. Geophys. Res., 91*, 9807–9826, 1986.

Jacob, D. J., Heterogeneous chemistry and tropospheric ozone, *Atmos. Environ., 34*, 2131–2159, 2000.

Jacobson, M. Z., and R. P. Turco, SMVGEAR - A sparse-matrix, vectorized GEAR code for atmospheric models, *Atmos. Environ., 28*, 273–284, 1994.

Jacobson, M. Z., Studying the effects of aerosols on vertical photolysis rate coefficient and temperature profiles over an urban airshed, *J. Geophys. Res., 103*, 10593–10604, 1998.

Johnson, C. E., Relative roles of climate and emissions changes on future tropospheric oxidant concentrations, *J. Geophys. Res., 104*, 18,631–18,645, 1999.

Kanakidou, M., K. Tsigaridis, F. J. Dentener, and P. J. Crutzen, Human-activity-enhanced formation of organic aerosols by biogenic hydrocarbon oxidation, *J. Geophys. Res., 105*, 9243–9254, 2000.

Kasibhatla, P., W. L. Chameides, and J. St. John, A three-dimensional global model investigation of seasonal variations in the atmospheric burden of anthropogenic sulfate aerosols, *J. Geophys. Res., 102*, 3737–3759, 1997.

Kim, D. S., and V. P. Aneja, Chemical composition of clouds at Mt. Mitchell, North Carolina, USA, *Tellus, 44B*, 41–53, 1992.

Kjellstrom, E., A three-dimensional global model study of carbonyl sulfide in the troposphere and the lower stratosphere, *J. Atmos. Chem., 29*, 151–177, 1998.

Koch, D. M., D. Jacob, I. Tegen, D. Rind, and M. Chin, Tropospheric sulfur simulation and sulfate direct radiative forcing in the Goddard Institute for Space Studies general circulation model, *J. Geophys. Res., 104*, 23,799–23,822, 1999.

Landgraf, J., and P. J. Crutzen, An efficient method for online calculations of photolysis and heating rates, *J. Atmos. Sci., 55*, 863–878, 1998.

Langner, J., and H. Rodhe, A global three-dimensional model of the tropospheric sulfur cycle, *J. Atmos. Chem., 13*, 225–263, 1991.

Lantz, K. O., R. E. Shetter, C. A. Cantrell, S. J. Flocke, J. G. Calvert, and S. Madronich, Theoretical, actinometric, and radiometric determinations of the photolysis rate coefficient of NO_2 during the Mauna Loa observatory photochemistry experiment 2, *J. Geophys. Res., 101*, 14613–14629, 1996.

Lawrence, M. G., and P. J. Crutzen, The impact of cloud particle gravitational settling on soluble trace gas distributions, *Tellus, Ser.B, 50*, 263–289, 1998.

Lelieveld, J., G.-J. Roelofs, J. Feichter, and H. Rodhe, Terrestrial sources and distribution of atmospheric sulphur, *Philos. Trans. R. Soc. London, 352*, 149–157, 1997.

Levy, H., II, J. D. Mahlman, W. J. Moxim, and S. C. Liu, Tropospheric ozone: The role of transport, *J. Geophys. Res., 90*, 3753–3772, 1985.

Liao, H., Y. L. and J. H. Seinfeld, Effects of aerosols on tropospheric photolysis rates in clear and cloudy atmospheres, *J. Geophys. Res., 104*, 23,697–23,707, 1999.

Liou, K. N., *Radiation and Cloud Processes in the Atmosphere: Theory, Observation, and Modeling*, Oxford University Press, New York, 1992,

Liousse C., J. E. Penner, C. Chuang, J. J. Walton, H. Eddleman, and H. Cachier, A global three-dimensional model study of carbonaceous aerosols, *J. Geophys. Res., 101*, 19,411–19,432, 1996.

Maahs, H. G., Sulfur dioxide/water euilibrium between 0° and 50°C: An examination of data at low concentrations, in *Heterogeneous Atmospheric Chemistry, Geophys. Monogr. Ser.*, edited by D. R. Schryer, vol. 26, 273, AGU, Washington, D. C., 1982.

Mishchenko, M. I., W. B. Rossow, A. Macke, and A. A. Lacis, Sensitivity of cirrus cloud albedo, bidirectional reflectance and optical thickness retrieval accuracy to ice particle shape, *J. Geophys. Res., 101*, 16,973–16,985, 1996.

McPeters, R., Ozone profile comparisons, in *The atmospheric effects of stratospheric aircraft: Report of the 1992 models and measurement workshop*, edited by E.E. Remsberg and M.J. Prather, pp. D1-D37, NASA Ref. Publ. 1292, 1993.

Mickley, L. J., P. Murti, D. Jacob, J. Logan, and D. Rind, Radiative forcing from tropospheric ozone calculated with a unified chemistry-climate model, *J. Geophys. Res. 104*, 30,153–30,172, 1999.

Müller, J.-F., and G. Brasseur, IMAGES: A three-dimensional chemical transport model of the global troposphere, *J. Geophys. Res., 100*, 16,445–16,490, 1995.

National Bureau of Standards, Selected values of chemical thermodynamic properties, 1, *Tech. Note 270-1*, Gaithersburg, Md., 1965.

National Research Council, *Global Air Quality: An Imperative for Long-Term Observation Strategies*, National Academy Press, Washington, D. C., 2001.

Nenes, A., C. Pilinis, and S. N. Pandis, Isorropia: A new thermodynamic equilibrium model for multiphase multicomponent inorganic aerosols, *Aquat. Geochem., 4*, 12–152, 1998.

Oberholzer, B., J. L. Collett, J. Staehelin, and A. Waldvogel, In-cloud scavenging of gases and aerosols at mountain site in central Switzerland, *J. Atmos. Chem., 14*, 61–71, 1992.

Penner, J. E., H. Eddleman, and T. Novakov, Towards the development of a global inventory of black carbon emissions, *Atmos. Environ., 27A*, 1277–1295, 1993.

Penner, J. E., C. S. Atherton, and T. E. Graedel, Global emissions and models of photochemically active compounds, in *Global Atmospheric-Biosheric Chemistry*, edited by R. G. Prinn, pp. 223–247, Plenum, New York, 1994.

Pham, M., J.-F. Mller, G. P. Brasseur, C. Granier, and G. Megie, A three-dimensional study of the tropospheric sulfur cycle, *J. Geophys. Res., 100*, 26,061–26,092, 1995.

Rasch, P. J., M. C. Barth, J. T. Kiehl, S. E. Schwartz, and C. M. Benkovitz, A description of the global sulfur cycle and its controlling processes in the National Center for Atmospheric Research Community Climate Model, Version 3, *J. Geophys. Res., 105*, 1367–1385, 2000.

Restad, K., I. S. A. Isaksen, and T. K. Berntsen, Global distribution of sulfate in the troposphere: A three-dimensional model study, *Atmos. Environ., 30*, 3593–3609, 1998.

Rind, D., and J. Lerner, The use of on-line tracers as a diagnostic tool in general circulation model development, 1, Horizontal and vertical transport in the troposphere, *J. Geophys. Res., 101*, 12,667–12,683, 1996.

Rind, D., J. Lerner, K. Shah, and R. Suozzo, Use of on-line tracers as a diagnostic tool in general circulation model development, 2. Transport between the troposphere and stratosphere, *J. Geophys. Res., 104*, 9151–9167, 1999.

Roelofs, G.-J., and J. Lelieveld, Distribution and budget of O_3 in the troposphere calculated with a chemistry general circulation model, *J. Geophys. Res., 100*, 20,983–20,998, 1995.

Roelofs, G.-J., J. Lelieveld, and R. van Dorland, A three-dimensional chemistry/general circulation model simulation of anthropogenically derived ozone in the troposphere and its radiative forcing, *J. Geophys. Res., 102*, 23,389–23,401, 1997.

Roelofs, G.-J., J. Lelieveld, and L. Ganzeveld, Simulation of global sulfate distribution and the influence on effective cloud drop radii with a coupled photochemistry sulfur cycle model, *Tellus, Ser. B, 50*, 224–242, 1998.

Roelofs, G.-J., and J. Lelieveld, Tropospheric ozone simulation with a chemistry-general circulation model: Influence of higher hydrocarbon chemistry, *J. Geophys. Res., 105*, 22,697–22,712, 2000.

Ruggaber, A., R. Dlugir, and T. Nakajima, Modeling radiation quantities and photolysis frequencies in the atmosphere, *J. Atmos. Chem., 18*, 171–210, 1994.

Schwartz, S.E., Mass-transport considerations pertinent to aqueous-phase reactions of gases in liquid-water clouds, in *Chemistry of Multiphase Atmospheric Systems*, ed. by W. Jaechske, 415–471, Springer, Heidelberg, 1986.

Seinfeld, J. H., and S. N. Pandis, *Atmospheric Chemistry and Physics*, John Wiley, New York, 1998.

Singh, H. B., D. Ohara, D. Herlth, W. Sachse, D. R. Blake, J. D. Bradshaw, M. Kanakidou, and P. J. Crutzen, Acetone in the atmosphere: Distribution, sources, and sinks, *J. Geophys. Res., 99*, 1805–1819, 1994.

Sinha, A., and R. Toumi, Tropospheric ozone, lightning, and climate change, *J. Geophys. Res., 102*, 10,667–10,672, 1997.

Song, C. H., and G. R. Carmichael, The aging process of naturally emitted aerosol (sea-salt and mineral aerosol) during long-range transport, *J. Geophys. Res.*, in press, 2001.

Tang, I. N., Thermodynamic and optical properties of mixed-salt aerosols of atmospheric importance, *J. Geophys. Res., 102*, 1883–1893, 1997.

Tbazaedeh, A., M. Z. Jacobson, H. B. Singh, O. B. Toon, J. S. Linn, R. B. Chatfield, A. N. Thakur, R. W. Talbot, and J. E. Dibb, Nitric acid scavenging by mineral and biomass burning aerosols, *Geophys. Res. Lett., 25*, 4185–4188, 1998.

Tegen, I., and I. Fung, Modeling of mineral dust in the atmosphere; sources, transport, and optical thickness, *J. Geophys. Res., 99*, 22,897–22,914, 1994.

Tegen, I., and I. Fung, Contribution to the atmospheric mineral aerosol load from land surface modification. *J. Geophys. Res. 100*, 18,707–18,726, 1995.

Toumi, R., J. D. Haigh, and K. S. Law, A tropospheric ozone-lightning climate feedback, *Geophys. Res. Lett., 23*, 1037–1040, 1996.

Wang, Y., D. J. Jacob, and J. A. Logan, Global simulation of tropospheric O_3-NO_X-hydrocarbon chemistry, 1. Model formulation, *J. Geophys. Res., 103*, 10,713–10,725, 1998.

Wesely, M. L., Parameterization of surface resistances to gaseous dry deposition in regional-scale numerical models, *Atmos. Environ., 23*, 1293–1304, 1989.

Wild, O., X. Zhu, and M. J. Prather, Fast-J: Accurate simulation of in- and below-cloud photolysis in tropospheric chemical models, *J. Atmos. Chem., 37*, 245–282, 2000.

Yienger, J. J., and H. Levy, Empirical-model of global soil-biogenic NO_X emissions, *J. Geophys. Res., 100*, 11,447–11,464, 1995.

Zhang, Y., and G. R. Carmichael, The role of mineral aerosol in tropospheric chemistry in East Asia - A model study, *J. Appl. Meteorol., 38*, 353–366, 1999.

Chapter 6

Summary and Conclusions

This thesis is a composite of works that examine effects of aerosols on atmospheric chemistry and climate. Chapter 2 examines effect of clouds on aerosol direct radiative forcing. The presence of an embedded cloud layer enhances the heating effect of absorbing aerosols located above the cloud layer, but shields the radiative effects of aerosols below cloud. Chapter 3 studies the sensitivity of diurnal average mineral dust forcing to dust physical and optical properties. The sign of top-of-atmosphere radiative forcing depends on surface albedo, particle size, imaginary part of refractive index, and the presence or absence of clouds. At the surface, shortwave forcing always leads to cooling and longwave radiative forcing always leads to heating. Chapter 4 investigates effects of aerosols on photolysis rates in clear and cloudy atmospheres. Nonabsorbing aerosol generally enhances photolysis rates above and in the upper part of the aerosol layer in both noncloudy and cloudy atmospheres, with the enhancement effect reduced in the presence of clouds. In contrast, absorbing aerosol reduces photolysis rates under both noncloudy and cloudy sky conditions, with the reduction accentuated by a cloud layer.

Chapter 5 presents a unified model that simulates both tropospheric chemistry and sulfate/nitrate/ammonium aerosols within the Goddard Institute for Space Studies general circulation model. We have applied the unified model to investigate interactions between gas-phase chemistry and aerosols. The global effect of aerosols on gas-phase chemistry through altered photolysis rates is found to be small. Heterogeneous processes are shown to be important for both gas-phase species and aerosols. Based on current understanding, mineral dust aerosol is predicted to play a significant role in both gas-phase chemistry and aerosol formation through uptake of O_3, SO_2, and HNO_3.

The unified model represents the first step in the development of a fully coupled climate/chemistry/aerosol model. Several aspects of the unified model can be improved in future research. Current version of the model uses off-line three-dimensional fields of organic carbon, black carbon, and mineral dust aerosols for the simulation of heterogeneous and photolysis processes. In future work, these aerosols, as well as sea salt aerosol, will be integrated into the on-line GCM. Both primary organic carbon aerosol, which is emitted directly into the atmosphere as products of fossil fuel combustion or biomass burning, and secondary organic aerosol, which is formed by the condensation of semi-volatile organic compounds on pre-existing aerosols, will be taken into account. Black carbon (elementary carbon) will also be treated as a tracer in the unified model. Sea salt aerosol uptakes SO_2 and HNO_3 [*Tabazadeh et al.*, 1998] and serves as CCN in the marine boundary layer [*Ghan et al.*, 1998], which is expected to play significant roles in gas-phase chemistry and global climate. Radiative forcing by ozone and climate response will also be simulated in subsequent work.

The unified model with above features will be used to improve understanding of aerosol-chemistry-climate interactions in the context of expected changes in emissions and climate during the next century. We will focus on the following questions:

1. How will changes in emissions and climate affect the abundances of tropospheric O_3 and aerosols over the next century?
2. What will be the radiative and climate consequences of these changes?
3. How will aerosol-chemistry-climate feedbacks affect the ultimate climate response from changes in tropospheric O_3 and aerosols?

4. How will future climate change affect O_3 and aerosol air pollution in populated regions of the world?

References

Ghan, S. J., G. Guzman, and H. Abdul-Razzak, Competition between sea salt and sulfate particles as cloud condensation nuclei, *J. Atmos. Sci., 55*, 3340–3347, 1998.

Tbazaedeh, A., M. Z. Jacobson, H. B. Singh, O. B. Toon, J. S. Linn, R. B. Chatfield, A. N. Thakur, R. W. Talbot, and J. E. Dibb, Nitric acid scavenging by mineral and biomass burning aerosols, *Geophys. Res. Lett., 25*, 4185–4188, 1998.